THE UNIVERSITY *of* EDINBURGH

Constraining the Yukawa coupling using Run 3 data from the ATLAS Experiment at the LHC

Julia Frances Allen

THE UNIVERSITY
of EDINBURGH

Doctor of Philosophy
The University of Edinburgh
March 2025

To my family
Josephine, Bridget, Cecelia and Harry

Abstract

Since the discovery of the Higgs boson at the Large Hadron Collider (LHC) in 2012, particle physicists have endeavoured to measure its properties to better understand its nature. The thesis focuses on the Higgs boson's coupling to Standard Model fermions, referred to as the Yukawa coupling.

Using Run 3 data from the ATLAS Experiment at the LHC, this work presents an innovative approach to indirectly probe the Yukawa coupling to the light (up and down) quarks and the charm quark. Direct searches for Higgs boson decays into quark pairs are systematically limited by the efficiency of determining quark flavour from the hadronic jets in the final state. Alternatively, kinematic distributions of the Higgs boson, such as the transverse momentum spectrum, offer an indirect probe of the Yukawa coupling. The transverse momentum is sensitive to quark-initiated Higgs production which has a softer distribution compared to the dominant gluon fusion production due to the lower colour charge of quarks. This technique is applied to events where the Higgs boson has decayed to two photons. The diphoton decay channel has a branching ratio of 0.23%.

During Run 2 of the ATLAS Experiment, this method was first employed to constrain the charm and bottom quark Yukawa coupling modifiers. Implementing a multivariate analysis designed to classify Higgs boson production modes using Higgs kinematics, this thesis aims to improve the technique and ultimately the sensitivity to the Yukawa couplings. This study uses $58.6\,\text{fb}^{-1}$ of proton-proton collision data collected in 2022–2023 at a centre-of-mass energy of $\sqrt{s} = 13.6\,\text{TeV}$. The expected constraints on the light and charm quark Yukawa couplings are found to be below that of the bottom quark at the 95% confidence level. Since the Standard Model predicts a hierarchical structure in Yukawa couplings, with the first- and second-generation couplings smaller than those of the third-generation, this work demonstrates that Higgs kinematics can be used to experimentally establish this hierarchy.

Lay summary

> *"The Higgs boson is the manifestation of the Higgs field, and it is the field that gives mass to the elementary particles. Without it, particles would remain massless and there would be no atoms, no chemistry, no life."*
>
> Peter Higgs

The Standard Model of Particle Physics (SM) is the theory explaining how the fundamental particles of the Universe interact. An established and well-tested theory, the SM has successfully explained almost all current experimental data and has predicted a wide range of phenomena. In the SM, fundamental particles obtain their mass through their interaction with the Higgs boson. Before 2012, the Higgs boson was the last missing piece of the SM puzzle and, searching for it, the motivation for the construction of the Large Hadron Collider (LHC).

Located at CERN in Geneva, the LHC is the world's largest particle accelerator. Constructed with the primary aim of discovering the Higgs boson, protons are accelerated to nearly the speed of light before colliding them head-on. Proton collisions at the LHC provide the necessary conditions to enable physicists to study rare subatomic particles. By detecting these particles, physicists gain an insight into the subatomic world. This insight is essential for understanding the nature of the Universe. Four main detectors are located around the LHC ring. This thesis analyses proton-proton collision data from one such detector, known as the ATLAS Experiment.

The discovery of the Higgs boson in 2012 by ATLAS and CMS collaborations at the LHC was a significant milestone in particle physics — the SM was now complete. In 2013, the Nobel Prize in Physics was awarded to François Englert and Peter Higgs *'for the theoretical discovery of a mechanism that contributes to our understanding of the origin of mass of subatomic particles'*. Now 10 years

on from this discovery, the ATLAS Experiment has observed 30 times as many Higgs bosons and continues to study its properties.

This thesis studies the interaction between the Higgs boson and quarks, the building blocks of protons. Quarks are divided into three generations; first-generation quarks are the lightest and the third-generation are the heaviest. The SM predicts that the Higgs boson's coupling strength (referred to as the Yukawa coupling) is proportional to the mass of the particle it interacts with. A hierarchy in the strength of the Higgs boson coupling to quarks is therefore expected, with the coupling to third-generation quarks being the strongest.

This thesis presents a novel approach to studying the Higgs boson coupling to first- and second-generation quarks. The technique developed in this thesis is expected to confirm the hierarchy of the Higgs boson couplings since the first- and second-generation couplings are expected to be weaker than the third-generation. By confirming the SM prediction, these results would contribute to a deeper understanding of the SM and the Higgs boson.

Declaration

I declare that this thesis was composed by myself, that the work contained herein is my own except where explicitly stated otherwise in the text, and that this work has not been submitted for any other degree or professional qualification except as specified.

(*Julia Frances Allen, March 2025*)

Acknowledgements

First and foremost, I would like to express my deepest gratitude to Liza Mijović for her invaluable role in the development of this thesis. Her guidance and expertise have been instrumental in shaping this work and I could not have completed this without her.

I am sincerely grateful to Victoria Martin for her insightful advice and continuous encouragement throughout my PhD. I am especially thankful for the opportunity to pursue my PhD under her guidance.

I would like to thank my Higgs colleagues at the University of Edinburgh and CERN. In particular, I extend my gratitude to Davide Mungo for his involvement in the JVT studies, Ana Rosario Cueto Gomez for her modelling expertise and Luis Pascual Dominguez for his expertise in photon isolation.

Thanks are due to the ATLAS trigger group, particularly the trigger operations team, for their expertise and collaboration. Special thanks go to Julie Kirk for her invaluable mentorship during my ATLAS qualification task. I am also incredibly grateful to Neofytos Themistokleous for his guidance and support with the Trigger Rate Presenter.

To Grandad Harry and Grandma Nora — your memory continues to inspire me and I hope this achievement makes you proud.

To my honorary grandparents, Enid and Peter — thank you for fostering my curiosity from a young age and for always encouraging me to ask questions.

To my siblings, Bridget, Cecelia and Harry — thank you for filling my life with joy and laughter. You make life brighter every step of the way.

To my partner, Richards — in physics and in life. Sharing this experience with you has been an incredible privilege. I am endlessly grateful for your love and support and I cannot wait to see what the future holds for us.

Finally, and most of all, to my mum, Josephine — you have always been my greatest source of strength and motivation. Your unwavering belief in me has made this PhD possible and I cannot thank you enough for everything you do. This success is as much yours as it is mine.

Contents

Abstract i

Lay summary ii

Declaration iv

Acknowledgements v

Contents vi

List of figures xiii

List of tables xvii

Acronyms xix

Glossary xxi

1 Introduction 1

2 The Standard Model of Particle Physics 5

2.1 Elementary particles and forces of nature 6

2.2 Lagrangians in Quantum Field Theory 7

2.3 The Standard Model Lagrangian 8

2.4 Quantum Electrodynamics 9

2.5 Quantum Chromodynamics 10
2.6 Electroweak Theory 11
2.7 Particle masses 13
2.8 The Brout-Englert-Higgs mechanism 14
2.9 Fermion masses and the Yukawa coupling 16

3 The Higgs boson at the Large Hadron Collider 18

3.1 From theory to experiment 19
3.1.1 Parton distribution functions 19
3.1.2 Feynman rules 21
3.2 Production modes 22
3.2.1 Gluon-gluon fusion Higgs production 24
3.2.2 Quark-initiated Higgs production 24
3.3 Decay channels 26
3.4 Higgs boson discovery 27
3.5 Parameterisation within the Kappa Framework 28
3.6 Measurements of the Yukawa coupling 31
3.6.1 Direct constraint on the charm Yukawa coupling 32
3.6.2 Constraints on the light quark Yukawa couplings 33
3.7 Fiducial cross-section analysis 35
3.7.1 Fiducal volume and cross-sections 35
3.7.2 Diphoton channel 35
3.7.3 Indirect measurements of the Yukawa couplings 36
3.7.4 Indirect constraint on the charm Yukawa coupling 38

4 The Large Hadron Collider and the ATLAS Experiment 41

4.1 The Large Hadron Collider 42

4.1.1 Events, luminosity and pile-up 44

4.2 The ATLAS detector 46

4.3 Coordinate system 48

4.4 Magnet system 49

4.5 Tracking: the Inner Detector 49

4.6 Calorimetry 52

4.6.1 Electromagnetic and hadronic showers 53

4.6.2 Energy resolution 54

4.6.3 Liquid Argon Calorimeter 54

4.6.4 Tile Calorimeter 56

4.7 Spectrometry: the Muon Spectrometer 57

4.8 Detector and accelerator upgrades 58

5 The ATLAS trigger system 59

5.1 Trigger and data acquisition 60

5.2 Level-1 trigger 61

5.3 High-level trigger 62

5.4 Trigger operations 64

6 Trigger development for Run 3 65

6.1 Optimisation of the ID tracking strategy in the HLT 66

6.2 Trigger Rate Presenter 69

7 Reconstruction and physics objects 72

7.1 Physics objects for $H \to \gamma\gamma$ analyses 73

7.2 Track reconstruction 73

7.3 Primary vertex 75

7.4 Topological clusters 76

7.5 Electron and photon reconstruction 77

7.5.1 Supercluster reconstruction 78

7.5.2 Photon identification 78

7.5.3 Diphoton vertex 80

7.6 Muon reconstruction 81

7.7 Jet reconstruction 83

7.7.1 Jet Vertex Tagger 84

7.7.2 Jet flavour tagging 84

7.8 Missing transverse energy 86

8 $H \to \gamma\gamma$ cross-section measurements 87

8.1 Run 2 and Run 3 datasets 88

8.2 Event selection 88

8.2.1 Selection of jets, leptons and $E_{\mathrm{T}}^{\mathrm{miss}}$ objects 88

8.2.2 Higgs boson production modes 89

8.2.3 Fiducial phase space 90

8.3 Modelling of the invariant mass spectrum 91

8.3.1 Signal model 91

8.3.2 Background model and spurious signal 92

8.4 Fit procedure 93
8.5 Systematic uncertainties 94
8.6 Fiducial cross-section results 96
8.7 Yukawa interpretation 96

9 Data validation 100

9.1 Datasets 101
9.1.1 Experimental data 101
9.1.2 Simulated data 102
9.2 Validation of ggF simulated samples 103
9.2.1 Photons 104
9.2.2 Jets 106
9.2.3 Missing transverse energy 109
9.3 Validation of data control regions 111
9.4 Summary 111

10 Signal modelling 112

10.1 Simulated data 113
10.2 Diphoton fiducial region 113
10.3 Fiducial subregions 117
10.4 Summary 118

11 Constraining up, down and charm quark Yukawa couplings 119

11.1 Datasets 120
11.1.1 Data and pseudo-data 120
11.1.2 Simulated data 120

11.1.3 Event selection 121
11.1.4 Parametric detector response for photons 122
11.2 Signal neural network classifier 123
11.2.1 Feature selection 123
11.2.2 Neural network architecture 127
11.2.3 Model performance 128
11.2.4 Defining orthogonal signal regions 129
11.3 Statistical analysis 131
11.3.1 Diphoton invariant mass distribution 131
11.3.2 Counting experiment 132
11.4 Results 133
11.4.1 Inclusive signal region measurement 134
11.4.2 Combined measurements 135
11.4.3 Individual measurements 138
11.4.4 Summary of assumptions 138
11.5 Outlook to full Run 3 and HL-LHC 140
11.6 Comparison to other techniques 141
11.7 Summary 141

12 Conclusion 143

A Rejecting other Higgs production modes 146

B Background rejection neural network 148

C Individual signal region plots 154

D ECFA ECR Panel 158

Bibliography 159

List of Figures

1.1 ATLAS Run 2 measurements of coupling strength modifiers. 3

2.1 The fundamental paticles of the Standard Model 6

2.2 Shape of the Higgs potential 15

3.1 Parton distribution function as a function of momentum fraction 20

3.2 Feynman diagram at leading and next-to-leading order 21

3.3 Main Higgs boson production modes at the LHC 22

3.4 Higgs production cross-sections as a function of $\sqrt{S}$. 23

3.5 Feynman diagram for quark-initiated Higgs production 24

3.6 Possible Feynman diagrams for $H \to \gamma\gamma$ 26

3.7 Diphoton invariant mass distribution from Higgs discovery 27

3.8 ATLAS Run 2 measurements of coupling strength modifiers. 31

3.9 Direct and indirect Feynman diagrams for $H \to M\gamma$ 34

3.10 ATLAS event display of $H \to \gamma\gamma$ 36

3.11 Effect of soft gluon emissions on the $p_{\mathrm{T},H}$ 37

3.12 Template $p_{\mathrm{T},H}$ spectrum of inclusive Higgs production 37

3.13 Run 2 $H \to \gamma\gamma$ constraints on the bottom and charm couplings 39

4.1 The CERN accelerator complex 42

4.2 The stages of the proton beam cycle at the LHC 43

4.3 Delivered and recorded integrated luminosity at ATLAS 45

4.4 Pile-up distribution for Run 3 data taking 46
4.5 Schematic of the ATLAS detector system 47
4.6 ATLAS coordinate system 48
4.7 Cross-section of the ATLAS Inner Detector 50
4.8 Visualisation of tracking through the Inner Detector layers 50
4.9 Representation of electromagnetic and hadronic showers 53
4.10 Cross-section of the ATLAS Liquid Argon calorimeters 55
4.11 Accordion structure of the Electromagnetic Calorimeter 55
4.12 Cross-section of the ATLAS muon system 57

5.1 ATLAS Trigger and Data Acquisition system for Run 3 60
5.2 Structure of the upgraded L1Calo trigger tower 61
5.3 Diphoton trigger efficiencies for 2022 data taking 63

6.1 Timing and efficiency plots for B-physics ID tracking 67
6.2 Schematic of Inner Detector Super RoI tracking tool 68
6.3 Snapshot of the TRP dashboard 70
6.4 Photon trigger rates displayed on the TRP dashboard 70

7.1 Track reconstruction in the ATLAS Inner Detector 74
7.2 Supercluster reconstruction for electrons and photons 78
7.3 Jet Vertex Tagger discriminating variables 85
7.4 Performance of the DL1r b-tagging algorithm 85

8.1 Composition of Higgs production in each fiducial region 90
8.2 Double sided Crystal Ball functional form 92
8.3 Diphoton invariant mass distribution for early Run 3 data 93
8.4 Template $p_{\mathrm{T},\gamma\gamma}$ distributions for different values of κ_b and κ_c 98
8.5 Two-dimensional limits on κ_b and κ_c 98

9.1 Validation of photon kinematics for simulated ggF events 105
9.2 Validation of jet multiplicity for simulated ggF events 106
9.3 Validation of JVT implementation for different jet collections 107
9.4 Validation of MET distribution for simulated ggF events 109
9.5 Data control regions for 2022 and 2023 datasets 110
9.6 Photon kinematics in 2022 and 2023 data control regions 110

10.1 Fit to the $H \to \gamma\gamma$ signal in the diphoton fiducial region. 114
10.2 Fit to the $H \to \gamma\gamma$ signal from the early Run 3 measurement 114
10.3 Fit to the $H \to \gamma\gamma$ signal in high $E_{\mathrm{T}}^{\mathrm{miss}}$ and $t\bar{t}H$ subregions 116

11.1 NLO in QCD Feynman diagrams for $u\bar{u} \to H$ production 121
11.2 NNLO in QCD Feynman diagrams for $u\bar{u} \to H$ production 121
11.3 Feature distributions with and without photon smearing. 122
11.4 Comparing PDF effects for different Higgs production modes. 123
11.5 Signal classifier input feature distributions after robust scaling 125
11.6 Signal classifier input feature correlation matrix 126
11.7 Performance metrics of the signal classifier. 129
11.8 Orthogonal discriminant distribution for the signal classifier 130
11.9 Confusion matrix for the orthogonal signal regions. 130
11.10 Invariant mass distribution for the inclusive signal region 131
11.11 Branching ratio and cross-section κ parameterisation. 132
11.12 2D expected limits from the combined signal regions 136
11.13 2D expected limits for full Run 3 dataset 140

B.1 Background rejection input feature distribution after robust scaling . . . 150
B.2 Performance metrics of the background rejection classifier 152
B.3 Discriminant distributions for the background rejection classifier. 153

C.1 2D expected limits in the exclusive signal region. 154

C.2 Invariant mass distribution for the ggF signal region 155
C.3 2D expected limits in the ggF signal region 155
C.4 Invariant mass distribution for the κ_c signal region. 156
C.5 2D expected limits in the κ_c signal region. 156
C.6 Invariant mass distribution for the $\kappa_{u,d}$ signal region 157
C.7 2D expected limits in the $\kappa_{u,d}$ signal region 157

List of Tables

3.1 SM Higgs boson production cross-sections at 13.6 TeV 23

3.2 SM $q\bar{q} \to H$ production cross-sections at 13.6 TeV 25

3.3 Branching ratio of the Higgs boson decay modes. 26

3.4 Kappa Framework parameterisation of Higgs boson properties. 29

3.5 Constraints on the charm coupling from $H \to c\bar{c}$ 33

3.6 Constraints on the light quark couplings from $H \to M\gamma$ 34

3.7 Constraints on the light quark couplings from $H\gamma$ production 34

3.8 Constraints on the charm couplings from $H \to \gamma\gamma$ 39

5.1 Photon trigger requirements for $H \to \gamma\gamma$ analysis. 63

7.1 Quality criteria for track candidates 75

8.1 Diphoton fiducial region selection requirements. 91

8.2 Run 2 $H \to \gamma\gamma$ systematic uncertainties 95

8.3 Constraints on the charm couplings from $H \to \gamma\gamma$ 97

9.1 Selection cutflow in 2022 and 2023 Run 3 datasets 101

9.2 MC samples used in the data validation study. 102

9.3 Selection cutflow in ggF MC samples. 104

10.1 Expected number of events in diphoton fiducial region 113

10.2 $H \to \gamma\gamma$ signal modelling yields for all fiducial regions. 115

11.1 MC simulated signal samples used in signal classifier training 120
11.2 Input features to signal classifier 126
11.3 Architecture of the signal classifier 127
11.4 Definition of orthogonal signal region 129
11.5 Expected limits for the inclusive and combined measurements 134
11.6 Expected composition of events in the inclusive signal region 138
11.7 Expected limits in each individual signal region 139
11.8 Signal and background yields in each signal region 139
11.9 Projected constraints for Run 3 and HL-LHC 140

A.1 Events passing selection criteria to remove VBF, VH and $t\bar{t}H$ 146

B.1 MC simulated samples used in background rejection training 148
B.2 Input features used in background rejection training 149
B.3 Architecture of the background rejection classifier 149
B.4 Discriminant cuts for the background rejection classifier 153

Acronyms

ATLAS A Toriodal LHC Apparatus.

CERN European Council for Nuclear Research.

CSCs Cathode Strip Chambers.

DSCB double-sided Crystal Ball.

ECal Electromagnetic Calorimeter.

eFEX Electromagnetic Feature Extractor.

FCal Forward Calorimeter.

ggF gluon-gluon fusion.

HCal Hadronic Calorimeter.

HEC Hadronic End-Cap.

HL-LHC High Luminosity LHC.

HLT High-Level Trigger.

IBL Insertable B-Layer.

ID Inner Detector.

IS Information Service.

JVF Jet Vertex Fraction.

JVT Jet Vertex Tagger.

L1 Level-1.

L1Calo L1 Calorimeter.

LAr Liquid Argon.

LHC Large Hadron Collider.

LO leading order.

MC Monte Carlo.

MDTs Monitored Drift Tubes.

MET Missing Transverse Energy.

MS Muon Spectrometer.

NLO next-to-leading order.

NNLO next-to-next-to-leading order.

P-BEAST Persistent Back-End for the ATLAS IS system of TDAQ.

PDF parton distribution function.

PMTs photomultiplier tubes.

QCD Quantum Chromodynamics.

QED Quantum Electrodynamics.

$\mathbf{q\bar{q} \to H}$ quark-initiated Higgs production.

RoI region of interest.

RPCs Resistive Plate Chambers.

SCT Semiconductor Tracker.

SM Standard Model of Particle Physics.

TAP trigger after prescale.

TAV trigger after veto.

TDAQ Trigger and Data Acquisition.

TGCs Thin Gap Chambers.

TileCal Tile Calorimeter.

TRP Trigger Rate Presenter.

TRT Transition Radiation Tracker.

$\mathbf{t\bar{t}H}$ associated production of the Higgs boson with a top quark pair.

VBF vector-boson fusion.

VH associated production of the Higgs boson with a vector boson.

Glossary

2022+23+fix SW is the same 2022+23 SW release including a fix to the JVT bug. Also referred to as **2022+2023 SW**.

2022+23 SW is the software release developed for the analysis of the combined 2022+2023 dataset.

2022 SW is the software release developed for the analysis of the 2022 dataset.

Athena is the ATLAS offline software framework developed by members of the collaboration.

bremsstrahlung is the electromagnetic radiation produced by the deceleration of a charged particle as it is deflected by another charged particle, typically an atomic nucleus.

converted photons have pair produced into an electron-positron pair before the calorimeter in the tracking detector. The signature of a converted photon is an energy deposit in the Electromagnetic Calorimeter (ECal) and a matching track (or pair of tracks) in the Inner Detector (ID).

Point-1 is the first interaction point on the LHC ring where the ATLAS detector cavern and control room are located.

prompt photons originate from the hard scatter process. In the context of $H \to \gamma\gamma$, prompt photons are produced in the decay of the Higgs boson.

unconverted photons have pair produced in the calorimeter only. The signature of an unconverted photon is an energy deposit in the Electromagnetic Calorimeter (ECal).

vertex is the point where an interaction between particles occurs. The *primary vertex* defines the location in the detector where the *pp* interaction with the highest momentum transfer between the protons, the so-called *hard process*, takes place.

Chapter 1

Introduction

"The discovery of the Higgs boson is a triumph of human curiosity, ingenuity, and collaboration."

Fabiola Gianotti
CERN Director-General

Following the discovery of the Higgs boson in 2012 by the ATLAS [1] and CMS [2] collaborations at the Large Hadron Collider (LHC), particle physicists have been extensively studying its properties.

The Higgs boson is the only scalar particle in the Standard Model of Particle Physics (SM). Fundamental particles obtain their mass through their interaction with the Higgs boson. This thesis focuses on the Higgs boson coupling to SM fermions, more specifically quarks, referred to as the Yukawa coupling. The SM hypothesises that the Higgs boson couples in proportion to the mass of the fermion. The SM therefore predicts a hierarchy in the Yukawa couplings with the heaviest, third-generation quarks having the strongest coupling to the Higgs boson. The Yukawa coupling is the only interaction in the SM that explicitly depends on the fermion's generation.

Direct measurements of the quark Yukawa couplings can be achieved through a search for kinematically allowed decay channels of the Higgs boson to quark pairs, $H \to q\bar{q}$. Experimentally, the couplings between the Higgs boson and third-generation quarks have been measured and are consistent with the SM [3], as shown in Figure 1.1. Direct measurements of the Yukawa couplings to first- and second-generation quarks, however, have yet to be measured — only upper limits on the charm quark Yukawa coupling have been set by the ATLAS [4] and CMS [5] collaborations. The direct measurement of the Yukawa couplings for up, down and strange quarks is inhibited at the LHC due to the large multi-jet background. Constraints on the light quark Yukawa couplings have been set by probing rare decays of the Higgs boson to a light vector meson and a photon, $H \to M\gamma$ [6]. For example, $H \to \phi\gamma$ and $H \to \rho\gamma$ have been used to constrain the strange and light (up and down) quark Yukawa couplings, respectively.

The direct search for $H \to q\bar{q}$ is limited by the efficiency of determining the quark flavour from the hadronic jets in the final state. Kinematic distributions of the Higgs boson, such as the transverse momentum spectrum, offer an indirect probe of the Yukawa coupling. The transverse momentum is sensitive to quark-initiated Higgs production, $q\bar{q} \to H$, and has a softer distribution compared to the dominant gluon-fusion production due to the lower colour charge of quarks. The ATLAS Experiment applied this technique to constrain the bottom and charm quark Yukawa couplings in the Run 2 $H \to \gamma\gamma$ cross-section measurement [7]. Better exclusion limits were obtained for the charm quark Yukawa coupling from $q\bar{q} \to H \to \gamma\gamma$ production compared to the Run 2 $H \to c\bar{c}$ measurement.

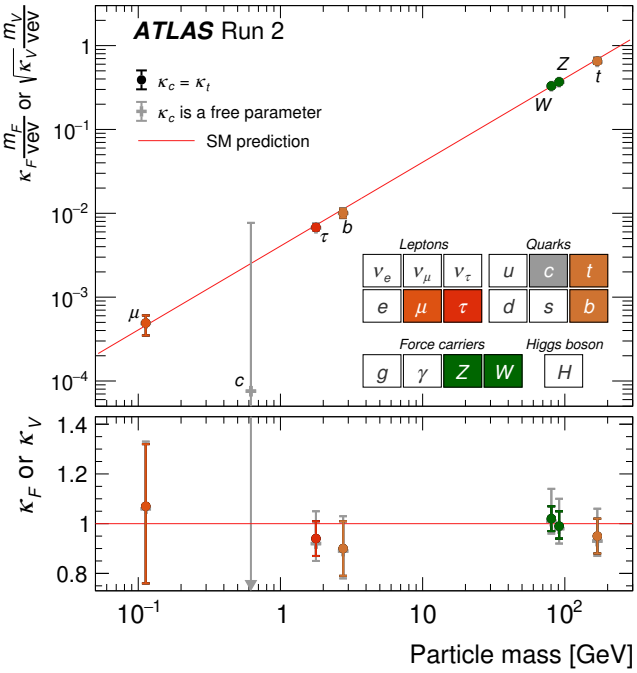

Figure 1.1 *The Higgs boson coupling strength for fermions and vector bosons compared to the SM prediction from Run 2 of the ATLAS Experiment. Figure from Ref. [3].*

Using Run 3 data from the ATLAS Experiment, the aim of this thesis is to improve the technique used in the Run 2 $H \to \gamma\gamma$ cross-section measurement to indirectly probe the Yukawa coupling to the charm and light (up and down) quarks. The innovative approach in this thesis uses a multivariate analysis designed to classify Higgs boson production modes using Higgs kinematics and ultimately improve the sensitivity to the Yukawa couplings. For Run 3, the well-measured bottom quark Yukawa coupling is fixed and new parameters were introduced to probe the first-generation couplings. This thesis uses $58.6\,\text{fb}^{-1}$ of proton-proton collision data collected between 2022 and 2023 at a centre-of-mass energy of $\sqrt{s} = 13.6\,\text{TeV}$. The expected constraints on the charm and light quark Yukawa couplings are found to be weaker than the bottom quark at 95% confidence level. Since the SM predicts a hierarchical structure in Yukawa couplings, with the first- and second-generation couplings smaller than those of the third-generation, this work demonstrates that Higgs kinematics can be used to experimentally establish this hierarchy.

This thesis begins by outlining the foundations on which the work is based. The theoretical background of the SM and, most importantly, the role of the Higgs

boson in the SM is discussed in Chapter 2. Chapter 3 provides an overview of the Higgs boson and its properties in the context of LHC. A literature review of the direct and indirect measurements of the Yukawa couplings is presented. Chapter 4 introduces the ATLAS Experiment at the LHC — the source of the data analysed in this thesis.

Technical work on the development of the ATLAS trigger system for Run 3 data-taking is presented in this thesis. Chapter 5 introduces the trigger system which is designed to select events of interest to keep for further analysis. Chapter 6 discusses two technical projects: the optimisation of the Inner Detector trigger tracking in the High-Level Trigger (HLT); and the development of the Trigger Rate Presenter (TRP).

The remaining chapters focus on the analysis of the $H \to \gamma\gamma$ measurement. Chapter 7 discusses the reconstruction of detector signals into physics objects used in the $H \to \gamma\gamma$ cross-section analysis. Chapter 8 introduces the state-of-the-art techniques used in the Run 2 and early Run 3 publications. Chapter 9 presents the validation of the 2022+2023 Run 3 dataset, corresponding simulated samples and the software developed for the analysis. Chapter 10 discusses the modelling of the $H \to \gamma\gamma$ signal in different regions of phase space probed in the cross-section measurement. Finally, Chapter 11 presents the novel technique developed in this thesis to probe the charm and light quark Yukawa couplings.

Chapter 2

The Standard Model of Particle Physics

The Standard Model of Particle Physics (SM) explains how the fundamental constituents of the Universe interact; it hypothesises that the forces between particles are themselves described by the exchange of particles. The SM is an established and well-tested theory that has successfully explained almost all current experimental data and predicted a wide range of phenomena. In this chapter, I introduce the SM and the Lagrangian formalism used to describe it. Focusing on the role of the Higgs boson in the SM, the Higgs mechanism is introduced as an explanation for the origin of massive vector bosons. Finally, I discuss the Yukawa coupling as a mechanism for the generation of fermion masses — the focus of this thesis.

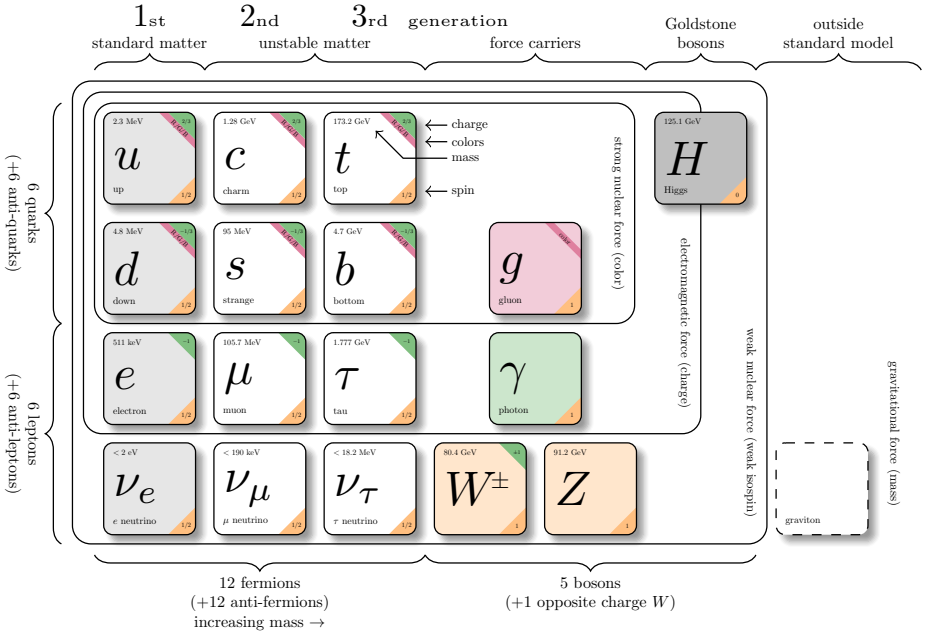

Figure 2.1 *The 17 fundamental particles of the Standard Model of Particle Physics (SM). There are 12 fermions: six quarks and six leptons categorised into three generations. There are five bosons: four force-carrying gauge bosons and the Higgs boson. Figure from Ref. [8].*

2.1 Elementary particles and forces of nature

The Standard Model of Particle Physics (SM) is the theory describing all fundamental constituents of matter and their interactions. In quantum mechanics, particles are categorised into bosons with integer spin and SM fermions with half-integer spin. All matter that can be observed directly is made up of quarks and leptons, both of which are fermions and fundamental particles. SM fermions are categorised into three generations of increasing mass.

There are four known fundamental forces that govern all interactions between fermions, mediated by the exchange of gauge bosons. The electromagnetic force is mediated by the photon, γ, the weak force by the massive $W^{\pm}$ and Z bosons and the strong force by the gluon, g. Gravity is the fourth fundamental force which cannot yet be described consistently with all other interactions in the SM.

The spin-0 Higgs boson is the final particle in the SM, responsible for giving mass to all particles it interacts with. The 17 fundamental particles of the SM are shown in Figure 2.1.

2.2 Lagrangians in Quantum Field Theory

The coupling of the Higgs boson to fermions, the *Yukawa coupling*, enters into the Lagrangian formalism of the SM as a mass term for the fermions. This section introduces the Lagrangian formalism of Quantum Field Theory [9].

In classical dynamics, a Lagrangian, L, for a given system is defined in terms of the kinetic energy, T, and potential energy, V, of the system

$$L = T - V. \tag{2.1}$$

The Lagrangian, $L(q_i, \dot{q}_i)$, is a function of the generalized coordinates q_i and their time derivatives $\dot{q}_i$.

In Quantum Field Theory, single particle wavefunctions are replaced by excitations of a quantum field. The Lagrangian is replaced by the Lagrangian Density, $\mathcal{L}(\phi_i, \partial_\mu \phi_i)$, as a function of the fields $\phi_i(x, y, z, t)$ and the derivatives of the fields $\partial_\mu \phi_i$ with respect to the four space-time coordinates. The field equation is determined by the form of the Lagrangian density — referred to henceforth simply as the Lagrangian. The SM particles and their interactions are described using the Lagrangian formalism of Quantum Field Theory.

The Lagrangian for a spin-0 boson of mass m can be written as

$$\mathcal{L}_S = \frac{1}{2}(\partial_\mu \phi)(\partial^\mu \phi) - \frac{1}{2} m^2 \phi^2. \tag{2.2}$$

Spin-0 scalar particles are described by excitations of the scalar field ϕ satisfying the Klein-Gordon equation: $\partial_\mu \partial^\mu \phi + m^2 \phi = 0$.

The Lagrangian for spin-1/2 fermions of mass m can be written as

$$\mathcal{L}_D = i\bar{\psi}\gamma^\mu \partial_\mu \psi - m\bar{\psi}\psi, \tag{2.3}$$

where $\psi(x)$ is a four-component complex spinor satisfying the Dirac equation

$$(i\gamma^\mu \partial_\mu - m)\psi = 0. \tag{2.4}$$

The Lagrangian for a free photon field, A_μ, is given by

$$\mathcal{L}_\gamma = -\frac{1}{4} F_{\mu\nu} F^{\mu\nu}, \tag{2.5}$$

where $F_{\mu\nu} = \partial_\mu A_\nu - \partial_\nu A_\mu$ is the field-strength tensor. If the photon had mass, the free particle Lagrangian would be modified to

$$\mathcal{L}_{\text{Proca}} = -\frac{1}{4} F_{\mu\nu} F^{\mu\nu} + \frac{1}{2} m_\gamma^2 A_\mu A^\mu, \tag{2.6}$$

known as the *Proca Lagrangian*, describing massive spin-1 bosons.

2.3 The Standard Model Lagrangian

The full SM Lagrangian is presented in expressions 2.7 to 2.11.

$$\mathcal{L}_{\text{SM}} = \underbrace{-\frac{1}{4} W^k_{\mu\nu} W_k^{\mu\nu} - \frac{1}{4} B_{\mu\nu} B^{\mu\nu} - \frac{1}{4} G^a_{\mu\nu} G_a^{\mu\nu}}_{\text{kinetic energies \& self-interactions of the gauge bosons}} \tag{2.7}$$

$$+ \underbrace{\bar{\psi}_L \gamma^\mu \left(i\partial_\mu - g_W \frac{1}{2} \sigma^k W^k_\mu - g' \frac{Y}{2} B_\mu \right) \psi_L + \bar{\psi}_R \gamma^\mu \left(i\partial_\mu - g' \frac{Y}{2} B_\mu \right) \psi_R}_{\text{kinetic energies \& electroweak interactions of fermions}} \tag{2.8}$$

$$+ \underbrace{g_S (\bar{\psi}_q \gamma^\mu \frac{1}{2} \lambda^a \psi_q) G^a_\mu}_{\text{quark gluon interactions}} \tag{2.9}$$

$$+ \underbrace{\frac{1}{2} \left| \left(i\partial_\mu - g_W \frac{1}{2} \sigma^k W^k_\mu - g' \frac{Y}{2} B_\mu \right) \phi \right|^2 - V(\phi)}_{W^\pm,\ \text{Z},\ \gamma \text{ and Higgs masses \& couplings}} \tag{2.10}$$

$$- \underbrace{y_f \left(\bar{\psi}_L \phi \psi_R + (\bar{\psi}_L \phi \psi_R)^\dagger \right) + y_f \left(\bar{\psi}_L \phi_c \psi_R + (\bar{\psi}_L \phi_c \psi_R)^\dagger \right)}_{\text{fermion masses \& couplings to Higgs}} \tag{2.11}$$

The SM Lagrangian combines the theory of the strong, electromagnetic and weak interactions. The electromagnetic interaction between electrically charged particles is described by the Quantum Field Theory of Quantum Electrodynamics (QED) [10]. The strong interaction between quarks and gluons is described by the Quantum Field Theory of Quantum Chromodynamics (QCD) [11, 12]. Electroweak theory [13–15] details the unification of the weak interaction and QED. The SM Lagrangian can therefore be written in the form

$$\mathcal{L}_{\text{SM}} = \mathcal{L}_{\text{QCD}} + \mathcal{L}_{\text{EW}}, \tag{2.12}$$

as the sum of the Lagrangians for QCD and the electroweak theory.

Symmetries play a key role in describing the interactions between particles in the SM. Local gauge symmetry is expressed naturally as the invariance of the Lagrangian under a local phase transformation of the fields. The symmetry group of the SM is written as

$$\mathrm{SU}(3)_C \times \mathrm{SU}(2)_L \times \mathrm{U}(1)_Y. \tag{2.13}$$

The $\mathrm{SU}(3)_C$ symmetry group corresponds to the conservation of colour charge in the strong interaction. The $\mathrm{SU}(2)_L$ symmetry group corresponds to conservation of weak isospin in the electroweak interaction. The $\mathrm{U}(1)_Y$ symmetry group corresponds to conservation of weak hypercharge in the electromagnetic interaction.

The following sections discuss the gauge symmetries of the SM in more detail and the associated interactions that arise from the requirement of local gauge invariance — covering the interactions described in expressions 2.7 to 2.9 in the SM Lagrangian. Whilst the local gauge principle provides an elegant description of SM interactions, subsequent sections discuss how the requirement for local gauge invariance of the SM is broken by particle mass terms in the Lagrangian. The Brout-Englert-Higgs mechanism is introduced as a solution to the problem of massive gauge bosons in the SM — the explanation for expression 2.10 in the SM Lagrangian. Finally, the Yukawa coupling is introduced in the generation of fermion masses and the final term in the SM Lagrangian, expression 2.11.

2.4 Quantum Electrodynamics

For the electromagnetic interaction, the Dirac equation (Equation 2.4) is required to be invariant under the U(1) local phase transformation

$$\psi(x) \rightarrow \psi'(x) = e^{iq\chi(x)}\psi(x). \tag{2.14}$$

The local nature of the gauge transformation means that derivatives acting on the field also act on the local phase $\chi(x)$. The required gauge invariance is restored by replacing the derivative in the Dirac equation with the covariant derivative

$$\partial_\mu \rightarrow D_\mu = \partial_\mu + iqA_\mu, \tag{2.15}$$

where $A_\mu \to A'_\mu = A_\mu - \partial_\mu \chi(x)$ is a new field designed to cancel the extra term introduced by $\partial_\mu \psi'$. The electric charge is denoted by q. Introducing the covariant derivative into the spin-1/2 fermion Lagrangian in Equation 2.3, a new term is established describing the interaction between the fermion and photon fields of the form $q\bar{\psi}\gamma^\mu A_\mu \psi$. The requirement that physics is invariant under local U(1) phase transformations therefore arises in the interaction between fermions and the photon.

Introducing the kinetic term for the photon, $F_{\mu\nu}F^{\mu\nu}$, the Lagrangian of QED is given by

$$\mathcal{L}_{\text{QED}} = \bar{\psi}(i\gamma^\mu \partial_\mu - m)\psi + q\bar{\psi}\gamma^\mu \psi A_\mu - \frac{1}{4}F_{\mu\nu}F^{\mu\nu}, \tag{2.16}$$

where $F_{\mu\nu} = \partial_\mu A_\nu - \partial_\nu A_\mu$ is the electromagnetic field strength tensor.

2.5 Quantum Chromodynamics

The underlying symmetry associated with the strong interaction is invariance under $\text{SU}(3)_C$ local phase transformations

$$\psi(x) \to \psi'(x) = e^{ig_S \boldsymbol{\alpha}(x)\cdot \hat{\boldsymbol{T}}}\psi(x), \tag{2.17}$$

where g_S is the strong coupling constant and $\boldsymbol{\alpha}(x)$ consists of eight functions of space-time coordinate x. $\hat{\boldsymbol{T}} = \{T^a\}$ are the generators of the $\text{SU}(3)_C$ symmetry group related to the eight Gell-Mann matrices by $T^a = \frac{1}{2}\lambda^a$. Since the $\text{SU}(3)_C$ generators are 3×3 matrices, the fermion wavefunction, $\psi(x)$, must now include three additional degrees of freedom corresponding to the three *colours* of the strong interaction: red, green and blue. The Dirac equation (Equation 2.4) for the $\text{SU}(3)_C$ local gauge transformation becomes

$$i\gamma^\mu \left[\partial_\mu + ig_S(\partial_\mu \boldsymbol{\alpha}) \cdot \hat{\boldsymbol{T}}\right] \psi = m\psi. \tag{2.18}$$

The required local gauge invariance can be maintained by introducing eight new fields $G^a_\mu(x)$, $a = 1, \ldots, 8$, corresponding to eight different colour combinations of gluons that mediate the strong force. Including the interactions with the new gauge fields, the Dirac equation takes the form

$$i\gamma^\mu \left[\partial_\mu + ig_S \frac{1}{2}\lambda^a G^a_\mu\right] \psi = m\psi. \tag{2.19}$$

This restores the invariance under local $\mathrm{SU}(3)_C$ phase transformations, provided that the new fields transform as $G^k_\mu \to G^{k'}_\mu = G^k_\mu - \partial_\mu \alpha_k - g_S f_{ijk} \alpha_i G^i_\mu$ where f_{ijk} are the structure constants of the $\mathrm{SU}(3)_C$ group. The last term is a consequence of $\mathrm{SU}(3)_C$ generators not commuting with each other and gives rise to the self-interactions of the gluon fields.

The Lagrangian for QCD therefore takes the form

$$\mathcal{L}_{\mathrm{QCD}} = \bar{\psi}_q (i\gamma^\mu \partial_\mu - m_q)\psi_q + g_S \bar{\psi}_q \gamma^\mu \frac{1}{2}\lambda^a \psi_q G^a_\mu - \frac{1}{4} G^a_{\mu\nu} G^{a\mu\nu}, \tag{2.20}$$

following the same methodology as in QED whilst enforcing gauge invariance under the $\mathrm{SU}(3)_C$ symmetry group.

2.6 Electroweak Theory

In the 1960s, Sheldon Glashow [13], Abdus Salam [14] and Steven Weinberg [15] developed the unified electroweak model that describes both the electromagnetic and weak interactions. Two additional quantum numbers are introduced to describe the electroweak interactions: the two-component weak isospin, I_W, and weak hypercharge, Y. The two components of weak isospin are total weak isospin and the third component of weak isospin, $I^{(3)}_W$. The electric charge, Q, is related to the weak isospin and weak hypercharge by

$$Q = I^{(3)}_W - \frac{Y}{2}. \tag{2.21}$$

In the electroweak model, the U(1) symmetry of electromagnetism is replaced with a new $\mathrm{U}(1)_Y$ local gauge symmetry

$$\psi(x) \to \psi'(x) = \hat{U}(x)\psi(x) = e^{ig'\frac{Y}{2}\zeta(x)}\psi(x), \tag{2.22}$$

giving rise to a new gauge field B_μ that couples to a new kind of charge, the weak hypercharge. The resulting interaction term takes the form $g'\frac{Y}{2}\gamma^\mu B_\mu \psi$ which has the same structure as the QED interaction arising from the U(1) symmetry in Equation 2.16 with the replacement $q \to g'\frac{Y}{2}$.

The weak interaction is derived by extending the local gauge principle, requiring

that the Lagrangian remain invariant under the SU(2) local phase transformations

$$\varphi(x) \rightarrow \varphi'(x) = e^{ig_W \boldsymbol{\alpha}(x)\cdot\boldsymbol{T}}\varphi(x), \tag{2.23}$$

where g_W is the weak coupling constant and $\boldsymbol{\alpha}(x)$ consists of three functions specifying the local phase at each point in spacetime. $\boldsymbol{T} = \frac{1}{2}\boldsymbol{\sigma}$ defines the generators of the SU(2) group in terms of the Pauli spin matrices. Since the generators of the SU(2) gauge transformation are 2×2 matrices, the wavefunction, $\varphi(x)$, is written in terms of two components known as the *weak isospin doublet*. An example weak isospin doublet is given by

$$\varphi(x) = \begin{pmatrix} \nu_e \\ e^- \end{pmatrix}_L \tag{2.24}$$

where both components are left-handed chiral spinors. The total weak isospin of the doublet is $I_W = +1/2$ and the third component of weak isospin is $I_W^{(3)}(\nu_e) = +1/2$ and $I_W^{(3)}(e^-) = -1/2$. Since the weak charged-current interaction associated with the $W^\pm$ boson couples together different fermions, the doublet must contain flavours differing by one unit charge. Moreover, the W boson only acts on left-handed chiral states; the doublet in Equation 2.24 therefore contains only left-handed chiral states. For this reason, the symmetry group of the weak interaction is referred to as $\mathrm{SU}(2)_L$. Charged fermions also have right-handed chiral states which sit in *weak isospin singlets* and are unaffected by the $\mathrm{SU}(2)_L$ gauge transformation.

Gauge invariance is achieved by replacing ∂_μ with D_μ which involves the generators of the symmetry group. The covariant derivative for the SU(2) group is given by

$$D_\mu = \partial_\mu - ig_W \boldsymbol{T}\cdot\boldsymbol{W}_\mu(x) \tag{2.25}$$

$$= \partial_\mu - ig_W \frac{1}{2}\sigma_k W_\mu^{(k)}(x). \tag{2.26}$$

Local gauge invariance is satisfied by introducing three gauge fields $W_\mu^{(k)}$, $k = 1, 2, 3$. Introducing the parameter θ_W as the weak mixing angle, the physical

gauge bosons of the electroweak interaction are defined as

$$W^{\pm} = \frac{1}{\sqrt{2}}(W^{(1)} \mp iW^{(2)}), \tag{2.27}$$

$$A_\mu = B_\mu \cos\theta_W + W_\mu^{(3)} \sin\theta_W, \tag{2.28}$$

$$Z_\mu = -B_\mu \sin\theta_W + W_\mu^{(3)} \cos\theta_W. \tag{2.29}$$

The electroweak Lagrangian is therefore given by

$$\mathcal{L}_{\text{EW}} = \bar{\psi}_L \gamma^\mu \left(i\partial_\mu - g_W \frac{1}{2}\sigma^k W_\mu^k - g' \frac{Y}{2} B_\mu \right) \psi_L \tag{2.30}$$

$$+ \bar{\psi}_R \gamma^\mu \left(i\partial_\mu - g' \frac{Y}{2} B_\mu \right) \psi_R \tag{2.31}$$

$$- \frac{1}{4} W_{\mu\nu} W^{\mu\nu} - \frac{1}{4} B_{\mu\nu} B^{\mu\nu}. \tag{2.32}$$

2.7 Particle masses

At this point, the QCD and electroweak Lagrangians have been introduced, consistent with expressions 2.7 to 2.9 in the SM Lagrangian. The form of the SM Lagrangian in Equation 2.12, however, is currently incomplete as it does not include mass terms for the gauge bosons or fermions.

If the photon field had mass, the QED Lagrangian in Equation 2.16 would be modified to include an additional mass term of $\frac{1}{2}m_\gamma^2 A_\mu A^\mu$, as demonstrated in Equation 2.6. The photon mass term is not gauge invariant. The required U(1) local gauge symmetry is therefore only satisfied if the interaction gauge boson is massless; this also applies to the $\text{SU}(2)_L$ and $\text{SU}(3)_C$ gauge symmetries. This is an apparent contradiction with the observation of the large masses of the W and Z bosons.

The mass problem is not restricted to the gauge bosons. For the electron spinor field, $\psi = e$, the electron mass term in Equation 2.16 can be written in terms of the chiral particle states as

$$-m_e \, \bar{e} \, e = m_e \left(\bar{e}_L \, e_R + \bar{e}_R \, e_L \right). \tag{2.33}$$

The $\text{SU}(2)_L$ gauge transformation of the weak interaction dictates that left-handed particles transform as weak isospin doublets and right-handed particles

as weak isospin singlets. The mass term in Equation 2.33 therefore breaks the required gauge invariance.

2.8 The Brout-Englert-Higgs mechanism

The proposed solution to the problem of the massive $W^{\pm}$ and Z gauge bosons in the SM is the mechanism of *spontaneous symmetry breaking* — a phenomenon where the ground state of a system does not obey the symmetry of the Lagrangian. This idea was introduced by Peter Higgs [16], Francois Englert and Robert Brout [17] in the context of electroweak $\mathrm{SU}(2)_L \times \mathrm{U}(1)_Y$ symmetry breaking in what is now referred to as the Brout-Englert-Higgs mechanism.

In the Brout-Englert-Higgs mechanism, a new field ϕ is introduced with a characteristic self interaction that leads to spontaneous symmetry breaking in the quantum vacuum. The simplest model consists of two complex scalar fields, ϕ^+ and ϕ^0, placed in a weak isospin doublet

$$\phi = \begin{pmatrix} \phi^+ \\ \phi^0 \end{pmatrix} = \frac{1}{\sqrt{2}} \begin{pmatrix} \phi_1 + i\phi_2 \\ \phi_3 + i\phi_4 \end{pmatrix}, \tag{2.34}$$

where ϕ_1, ϕ_2, ϕ_3 and ϕ_4 are real scalar fields. Since the Brout-Englert-Higgs mechanism is required to generate the masses of the electroweak gauge bosons, one of the scalar fields must be neutral, ϕ^0. The other field, ϕ^+, is charged such that $(\phi^+)^* = \phi^-$ to give the longitudinal polarisation states of the $W^{\pm}$ bosons. The Lagrangian for the doublet of complex scalar fields in Equation 2.34 is given by

$$\mathcal{L} = (\partial_\mu \phi)^\dagger (\partial^\mu \phi) - V(\phi), \tag{2.35}$$

where $V(\phi)$ is the Higgs potential:

$$V(\phi) = \frac{1}{2}\mu^2 \phi^\dagger \phi + \frac{1}{4}\lambda(\phi^\dagger \phi)^2. \tag{2.36}$$

For $\mu^2 < 0$, the potential has an infinite set of degenerate minima satisfying

$$\phi^\dagger \phi = (\phi_1^2 + \phi_2^2 + \phi_3^2 + \phi_4^2) \equiv v^2 = \frac{-\mu^2}{\lambda}, \tag{2.37}$$

where $v = \sqrt{-\mu^2/\lambda}$ is the vacuum expectation value of the field ϕ. The shape of the Higgs potential is shown in Figure 2.2.

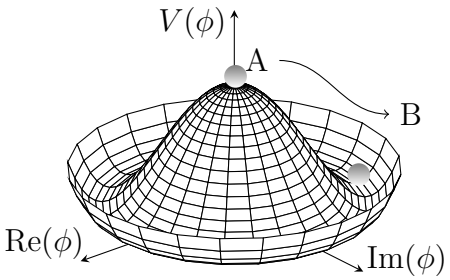

Figure 2.2 *Shape of the Higgs potential $V(\phi)$ in Equation 2.36. Figure from Ref. [18].*

After symmetry breaking, the neutral photon is required to remain massless. The minimum of the potential must therefore correspond to a non-zero vacuum expectation value only of the neutral field:

$$\phi_0 = \begin{pmatrix} 0 \\ v \end{pmatrix}. \tag{2.38}$$

Considering a small field excitation, $h(x)$, Equation 2.38 can be written as

$$\phi(x) = \begin{pmatrix} 0 \\ v + h(x) \end{pmatrix}. \tag{2.39}$$

Expanding the Higgs potential in Equation 2.36 around the minimum by a small field excitation, $h(x)$, the potential can be written as

$$V(\phi) = -\frac{1}{2}\lambda v^4 + \lambda v^2 h^2 + \lambda v h^3 + \frac{1}{4}\lambda h^4. \tag{2.40}$$

From the Lagrangian for spin-0 particles in Equation 2.2, the $\lambda v^2 h^2$ term is recognised as a massive spin-0 boson with mass $m_h = \sqrt{2\lambda}v$. The excitation of the field therefore corresponds to the spin-0 Higgs boson. The $\lambda v h^3$ and λh^4 terms are self-interactions of the Higgs boson whilst the λv^4 term is a constant with no physical consequences.

To determine how the Higgs boson interacts with the electroweak gauge bosons, the covariant derivative in Equation 2.25 can be applied to the Higgs field in Equation 2.39:

$$D_\mu \phi = \left(\partial_\mu - i g_W \frac{1}{2}\sigma^k W_\mu^k - i g' \frac{Y}{2} B_\mu\right) \begin{pmatrix} 0 \\ v + h(x) \end{pmatrix}. \tag{2.41}$$

From the Higgs Lagrangian in Equation 2.35, the term responsible for generating

the masses of the gauge bosons is $(D_\mu\phi)^\dagger(D^\mu\phi)$. From the Lagrangian for spin-0 bosons in Equation 2.2, terms that are quadratic in the gauge boson fields are identified as the mass terms of the gauge bosons. The mass term for the W bosons is given by

$$\frac{1}{8}v^2 g_W^2 \left(W_\mu^{(1)} W^{(1)\mu} + W_\mu^{(2)} W^{(2)\mu}\right), \tag{2.42}$$

resulting in a mass of $m_W = \frac{1}{2} g_W v$. The mass term for the neutral gauge bosons from $(D_\mu\phi)^\dagger(D^\mu\phi)$ is given by

$$\frac{1}{8}v^2 \left(g_W W_\mu^{(3)} - g' B_\mu\right)\left(g_W W^{(3)\mu} - g' B^\mu\right). \tag{2.43}$$

Written in terms of the mass matrix for the neutral gauge bosons, $\boldsymbol{M}$, gives

$$\frac{1}{8}v^2 \begin{pmatrix} W_\mu^{(3)} & B_\mu \end{pmatrix} \begin{pmatrix} g_W^2 & -g_W g' \\ -g_W g' & g'^2 \end{pmatrix} \begin{pmatrix} W^{(3)\mu} \\ B^\mu \end{pmatrix} = \frac{1}{8}v^2 \begin{pmatrix} W_\mu^{(3)} & B_\mu \end{pmatrix} \boldsymbol{M} \begin{pmatrix} W^{(3)\mu} \\ B^\mu \end{pmatrix}.$$

The eigenvalues of $\boldsymbol{M}$ generate the masses of the physical neutral gauge bosons

$$\frac{1}{2} \begin{pmatrix} A_\mu & Z_\mu \end{pmatrix} \begin{pmatrix} m_\gamma^2 & 0 \\ 0 & m_Z^2 \end{pmatrix} \begin{pmatrix} A^\mu \\ Z^\mu \end{pmatrix} = \frac{1}{8}v^2 \begin{pmatrix} A_\mu & Z_\mu \end{pmatrix} \begin{pmatrix} 0 & 0 \\ 0 & g_W^2 + g'^2 \end{pmatrix} \begin{pmatrix} A^\mu \\ Z^\mu \end{pmatrix} \tag{2.44}$$

identifying two neutral gauge bosons with $m_\gamma = 0$ and $m_Z = \frac{1}{2} v \sqrt{g_W^2 + g'^2}$.

To summarise, the Brout-Englert-Higgs mechanism generates the masses of the $W^\pm$ and Z bosons and ultimately derives expression 2.10 in the SM Lagrangian. The fermion masses and the final term in the SM Lagrangian (expression 2.11), however, still require further explanation.

2.9 Fermion masses and the Yukawa coupling

From Section 2.7, fermion mass terms violate the local $\mathrm{SU}(2)_L \times \mathrm{U}(1)_Y$ gauge symmetry due to the unequal splitting in left-handed and right-handed chiral states. Giving mass to leptons without breaking the gauge symmetry can be achieved by introducing a coupling between the lepton doublet to the Higgs boson

field ϕ. For the electron, $\psi = e$, the Lagrangian takes the form

$$\begin{aligned}\mathcal{L}^{e}_{\text{Yukawa}} &= -y_e \left(\bar{\psi}_L \, \phi \, \psi_R + \bar{\psi}_R \, \phi^\dagger \, \psi_L\right) \\ &= -y_e \left[\left(\bar{\nu_e}, \bar{e}\right)_L \begin{pmatrix}\phi^+ \\ \phi^0\end{pmatrix} e_R + \bar{e_R} \left(\phi^{+*} \phi^{0*}\right) \begin{pmatrix}\nu_e \\ e\end{pmatrix}_L\right], \end{aligned} \tag{2.45}$$

where y_e is the Yukawa coupling of the electron to the Higgs field. The electron Yukawa Lagrangian is therefore written as

$$\mathcal{L}^{e}_{\text{Yukawa}} = -\frac{y_e}{\sqrt{2}} v \left(\bar{e}_L \, e_R + \bar{e}_R \, e_L\right) - \frac{y_e}{\sqrt{2}} h \left(\bar{e}_L \, e_R + \bar{e}_R \, e_L\right) \tag{2.46}$$

$$= -m_e \left(\bar{e}_L \, e_R + \bar{e}_R \, e_L\right) - \frac{m_e}{v} h \left(\bar{e}_L \, e_R + \bar{e}_R \, e_L\right), \tag{2.47}$$

where $y_e \equiv \sqrt{2} m_e / v$. The Yukawa coupling is not predicted by the Higgs mechanism but is chosen to be consistent with the observed masses of the fermions. The first term gives mass to the electron and represents the coupling of the electron to the Higgs field through its non-zero vacuum expectation value. The second term gives rise to a coupling between the electron and the Higgs boson. As denoted in Equation 2.39, the non-zero expectation value of the Higgs field is in the lower component of the doublet. The combination of fields $\bar{\psi}_L \, \phi \, \psi_R + \bar{\psi}_R \, \phi^\dagger \, \psi_L$ therefore only generates the masses of the charged leptons and the down-type quarks. A separate mechanism is required to give masses to the up-type quarks.

To generate the masses of the up-type quarks, the conjugate doublet ϕ_c is constructed from the four fields in Equation 2.34 as

$$\phi_c = i\sigma_2 \, \phi^* = \begin{pmatrix}-\phi^{0*} \\ \phi^-\end{pmatrix} = \frac{1}{\sqrt{2}} \begin{pmatrix}-\phi_3 + i\phi_4 \\ \phi_1 - i\phi_2\end{pmatrix}. \tag{2.48}$$

Defining the up-type quark Yukawa coupling as $y_u \equiv \sqrt{2} m_u / v$, a local gauge invariant mass term for the up-type quarks can be constructed as

$$\mathcal{L}^{u}_{\text{Yukawa}} = y_u (\bar{\psi}_L \, \phi_c \, \psi_R + \bar{\psi}_R \, \phi_c^\dagger \, \psi_L) \tag{2.49}$$

$$= -m_u \left(\bar{u}_L \, u_R + \bar{u}_R \, u_L\right) - \frac{m_u}{v} h \left(\bar{u}_L \, u_R + \bar{u}_R \, u_L\right). \tag{2.50}$$

Combining Equations 2.46 and 2.49, expression 2.11 is derived.

To conclude this chapter, all the terms in the SM Lagrangian, expressions 2.7 to 2.11, have been derived. The final term in the SM Lagrangian, which includes the Yukawa couplings of fermions to the Higgs field, is the focus of this thesis.

Chapter 3

The Higgs boson at the Large Hadron Collider

The previous chapter introduced the SM and the motivation for the Higgs boson. In this chapter, I focus on the Higgs boson in the context of the Large Hadron Collider (LHC) since its discovery in 2012. An essential starting place is how particle physicists take the theory discussed in the previous chapter and explore it at an experiment. Important properties of the Higgs boson at the LHC are discussed, including its production and decay modes, resulting in its discovery. The remainder of the chapter focuses specifically on measurements of the Yukawa coupling at the LHC. I introduce the parameterisation required to measure the Yukawa coupling and discuss the current status of these measurements — forming the benchmark for this thesis.

3.1 From theory to experiment

For Run 3 of the ATLAS Experiment, proton-proton (pp) collisions take place a centre-of-mass energy of 13.6 TeV. A proton is a bound state composed of three *valence quarks* (uud). The strong interaction, mediated by the exchange of gluons, is responsible for keeping the quarks bound together. The mediating gluons can also produce quark-antiquark pairs, known as *sea quarks*. The composition of the proton during collisions at the LHC can therefore include any of the valence quarks, sea quarks or gluons — collectively known as *partons*.

In QCD, the strong coupling constant, α_s, decreases with energy. This is known as *asymptotic freedom* and is characterised by the running of the coupling constant $\alpha_s(Q)$ with the energy scale Q of the process. Similarly, masses also run with energy scale. Both the running couplings and masses therefore depend on the *renormalisation scale*, μ_R. Common practice is to set $\mu_R^2 = Q^2$ where Q is the energy scale of the process.

At high energies, the partons in the proton are asymptotically free. This implies that as protons collide at the LHC, individual partons can be viewed as independently interacting with partons from the other colliding proton in the hard-scatter process.

3.1.1 Parton distribution functions

The *cross-section* quantifies the probability of any given process taking place in a collision. The cross-section of pp collisions is dominated by the parton scattering processes described by the *parton model*. For a very energetic proton with momentum P_i, the partons will have a collinear momentum p_i given by

$$p_i = x_i P_i,\ 0 \leq x_i \leq 1, \tag{3.1}$$

where x_i is the fraction of the proton momentum carried by the parton. Since quarks and gluons are fundamental particles, perturbative QCD can be applied to calculate their cross-section. The total hadronic cross-section has the form

$$\sigma = \sum_{i,j} \int_0^1 dx_1 \int_0^1 dx_2 f_i(x_1, \mu_F^2) f_j(x_2, \mu_F^2) \hat{\sigma}_{ij}\left(x_i, \mu_F^2, \{p_i, p_j\}\right), \tag{3.2}$$

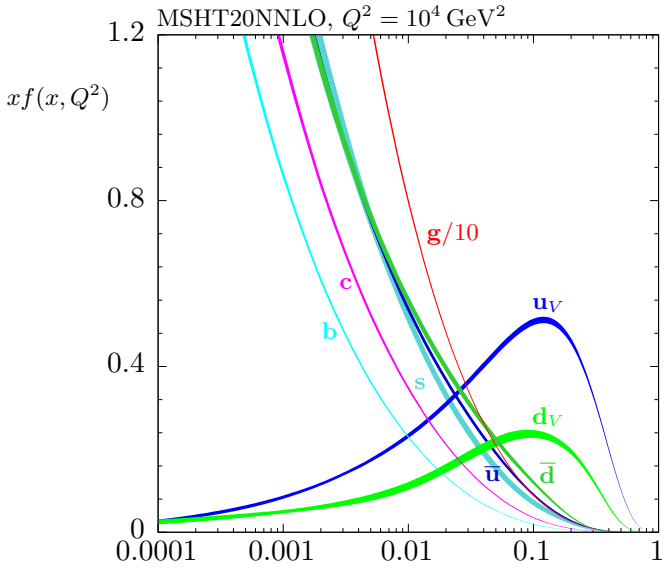

Figure 3.1 *An example parton distribution function (PDF) at $Q^2 = 10^4\ GeV^2$ as a function of the momentum fraction, x_i. The gluon PDF, the red line labelled $g/10$, has been scaled down by a factor of 10. The uncertainty on the PDF is represented by the line width. Figure taken from Ref. [19].*

where the following apply:

- $\hat{\sigma}_{ij}$ is the *partonic cross-section* with i and j denoting the species of the colliding particle;
- $f_i(x_k)$ is the *parton distribution function (PDF)* that describes the probability of finding parton i with momentum fraction x_k in proton k;
- μ_F is the *factorisation scale* separating perturbative and non-perturbative physics, typically set to the energy scale of the process ($\mu_F = Q$); and
- the integrals over the variables $\{x_i\}$ sum over all possible momentum fractions to calculate the total cross-section.

The PDFs by themselves are not physical observables; only the total hadronic cross-section is directly measurable which combines the PDFs with the partonic cross-sections. A graphical representation of a PDF at $Q^2 = 10^4\,\mathrm{GeV}^2$ as a function of x_i is shown in Figure 3.1. The amplitude of the scattering matrix element is used to calculate the partonic cross-section, summing over all allowed processes. This calculation can be done perturbatively, applying the *Feynman rules* at varying degrees of accuracy [20].

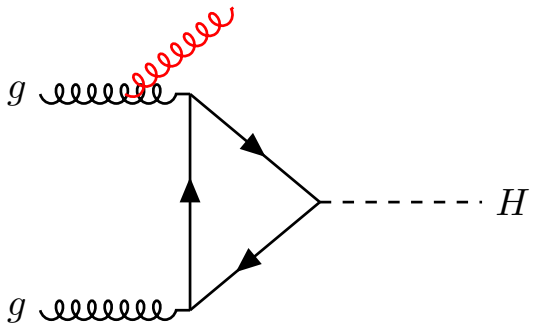

Figure 3.2 *Example Feynman diagrams for the $gg \to H$ process at leading order (LO) (black lines) and next-to-leading order (NLO) (black and red lines).*

3.1.2 Feynman rules

In the 1940s, Richard Feynman devised the Feynman rules to pictorially represent the mathematics behind perturbation theory — known as *Feynman diagrams* [10].

There are two types of lines (sometimes referred to as *legs*) in a Feynman diagram: *external* and *internal* lines. External lines are associated with particles and anti-particles; these are *real* particles that can be observed. For fermions, an arrow is drawn on the line to indicate the direction of the four-momentum. The arrow is reversed to represent anti-particles, interpreted as travelling backwards in time. Internal lines are associated with *virtual* particles that are never observed but are absorbed by, or decay into, real particles. Virtual particles are not required to obey the physical relation $p^2 = E^2 - |\vec{p}^{\,2}| = m^2$ and are commonly known as 'off the mass shell' (or *off-shell*) particles. Real particles are therefore *on-shell*.

For a given process, the Feynman rules can be used to calculate the scattering amplitude by summing over all allowed Feynman diagrams. The lowest possible order in the scattering amplitude is known as leading order (LO). The next order is known as next-to-leading order (NLO) and the n^{th} order is N^{n}LO. To increase the order of a Feynman diagram, additional vertices are added. They can take the form of initial or final state radiation or virtual corrections (known as *loops*). An example LO and NLO Feynman diagram is shown in Figure 3.2.

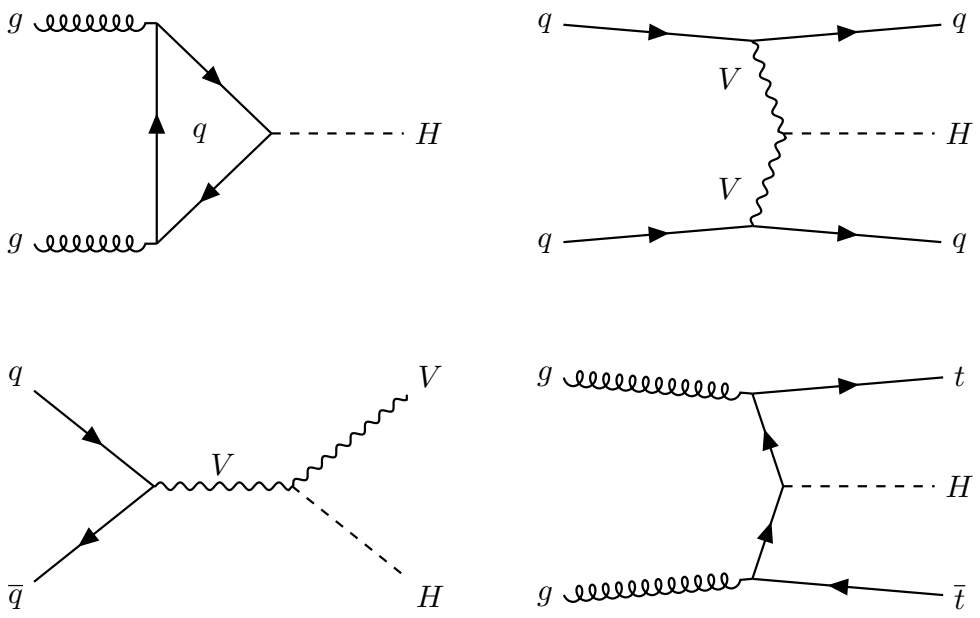

Figure 3.3 *Feynman diagrams for the four main production modes of the Higgs boson at the LHC at LO: (top left) ggF; (top right) VBF; (bottom left) VH; and (bottom right) $t\bar{t}H$.*

3.2 Production modes

There are four main production modes of the Higgs boson at the LHC:

1. gluon-gluon fusion (ggF);
2. vector-boson fusion (VBF);
3. associated production of the Higgs boson with a vector boson (VH); and
4. associated production of the Higgs boson with a top quark pair ($t\bar{t}H$).

Figure 3.3 shows the Feynman diagrams for each of these production modes at LO. The SM predictions for the Higgs boson production cross-sections at 13.6 TeV are presented in Table 3.1, illustrating ggF as the dominant production mode of the Higgs boson and the largest mechanism at a hadron collider. The cross-sections increase with the centre-of-mass energy of the colliding protons as shown in Figure 3.4.

The focus of this thesis is on the Yukawa coupling between the Higgs boson and quarks. The only production modes sensitive to quark couplings are ggF and quark-initiated Higgs production ($q\bar{q} \to H$).

Table 3.1 *SM predictions for the Higgs boson production cross-section, σ, values at 13.6 TeV. The theoretical uncertainties, denoted by $\Delta(\sigma)$, account for missing higher-order QCD corrections, uncertainties in the PDFs and knowledge of the strong coupling constant, α_s. All values are consistent with a Higgs boson mass of 125.09 GeV and are taken from Ref. [21].*

Production mode	σ [pb]	$\Delta(\sigma)$ [%]	Accuracy (of σ)
ggF	52.17	$^{+6.8}_{-8.3}$	N3LO QCD + NLO EW
VBF	4.075	$^{+2.2}_{-2.2}$	NNLO QCD + NLO EW
$pp \to WH$	1.453	$^{+1.8}_{-1.9}$	NNLO QCD + NLO EW
$pp \to ZH$	0.9422	$^{+4.1}_{-4.1}$	NNLO QCD + NLO EW
$t\bar{t}H$	0.5688	$^{+7.0}_{-10.0}$	NNLO QCD + NLO EW

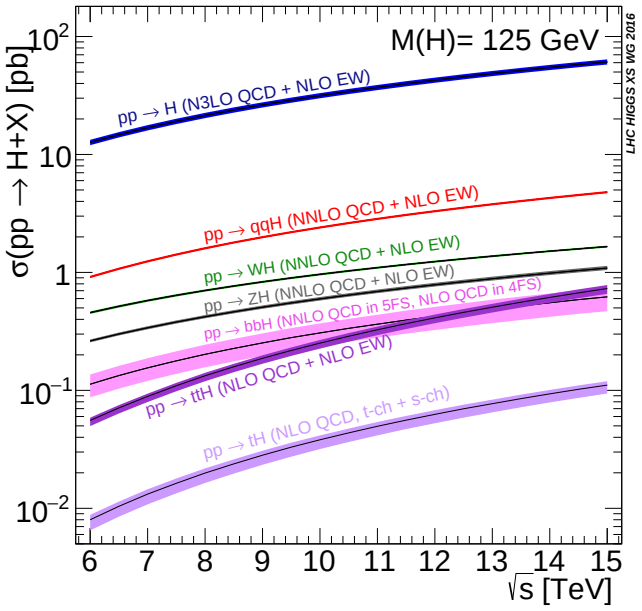

Figure 3.4 *The Higgs boson production cross-sections as a function of the centre-of-mass energy, $\sqrt{S}$, of the colliding protons. Figure from Ref. [22].*

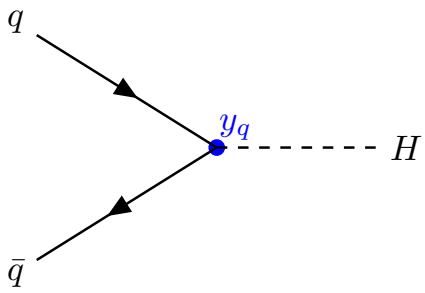

Figure 3.5 *The leading order Feynman diagram for* quark-initiated Higgs production *($q\bar{q} \to H$). The vertex for the Higgs boson coupling to quarks is proportional to the Yukawa coupling, y_q.*

3.2.1 Gluon-gluon fusion Higgs production

As discussed previously, when colliding protons, or more generally hadrons, there is a large gluon density. The Higgs boson, however, does not couple directly to gluons since they are massless. Gluons interact with other particles carrying colour charge, namely quarks and gluons. Since quarks have a non-zero mass, they can couple directly to the Higgs boson. Higgs production through ggF is therefore mediated by a quark loop. The Yukawa coupling is proportional to quark mass and so the dominant contribution to the quark loop is from the top quark (e.g. σ^{tt}_{ggF}) — the most massive quark. All quark flavours, however, contribute to the loop. Moreover, interference can take place between different quarks within the loop.

3.2.2 Quark-initiated Higgs production

Inclusive quark-initiated Higgs production accounts for contributions from both quark-quark ($q\bar{q}$) and gluon-quark (gq) initial states. It is possible for both sea quarks and the light valence quarks to form a Higgs boson through $q\bar{q} \to H$. The vertex for the Higgs boson coupling to quarks is proportional to the Yukawa coupling, y_q, as shown in Figure 3.5.

The state-of-the-art cross-section for bottom-quark-initiated Higgs production ($b\bar{b} \to H$) at 13 TeV [23] is given by

$$\sigma_{b\bar{b}\to H} = \left(0.529 \pm 9.7\%\,(\text{perturbative})\,^{+2.2\%}_{-3.0\%}(\text{PDF})\right)\ \text{pb}. \tag{3.3}$$

The state-of-the-art cross-section for charm-quark-initiated Higgs production

$(c\bar{c} \to H)$ at 13 TeV [24] is given by

$$\begin{aligned}\sigma_{c\bar{c}\to H} &= \left(1.64 \cdot \frac{m_c^2}{m_b^2} \pm 4.9\%\,(\text{perturbative}) \pm 2.4\%\,(\text{PDF})\right)\ \text{pb} \\ &= 0.077 \pm 0.004\ \text{pb},\end{aligned} \tag{3.4}$$

where $m_c^2/m_b^2 \approx 0.049$. Both Equation 3.3 and Equation 3.4 are calculated at NNLO accuracy and assume the SM value of the bottom and charm quark Yukawa couplings respectively.

To estimate the cross-sections at 13.6 TeV for Run 3, the 13 TeV cross-section is multiplied by a scale factor, $\text{SF}_{13.6\,\text{TeV}}$, determined from the ratio of the ggF cross-sections at 13.6 TeV (see Table 3.1) and 13 TeV (48.51 pb [25]):

$$\text{SF}_{13.6\,\text{TeV}} = \frac{52.17\,\text{pb}\ (13.6\,\text{TeV})}{48.51\,\text{pb}\ (13\,\text{TeV})} = 1.075. \tag{3.5}$$

Both cross-sections are calculated to N3LO QCD + NLO EW accuracy. The $b\bar{b} \to H$ and $c\bar{c} \to H$ cross-sections at 13.6 TeV are approximately 0.569 pb and 0.083 pb respectively.

In this thesis, the focus is on light-quark-initiated production of the Higgs boson ($u\bar{u} \to H$ and $d\bar{d} \to H$) whilst also considering $c\bar{c} \to H$. For the light quarks, there are no NNLO predictions for the cross-section available in the literature. The cross-sections are therefore estimated as follows: using MadGraph5_aMC@NLO [26], the cross-section is calculated at NLO QCD accuracy; a NNLO/NLO scale factor is estimated for $c\bar{c} \to H$ production using the NNLO cross-section in Equation 3.4; and finally the scale factor is applied to the $u\bar{u} \to H$ and $d\bar{d} \to H$ processes. The resulting SM cross-section values for $q\bar{q} \to H$ production at 13.6 TeV are presented in Table 3.2 where the coupling strengths are normalised to SM bottom quark Yukawa coupling, y_b^{SM}.

Table 3.2 *The $q\bar{q} \to H$ production cross-section values at 13.6 TeV where the Yukawa couplings are normalised to the SM bottom quark Yukawa coupling (y_b^{SM}).*

Production mode	Yukawa coupling	Cross-section [pb]
$c\bar{c} \to H$	$y_c = y_b^{SM}$	1.76
$u\bar{u}, d\bar{d} \to H$	$y_u = y_d = y_b^{SM}$	22.92

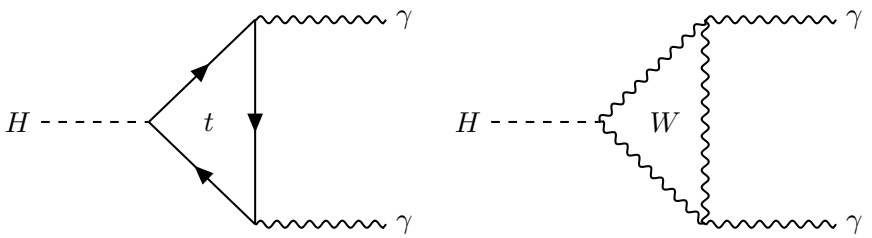

Figure 3.6 *Feynman diagrams at LO for the Higgs boson decay to two photons through (left) a virtual top quark loop and (right) a virtual W boson loop.*

3.3 Decay channels

The total decay width of the Higgs boson, Γ_H, is given by the sum of the partial decay widths, Γ_i, of all possible decay modes

$$\Gamma_H = \sum_i \Gamma_i = 4.07 \text{ MeV}, \tag{3.6}$$

equivalent to a lifetime of 1.56×10^{-22} s [25].

Table 3.3 presents the branching ratios of the dominant Higgs boson decay modes. The Higgs boson couples preferentially to the most massive particles in the SM that are kinematically accessible. The branching ratios are therefore greater for decays of the Higgs boson to massive particles.

Table 3.3 *Predicted branching ratio of the Higgs boson decay modes in the SM. All values are consistent with a mass of 125.09 GeV [22].*

Decay mode	Branching ratio
$H \to b\bar{b}$	5.809×10^{-1}
$H \to WW^*$	2.152×10^{-1}
$H \to gg$	8.180×10^{-2}
$H \to \tau\tau$	6.256×10^{-2}
$H \to c\bar{c}$	2.884×10^{-2}
$H \to ZZ^*$	2.641×10^{-2}
$H \to \gamma\gamma$	2.270×10^{-3}
$H \to Z\gamma$	1.541×10^{-3}
$H \to \mu\mu$	2.171×10^{-4}

The Higgs boson can decay to fermion pairs for all kinematically allowed decay modes satisfying $m_H > 2m_f$. With a pole mass of 172.52 ± 0.29 GeV [27], the Higgs boson decay to a top quark pair is kinematically forbidden. Decays to all

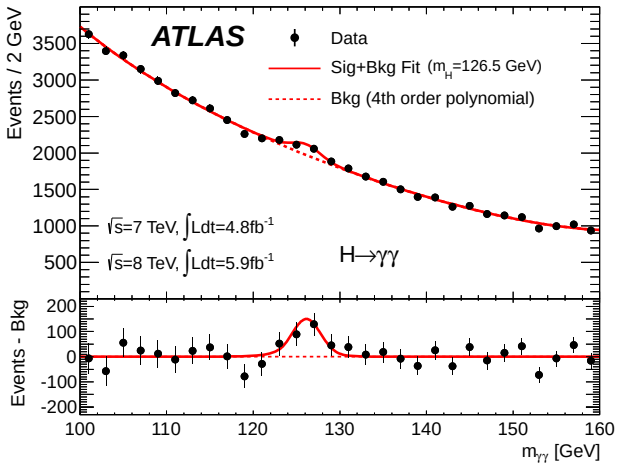

Figure 3.7 *Invariant mass distribution for the diphoton decay channel using ATLAS data. Figure from Ref. [1].*

other quark pairs are allowed with the Higgs boson decaying preferentially to bottom quarks. The Higgs boson also decays to lepton pairs ($\tau\tau$, $\mu\mu$ & ee).

Similarly, the Higgs boson can decay into bosons. For the decay to a pair of W or Z bosons to be kinematically viable, one of the gauge bosons must be produced off-shell (WW^*, ZZ^*). The Higgs boson can also decay to massless particles (γ & g) through loops of virtual heavy quarks or W bosons [28] as shown in Figure 3.6.

3.4 Higgs boson discovery

The discovery of the Higgs boson in 2012 by both ATLAS [1] and CMS [2] collaborations was a milestone in particle physics, recognised by the 2013 Nobel Prize in Physics to François Englert and Peter Higgs.

The datasets included pp collision data collected at the LHC during 2011 and 2012 at a centre-of-mass energy of $\sqrt{s} = 7$ and 8 TeV respectively. Both collaborations conducted individual searches with several final states: $\gamma\gamma$, ZZ^*, WW^*, $\tau\tau$ and $b\bar{b}$. The most significant evidence for the Higgs boson signal was achieved through a combination of the two most sensitive decay channels: $H \to \gamma\gamma$ and $H \to ZZ^* \to 4l$. The two channels are somewhat complementary to one another; the $H \to \gamma\gamma$ channel has a low signal-to-background ratio with a large number of events whilst the $H \to ZZ^* \to 4l$ channel has a high signal-to-background ratio with a small number of events.

In both channels, the mass of the Higgs boson candidate can be reconstructed from the invariant mass distribution of the decay products. Figure 3.7 presents the invariant mass distribution of the $H \to \gamma\gamma$ channel using ATLAS data. Above the large continuum background, a narrow Higgs boson signal was observed around a mass value of 125 GeV.

ATLAS and CMS collaborations combined their datasets to measure the mass of the Higgs boson [29]:

$$m_H = 125.09 \pm 0.21(\text{stat.}) \pm 0.11(\text{syst.}) \text{ GeV}. \tag{3.7}$$

The discovery of the Higgs boson in 2012 finally completed the SM of particle physics. Now 10 years on from this and the ATLAS Experiment has observed more than 30 times as many Higgs bosons. During Run 3 of the LHC, precision measurements of Higgs boson properties remains a key focus to further test the predictions of the SM and potentially probe new physics beyond the SM.

3.5 Parameterisation within the Kappa Framework

Couplings to the Higgs boson are 'pseudo-observables' in the SM — they cannot be measured directly. The production cross-sections and partial decay widths of the SM Higgs boson, however, can be parameterised in terms of coupling modifiers, κ, in the Kappa Framework [30]. The Higgs boson couplings to fermions and vector bosons can therefore be extracted by measuring the cross-section of Higgs processes. The analysis presented in this thesis applies the Kappa Framework to interpret the light and charm quark Yukawa couplings.

The purpose of the Kappa Framework is to establish whether properties of the Higgs boson are in fact consistent with, or exhibit deviations from, SM behaviour. In the parameterisation, it is assumed the observed signal originates from a single SM-like Higgs state with a mass near 125 GeV.

The signal cross-section of the Higgs boson in the diphoton channel can be parameterised as

$$(\sigma \cdot \mathcal{BR})(ii \to H \to ff) = \frac{\sigma_{ii}(\kappa) \cdot \Gamma_{ff}(\kappa)}{\Gamma_H(\kappa)}, \tag{3.8}$$

Table 3.4 *Parameterisation of the ggF and $q\bar{q} \to H$ production cross-sections, σ, partial decay widths, Γ_{ii}, and total decay width, Γ_H, of the Higgs boson in terms of the coupling modifiers, κ_i. Additional terms in red are included to account for the charm quark and light quark coupling modifiers where the coupling modifier is normalised to the bottom quark Yukawa coupling, $\overline{\kappa}_q = y_q/y_b^{SM}$. Table modified from Ref. [31].*

Production cross-section	Effective modifier	Resolved modifier
$\sigma(\text{ggF})$	κ_g^2	$1.040\,\kappa_t^2 + 0.002(\kappa_b^2 + \overline{\kappa}_c^2 + \overline{\kappa}_u^2 + \overline{\kappa}_d^2)$ $- 0.038\,(\kappa_t\kappa_b + \kappa_t\overline{\kappa}_c + \kappa_t\overline{\kappa}_u + \kappa_t\overline{\kappa}_d)$
$\sigma(b\bar{b} \to H)$	-	κ_b^2
$\sigma(c\bar{c} \to H)$	-	κ_c^2
$\sigma(u\bar{u} \to H)$	-	κ_u^2
$\sigma(d\bar{d} \to H)$	-	κ_d^2
Partial and total decay widths		
$\Gamma_{\gamma\gamma}$	κ_γ^2	$1.589\,\kappa_W^2 + 0.072\,\kappa_t^2 - 0.674\,\kappa_W\kappa_t + 0.009\,\kappa_W\kappa_\tau$ $+ 0.008\,(\kappa_W\kappa_b + \kappa_W\overline{\kappa}_c + \kappa_W\overline{\kappa}_u + \kappa_W\overline{\kappa}_d)$ $- 0.002\,(\kappa_t\kappa_b + \kappa_t\overline{\kappa}_c + \kappa_t\overline{\kappa}_u + \kappa_t\overline{\kappa}_d + \kappa_t\kappa_\tau)$
Γ_{gg}	κ_g^2	$1.111\,\kappa_t^2 + 0.012\,(\kappa_b^2 + \overline{\kappa}_c^2 + \overline{\kappa}_u^2 + \overline{\kappa}_d^2)$ $- 0.123\,(\kappa_t\kappa_b + \kappa_t\overline{\kappa}_c + \kappa_t\overline{\kappa}_u + \kappa_t\overline{\kappa}_d)$
Γ_H	κ_H^2	$0.581\,(\kappa_b^2 + \overline{\kappa}_c^2 + \overline{\kappa}_u^2 + \overline{\kappa}_d^2)$ $+ 0.215\,\kappa_W^2 + 0.063\,\kappa_\tau^2 + 0.026\,\kappa_Z^2$ $+ 0.0023\,\kappa_\gamma^2 + 0.0004\,\kappa_s^2 + 0.00022\,\kappa_\mu^2$ $+ 0.082\,(\Gamma_{gg}/\Gamma_{gg}^{\text{SM}})$

where σ_{ii} is the production cross-section through the initial state ii, Γ_{ff} is the partial decay width of the Higgs boson into the final state ff and Γ_H is the total width of the Higgs boson. Furthermore, $\sigma_{ii}(\kappa)$, $\Gamma_{ff}(\kappa)$ and $\Gamma_H(\kappa)$ can be parameterised in terms of the coupling modifiers where κ_i is defined such that $\sigma_{ii}(\kappa_i)$ or $\Gamma_{ii}(\kappa_i)$, associated with the SM particle i, scale with a factor of κ_i^2.

For any allowed $H \to f\bar{f}$ decays, the coupling modifiers can be expressed in terms of the Yukawa coupling as

$$\kappa_f = \frac{y_f}{y_f^{\mathrm{SM}}}, \tag{3.9}$$

where the SM Yukawa coupling, y_f^{SM}, is the best SM prediction in the limit of $\kappa_f \to 1$. Another useful parameterisation of the quark coupling modifiers is to normalise the light quark Yukawa couplings to the SM bottom quark Yukawa coupling,

$$\bar{\kappa}_q = \frac{y_q}{y_b^{\mathrm{SM}}}, \tag{3.10}$$

where the Yukawa couplings are evaluated at $\mu = m_H$ [32].

The dependence of the Higgs boson production cross-section on the top, bottom and charm quark coupling modifiers (κ_t, κ_b, κ_c) is expressed as follows:

$$\begin{aligned}\sigma_{pp\to H}(\kappa_t,\kappa_b,\kappa_c) &= \sigma_{\mathrm{ggF}}(\kappa_t,\kappa_b,\kappa_c) + \sigma_{\mathrm{ttH}}(\kappa_t) + \sigma_{b\bar{b}\to H}(\kappa_b) + \sigma_{c\bar{c}\to H}(\kappa_c) + \sigma_{\mathrm{other}} \\ &= \kappa_t^2(\sigma_{\mathrm{ggF}}^{tt} + \sigma_{\mathrm{ttH}}) + \kappa_b^2(\sigma_{\mathrm{ggF}}^{bb} + \sigma_{b\bar{b}\to H}) + \kappa_c^2(\sigma_{\mathrm{ggF}}^{cc} + \sigma_{c\bar{c}\to H}) \\ &+ \kappa_t\cdot\kappa_b\cdot\sigma_{\mathrm{ggF}}^{tb} + \kappa_t\cdot\kappa_c\cdot\sigma_{\mathrm{ggF}}^{tc} + \kappa_b\cdot\kappa_c\cdot\sigma_{\mathrm{ggF}}^{bc} + \sigma_{\mathrm{other}}. \end{aligned} \tag{3.11}$$

The full parameterisation of the ggF and $q\bar{q} \to H$ cross-sections is presented in Table 3.4, including additional terms for the light quark coupling modifiers. Furthermore, the $H \to \gamma\gamma$ and $H \to gg$ partial decay widths, as well as the total decay width of the Higgs boson, are sensitive to the quark Yukawa couplings. The parameterisation of these decay widths is also included in Table 3.4.

The calculations in Table 3.4 use the measured value of the Higgs mass of 125.09 GeV [29]. The production cross-sections and decay widths in the first column are by definition required to match the latest, highest precision theory calculations for the SM scenario ($\kappa = 1$). The functions in the third column of Table 3.4 are generally calculated at NLO in QCD; for $\kappa \neq 1$ higher-order accuracy is therefore lost and κ corresponds to an effective parameter [30].

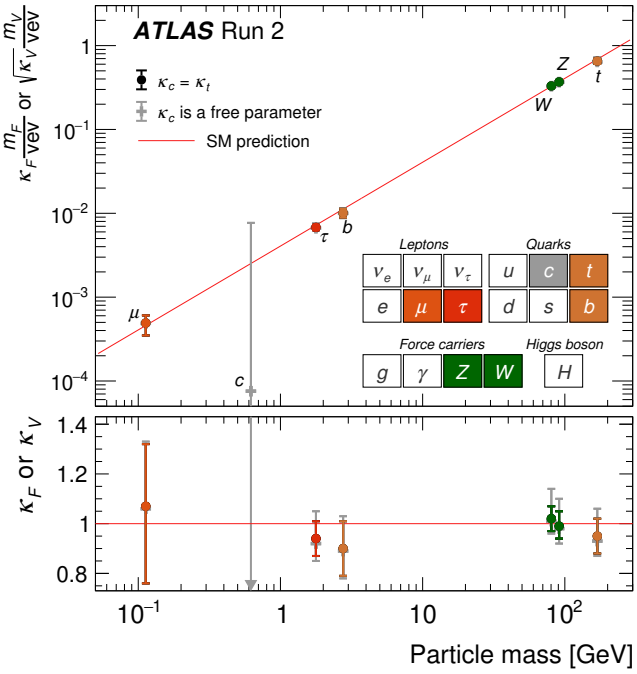

Figure 3.8 *Reduced Higgs boson coupling strength modifiers for fermions, $\kappa_F\, m_F/vev$ with $F = t, b, \tau, \mu$, and vector bosons, $\sqrt{\kappa_V}\, m_V/vev$. The lower panel shows values of the coupling strength modifiers κ_F and κ_V. The coloured markers represent the fit scenario where $\kappa_c = \kappa_t$ and the grey markers represent the fit scenario where κ_c is a free-floating parameter. Figure from Ref. [3].*

3.6 Measurements of the Yukawa coupling

The focus of this thesis is on constraining fermion Yukawa couplings. Direct measurements of the fermion Yukawa couplings can be achieved through a search for the $H \to f\bar{f}$ decay. The current measurements of the Higgs boson coupling strength modifiers performed using Run 2 data from the ATLAS Experiment are presented in Figure 3.8. More specifically, the top panel shows the reduced Higgs boson coupling strength modifiers for fermions F $= t, b, \tau, \mu$ in terms of fermion mass, m_F, and the vacuum expectation value (vev). The vector boson coupling strength modifiers are also plotted but are not discussed further in this thesis.

Experimentally, the interactions between the Higgs boson and third-generation fermions (t, b, τ) are well-measured with coupling strength values consistent with the SM as shown in Figure 3.8. The Yukawa coupling to first- and second-generation fermions, however, have yet to be measured — only upper limits on

interactions with second-generation muons [33, 34] and charm quarks [4, 5] have been set by the ATLAS and CMS collaborations. The data points in Figure 3.8 represent two fit scenarios for the charm quark coupling: $\kappa_c = \kappa_t$ (coloured markers) and κ_c left free to float (grey markers).

The main aim of this thesis is to constrain first-generation light quark Yukawa couplings using Run 3 data from the ATLAS Experiment. Moreover, the thesis also considers the charm quark Yukawa coupling.

3.6.1 Direct constraint on the charm Yukawa coupling

The method used to determine the constraints on the charm quark Yukawa coupling via the direct decay $H \to c\bar{c}$ is presented.

A search for $VH(H \to c\bar{c})$ with $V = W$ or Z was performed using $139\,\text{fb}^{-1}$ of 13 TeV pp collision data collected during Run 2 of the ATLAS Experiment [4]. Flavour-tagging algorithms are used to identify the jets originating from the hadronisation of quarks. In this analysis, a multivariate charm-tagging algorithm is used to identify the charm jets (c-jets). Additionally, a bottom jet (b-jet) identification algorithm is used to veto b-jets ensuring orthogonality to the $VH(H \to b\bar{b})$ analysis. The Higgs boson candidates are constructed from the two jets with the highest transverse momenta, p_T.

To search for the $H \to c\bar{c}$ signal, the dijet invariant mass, m_{cc}, is used to extract the signal yield. A fit to the m_{cc} distribution is performed to measure the signal strength, $\mu_{VH(c\bar{c})}$. To extract the coupling strength modifier, the signal strength can be interpreted within the Kappa Framework by parameterising the signal strength modifier in terms of κ_c:

$$\mu_{VH(c\bar{c})}(\kappa_c) = \frac{\kappa_c^2}{1 + \mathcal{BR}^{\text{SM}}_{H\to c\bar{c}}(\kappa_c^2 - 1)} \,, \tag{3.12}$$

where $\mathcal{BR}^{\text{SM}}_{H\to c\bar{c}}$ is the $H \to c\bar{c}$ branching fraction predicted in the SM. The observed and expected constraints on κ_c are presented in Table 3.5. Moreover, a combination with the ATLAS $VH(H \to b\bar{b})$ measurement to determine the ratio of the charm and bottom Yukawa couplings, $|\kappa_c/\kappa_b|$, is presented.

The same search was performed by the CMS collaboration [5] with a similar dataset and analysis strategy. The observed 95% confidence level interval on κ_c is

Table 3.5 *Direct constraints on the charm quark Yukawa coupling from the ATLAS Run 2 $H \to c\bar{c}$ analysis published in 2022 in Ref. [4] and a re-analysis of the dataset during 2024 presented in Ref. [35]. The observed (expected) constraints on κ_c and the ratio of $|\kappa_c/\kappa_b|$ at 95% confidence level are presented.*

κ	2022 analysis in Ref. [4] Observed (exp) 95% CL	2024 analysis in Ref. [35] Observed (exp) 95% CL
$\lvert\kappa_c\rvert <$	8.5 (12.4)	4.2 (4.1)
$\lvert\kappa_c/\kappa_b\rvert <$	4.5 (5.1)	3.6 (3.5)

$1.1 < |\kappa_c| < 5.5$ — the most stringent constraint on κ_c at the time of publication.

A re-analysis of the legacy search for $VH(H \to c\bar{c})$ with the ATLAS Run 2 data is presented in Ref. [35]. A multivariate approach was introduced to maximise the sensitivity of the analysis in the form of a boosted decision tree signal-background classifier. The new observed and expected constraints on κ_c and $|\kappa_c/\kappa_b|$ at 95% confidence level are presented in Table 3.5, improving on the previous result by a factor of 2. The observed ratio of $|\kappa_c/\kappa_b|$ confirms the Higgs boson coupling to charm quarks is weaker than to bottom quarks.

Searches for the direct decay of $H \to c\bar{c}$ are limited by statistical uncertainties due to a small branching fraction of 2.88% [22]. The dominating uncertainty, however, originates from the jet tagging efficiency required to identify the c-jets.

3.6.2 Constraints on the light quark Yukawa couplings

The large QCD background at the LHC inhibits the direct measurement of the light (up, down and strange) quark Yukawa couplings through $H \to q\bar{q}$. Rare, exclusive decays of the Higgs boson to a light vector meson M ($H \to M\gamma$) have been proposed to probe the light quark Yukawa couplings [36, 37].

Figure 3.9 shows the *direct* and *indirect* Feynman diagrams for $H \to M\gamma$. The direct decay is sensitive to the Yukawa couplings through the $H \to q\bar{q}$ coupling. The indirect decay is mediated by the $H \to \gamma\gamma$ coupling. Due to the smallness of the light quark Yukawa couplings, the indirect decay dominates despite being loop-induced. The Higgs boson couplings to light quarks can therefore be probed by searching for modifications in the branching ratio due to the direct decay mode — this interpretation, however, requires precise knowledge of the indirect decay.

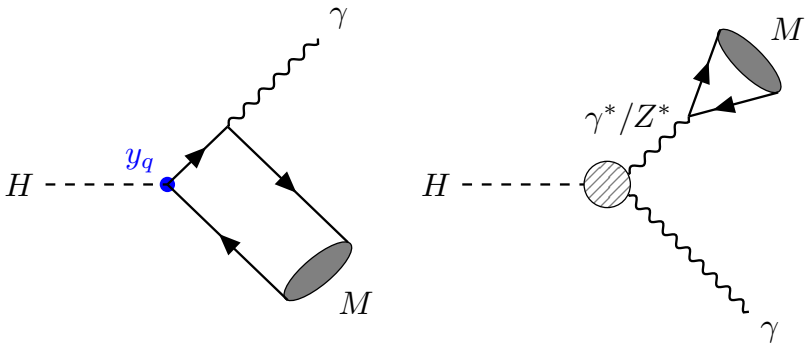

Figure 3.9 *Direct (left) and indirect (right) Feynman diagrams for the Higgs boson decay to meson M and a photon, $H \to M\gamma$. For the indirect decay, the circle represents a loop of virtual heavy quarks or W bosons.*

Both ATLAS [38] and CMS [39] collaborations have performed searches for different $H \to M\gamma$ decay modes using Run 2 data. To probe the strange quark Yukawa coupling, $H \to \phi\gamma$ is considered whilst $H \to \rho\gamma$ probes the Higgs coupling to up and down quarks. The decays $\phi \to K^+K^-$ and $\rho \to \pi^+\pi^-$ are used to reconstruct the ϕ meson and ρ meson respectively. The current constraints on the light quark Yukawa couplings at 95% confidence level are presented in Table 3.6.

Table 3.6 *Current constraints on the light (u, d, s) quark Yukawa coupling modifiers, $\bar{\kappa}_q$, measuring exclusive decays to light mesons, $H \to M\gamma$. Table modified from Ref. [6].*

Mode	$\mathcal{BR}_{M\gamma} <$		Observed 95% CL
$H \to \phi\gamma$	4.8×10^{-4}	$\overline{\kappa}_s$	$[-130,\ 150]$
$H \to \rho\gamma$	8.8×10^{-4}	$2\overline{\kappa}_u + \overline{\kappa}_d$	$[-243,\ 327]$

Most recently, CMS [40] collaboration analysed the Yukawa couplings between light quarks and the Higgs boson by examining changes in the Higgs boson production rate. The analysis was performed searching for γH production in the four lepton final state using the full Run 2 dataset. The constraints on the light quark Yukawa coupling modifiers are presented in Table 3.7.

Table 3.7 *Constraints on the light quark coupling modifiers, $\bar{\kappa}_q$, measuring γH production. Table adapted from Ref. [40].*

Parameter	Observed 95% CL	Expected 95% CL
$\bar{\kappa}_u$	$[-1.06, 1.05]$	$[-1.13, 1.13]$
$\bar{\kappa}_d$	$[-0.97, 0.97]$	$[-0.98, 0.97]$
$\bar{\kappa}_s$	$[-0.89, 0.85]$	$[-0.85, 0.81]$

3.7 Fiducial cross-section analysis

In the context of a fiducial cross-section analysis, the Yukawa couplings can be probed indirectly by measuring the transverse momentum distribution of the Higgs boson, $p_{\mathrm{T},H}$.

3.7.1 Fiducal volume and cross-sections

A fiducial definition of a measurement is required to extract detector-independent observables. This involves measuring an observable as it would be by a perfect version of the detector, free from any inefficiencies or biases introduced by the reconstruction process. It is important, however, to not idealise the measurement too far. For example, to avoid extrapolating the perfect detector to have perfect coverage, the finite acceptance of the detector must be taken into account. A closed region of phase-space that overlaps significantly with the performant regions of the detector is therefore defined — known as the *fiducial volume* within which the performance of physics objects is considered to be perfect. The fiducial volume defines a detector-independent set of measurements. Any extrapolation outside the fiducial volume, in a region that cannot be directly observed, is highly model-dependent or uncertain. Focusing solely on what the experiment can actually observe, the motivation behind fiducial measurements is to make the measurement as precise and model-independent as possible [20].

For the differential fiducial cross-section, the independent variable X in the differential cross-section $d\sigma/dX$ is typically based on final-state observable properties, such as the transverse momentum of the Higgs boson $d\sigma/dp_{\mathrm{T,H}}$.

3.7.2 Diphoton channel

The exact definition of the fiducial volume is specific to the analysis. The fiducial cross-section analysis relevant to this thesis is performed in the $H \to \gamma\gamma$ decay channel. The fiducial volume is defined by the kinematic properties of the two photons introduced in Section 8.2.3.

Motivated by a clean experimental signature, the $H \to \gamma\gamma$ decay channel is chosen despite a small branching ratio of 0.23% in the SM. The ATLAS event display

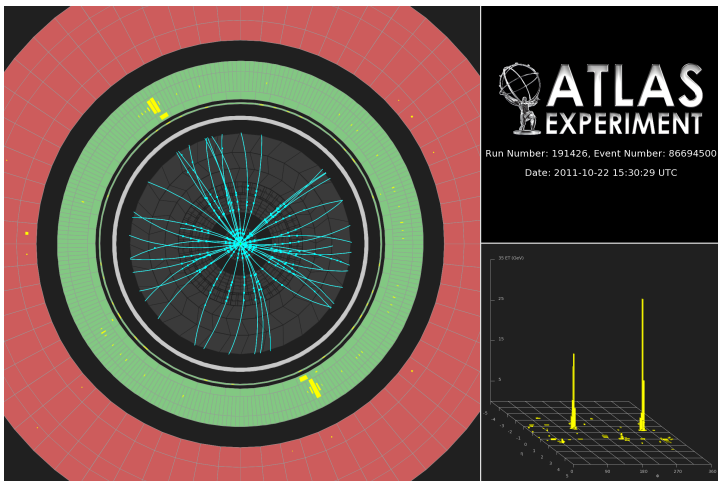

Figure 3.10 *ATLAS event display of a candidate diphoton event from 2011. The two high-energy photons are identified by the two large energy deposits (yellow) in the electromagnetic calorimeter (green ring). Figure from Ref. [41].*

in Figure 3.10 illustrates a candidate $H \to \gamma\gamma$ event. The distinct final-state topology of the diphoton channel is indicated by two large energy deposits in the electromagnetic calorimeter used to identify the two high-energy photons.

To observe the Higgs boson at the LHC, it is essential to distinguish the Higgs final states from the large QCD background. Background processes in the diphoton channel are categorised into two main types: resonant processes that produce a Higgs boson and non-resonant processes that do not produce a Higgs boson. The non-resonant background is dominated by SM diphoton production. Additional contributions arise from events where one (γj) or two (jj) jets are misidentified as photons. Both resonant and non-resonant background processes contribute to the diphoton invariant mass spectrum.

3.7.3 Indirect measurements of the Yukawa couplings

In the context of the $H \to \gamma\gamma$ fiducial cross-section analysis, a measurement of the Higgs boson production cross-section can be used as an indirect probe to the Yukawa couplings. As demonstrated in Section 3.5 (see Table 3.4), the Higgs boson production cross-section is sensitive to the Yukawa couplings through:

1. loop induced gluon-gluon fusion (ggF); and
2. quark-initiated Higgs production $(q\bar{q} \to H)$.

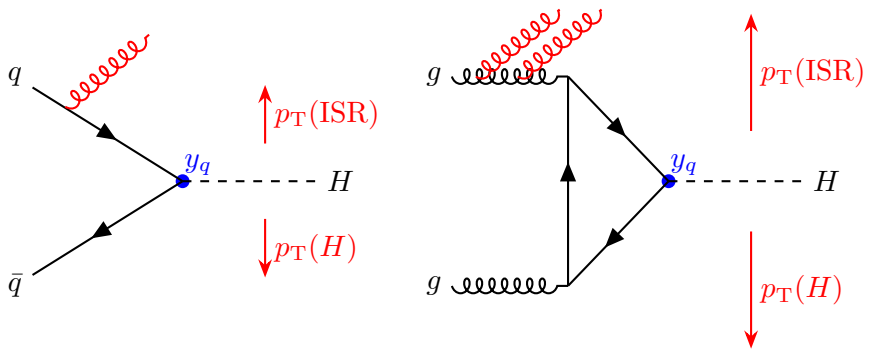

Figure 3.11 *Feynman diagrams illustrating the effect of initial state radiation (ISR) on the $p_{T,H}$ distribution for (left) $q\bar{q} \to H$ and (right) ggF production. Colour charge dictates the probability of soft gluon emissions. Gluons have a higher colour charge and so there is a higher probability of gluon emissions for ggF.*

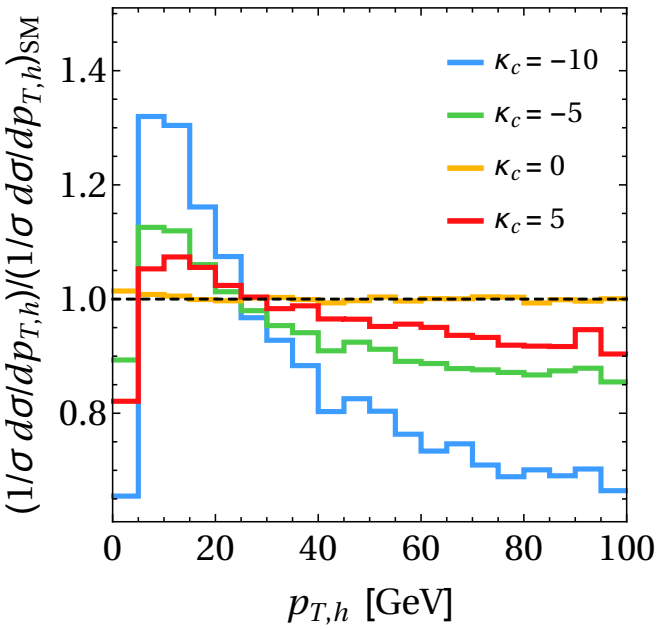

Figure 3.12 *Template of the normalised Higgs boson transverse momentum, $p_{T,H}$, spectrum for different values of κ_c divided by the SM prediction. All other Yukawa couplings are set to their SM values. The templates consider the inclusive Higgs production at 8 TeV. Figure from Ref. [42].*

The indirect senstivity to the Yukawa couplings is observed through both the *shape* and *normalisation* of the diphoton transverse momentum distribution, $p_{\mathrm{T},\gamma\gamma}$. This method has the advantage of not being limited by the tagging efficiency of jets originating from the charm quark in $H \to c\bar{c}$ decays.

Shape-only effects

Figure 3.11 illustrates the effect of initial state radiation (or soft gluon emissions) on the $p_{\mathrm{T},H}$ (or $p_{\mathrm{T},\gamma\gamma}$) distribution. The probability of a soft gluon emission is dictated by the colour charge of the initial state partons; colour factor gives rise to the relative strength of the coupling between the parton and the radiating gluon. Since gluons have a higher colour charge than quarks, there is a higher probability of gluon emissions for ggF. More soft gluon emissions results in a broader $p_{\mathrm{T},H}$ distribution for ggF. Conversely, $q\bar{q} \to H$ has a narrower $p_{\mathrm{T},H}$ distribution. The ggF and $q\bar{q} \to H$ production modes can therefore be experimentally distinguished through the $p_{\mathrm{T},H}$ distribution. Figure 3.12 illustrates the shape-only effects observed through the normalised $p_{\mathrm{T},H}$ spectrum for varying values of κ_c [32].

Normalisation effects: cross-section and branching ratio

The normalisation of the $p_{\mathrm{T},\gamma\gamma}$ distribution is sensitive to the Yukawa couplings through the parameterisation of the cross-section and branching ratio in the Kappa Framework, as described in Section 3.5. The expected number of $H \to \gamma\gamma$ events is determined by

$$\mathcal{N} = \sigma(\kappa_q) \cdot \mathcal{L} \cdot \mathcal{B}_{\gamma\gamma}(\kappa_q) \cdot \epsilon, \tag{3.13}$$

where σ is the Higgs production cross-section, $\mathcal{L}$ is the integrated luminosity, $\mathcal{B}_{\gamma\gamma}$ is the $H \to \gamma\gamma$ branching ratio and ϵ is the efficiency of the diphoton selection. To determine the constraints on κ_q, using both normalisation and shape effects of the $p_{\mathrm{T},\gamma\gamma}$ distribution, all other coupling modifiers are set to their SM values.

3.7.4 Indirect constraint on the charm Yukawa coupling

For the ATLAS Run 2 $H \to \gamma\gamma$ fiducial cross-section measurement [7], the method described above was used to extract constraints on the bottom and charm quark

Table 3.8 *Observed and expected constraints at 95% confidence level on the bottom and charm Yukawa coupling modifiers, κ_b and κ_c respectively. Table adapted from Ref. [7].*

κ	Observed 95% CL	Expected 95% CL
κ_c	$[-2.5,\ 2.3]$	$[-3.0,\ 3.1]$
κ_b	$[-1.1, -0.8] \cup [0.8,\ 1.1]$	$[-1.2, -0.9] \cup [0.8,\ 1.2]$

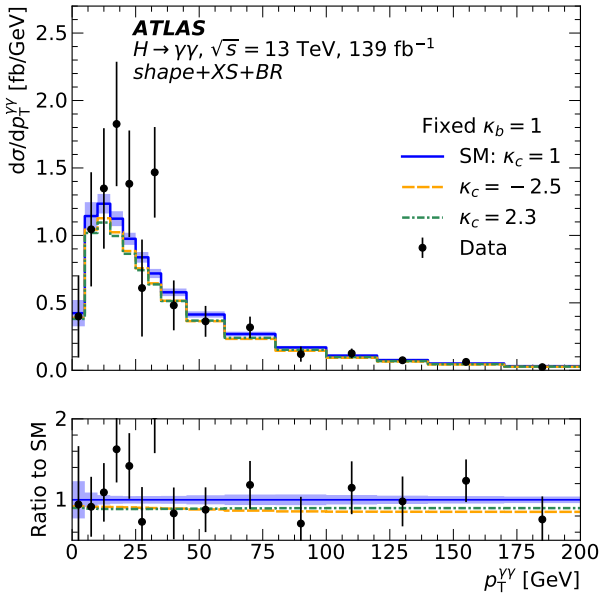

(a) $p_{T,\gamma\gamma}$ *template*

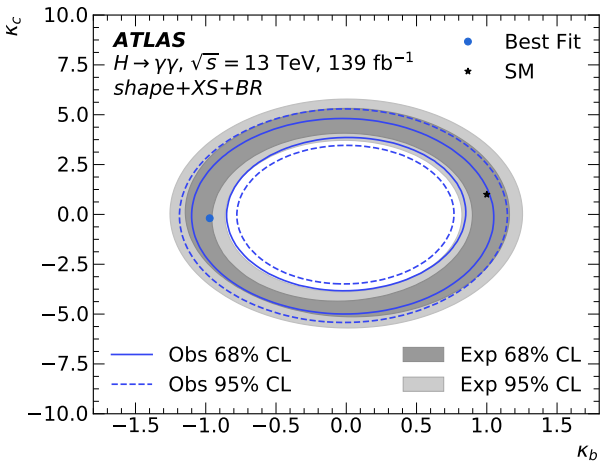

(b) *2D limits of* κ_b *and* κ_c

Figure 3.13 *(a) Observed fiducial differential cross-section times branching ratio for the diphoton transverse momentum distribution, $p_{T,\gamma\gamma}$, for different values of κ_c corresponding to the 95% CL. (b) Two-dimensional limits on κ_b and κ_c. Limits are presented at both 95% and 68% confidence levels. The fitting strategy considers both shape and normalisation effects. Figures from Ref. [7].*

Yukawa couplings. Cross-section measurements for $H \to \gamma\gamma$ production were performed using $139\,\text{fb}^{-1}$ of $13\,\text{TeV}$ pp collision data. Table 3.8 summarises the observed and expected constraints on κ_b and κ_c respectively at 95% confidence level. The $p_{\text{T},\gamma\gamma}$ templates for different values of κ_c corresponding to the 95% confidence level are presented in Figure 3.13a. Furthermore, the two-dimensional limits on κ_b and κ_c are presented in Figure 3.13b.

The work in this thesis builds upon the Yukawa interpretation of the $H \to \gamma\gamma$ cross-section measurement presented in Ref. [7]. The techniques used in this publication are discussed in detail in Chapter 8.

Chapter 4

The Large Hadron Collider and the ATLAS Experiment

The Large Hadron Collider (LHC) is the world's most powerful particle accelerator and the home of the ATLAS Experiment. In this chapter, I start by introducing the Large Hadron Collider (LHC) and its accelerator complex to provide context for how proton beams are accelerated and collided in the LHC ring. The ATLAS detector is then described in detail, including the different detector subsystems and the technologies used to build the detector. A particular focus is given to the Electromagnetic Calorimeter (ECal) — the main sub-detector used to measure photons in the $H \to \gamma\gamma$ analysis.

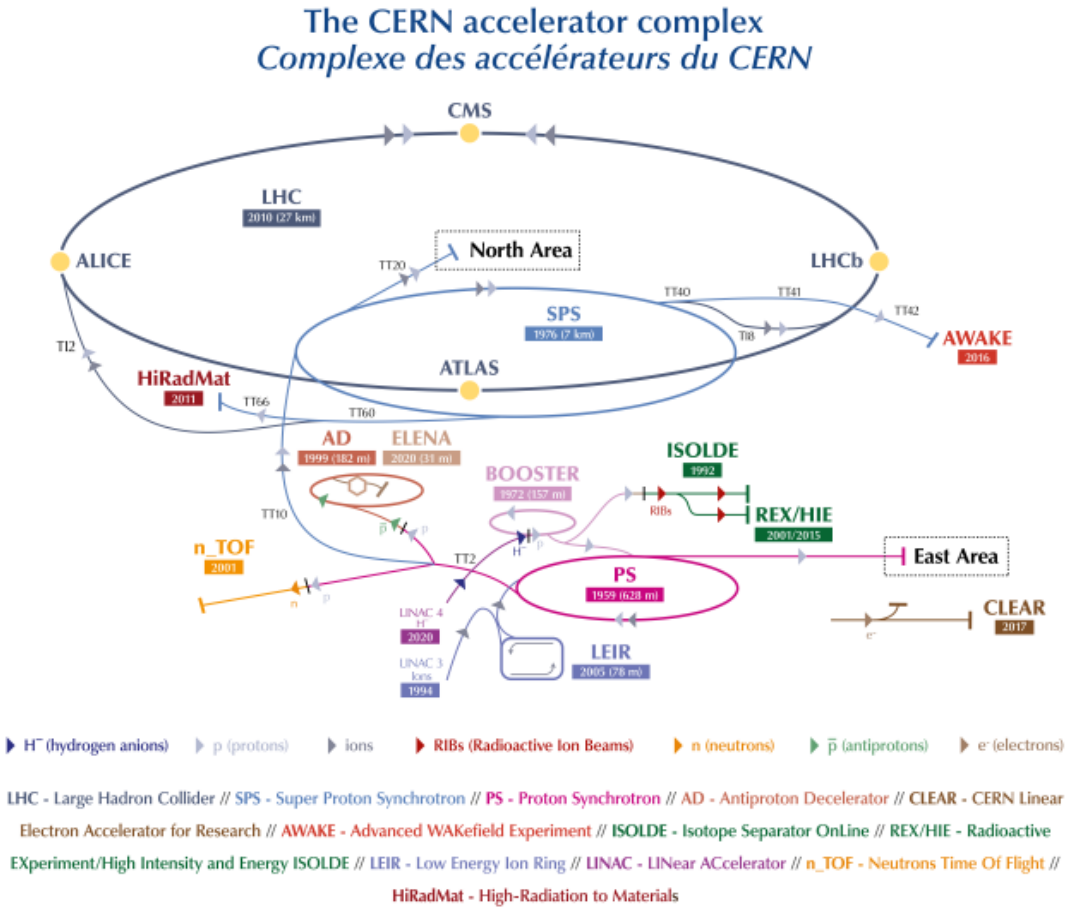

Figure 4.1 *The accelerator complex at the CERN. Figure from Ref. [43].*

4.1 The Large Hadron Collider

Proton-proton (pp) collision data, collected during Run 3 of the Large Hadron Collider (LHC) [44] between 2022 and 2023, is used in this thesis. An overview of the process by which pp collisions occur at the LHC to produce the analysed data is provided in this section.

The LHC is the largest particle accelerator in the world situated 100 m underground at the CERN laboratory. Located in the tunnel of its predecessor, the Large Electron-Positron Collider (LEP), the LHC spans a circumference of 27 km. The LHC is a two-ring superconducting hadron collider designed to collide protons at an unparalleled luminosity and centre-of-mass energy [45]. Protons are supplied to the LHC through the accelerator complex at CERN illustrated in Figure 4.1, which is designed to accelerate protons to increasingly higher energies.

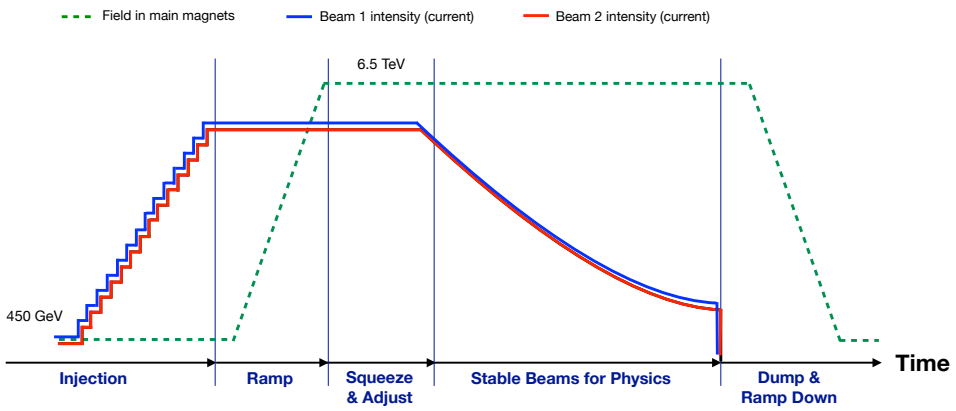

Figure 4.2 *The stages of the LHC beam cycle. The beams are injected into the two rings of the LHC. During ramp the beams are accelerated to the collision energy (*6.8 TeV *for Run 3). The beams are prepared for collisions during squeeze and adjust. During stable beams collisions take place at the interaction points. Finally, the beams are extracted from the ring during dump and ramp down. Figure from Ref. [46].*

There are many stages to proton acceleration, starting with a small container of hydrogen gas. An electric field is used to strip the electrons from the hydrogen atoms to produce negative hydrogen ions (or protons). The resulting protons are sent to the Linear accelerator 4 (Linac4), replacing Linear accelerator 2 (Linac2) for Run 3. Linac4 accelerates protons to an energy of 160 MeV before being injected into a series of smaller circular accelerators: the Proton Synchrotron Booster (PSB); the Proton Synchrotron (PS); and the Super Proton Synchrotron (SPS). Protons are accelerated up to 450 GeV before finally being injected into the LHC through two beam pipes — one circulating clockwise and the other anticlockwise. The final stage of acceleration in the LHC ring, known as ramp-up, takes approximately 20 minutes to accelerate the protons to an energy of 6.8 TeV for Run 3. The stages of the LHC beam cycle are shown in Figure 4.2.

Accelerators use oscillating electric fields to accelerate charged particles. More specifically, radiofrequency cavities (metallic chambers spaced at intervals along the accelerator) are used to generate electromagnetic fields that oscillate at specific frequencies. As the particle beam passes through the cavities, the protons are accelerated along the beam pipe. For circular accelerators, dipole magnets are used to bend the path of the beam around the ring. Quadrupole magnets are used to focus the beam, keeping the protons close together.

The two beams are brought into collision at four interaction points where four detectors are located: A Toriodal LHC Apparatus (ATLAS) [47], Compact

Muon Solenoid (CMS) [48], LHC beauty (LHCb) [49], and A Large Ion Collider Experiment (ALICE) [50]. The LHC primarily runs *pp* collision. It can also accelerate beams of heavy ions for lead-lead (Pb-Pb) and proton-lead (*p*-Pb) collisions. Since individual protons are too small to collide, the proton beams are structured into bunches. Each beam can contain up to 2808 bunches with each bunch containing approximately 1.15×10^{11} protons. A bunch crossing refers to the moment when two bunches collide. The LHC operates at a bunch crossing rate of 40 MHz corresponding to a bunch spacing of 25 ns [51]. During the data taking periods used in this thesis, on average around 45 *pp* collisions took place in a single bunch crossing — a measure commonly used to quantify *pile-up* which is introduced in Section 4.1.1.

Run 3 of the LHC started in 2022 and is expected to continue until 2026. Over the lifetime of the LHC, the centre-of-mass energy, $\sqrt{s}$, at the interaction point has increased with each run. Run 1 (2009–2013) operated at $\sqrt{s} = 7 - 8\,\text{TeV}$, increasing to $\sqrt{s} = 13\,\text{TeV}$ for Run 2 (2015–2018). For Run 3, the centre-of-mass energy has increased to $\sqrt{s} = 13.6\,\text{TeV}$. Ultimately, the LHC is designed to reach a proton beam energy of 7 TeV resulting in a centre-of-mass energy of $\sqrt{s} = 14\,\text{TeV}$. This goal is a key objective of the High-Luminosity LHC (HL-LHC) [52] which is set to succeed Run 3.

4.1.1 Events, luminosity and pile-up

At the point of collision, the interaction of two protons is referred to as an *event*. The event rate of a physical process produced in collisions is given by

$$\frac{dN}{dt} = \sigma \cdot \mathcal{L}, \tag{4.1}$$

where σ is the cross-section and $\mathcal{L}$ is the instantaneous luminosity. The instantaneous luminosity (units: $\text{cm}^{-2}\text{s}^{-1}$) measures the number of particles per unit area per unit time.

Luminosity is a key concept at collider experiments that depends on parameters of the colliding proton beams. Assuming Gaussian beam distribution, the instantaneous luminosity is given by

$$\mathcal{L} = \frac{N_b N_p^2 f_{\text{rev}} F}{4\pi\sigma_x\sigma_y}. \tag{4.2}$$

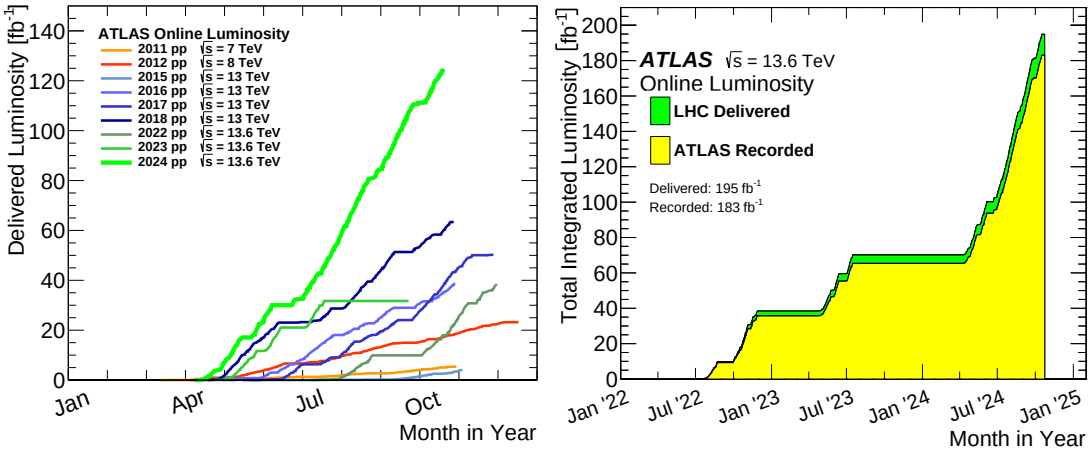

(a) *Luminosity for each year* **(b)** *Luminosity for Run 3*

Figure 4.3 *(a) The LHC delivered luminosity to the ATLAS Experiment during pp collisions for each year of running. (b) The cumulative integrated luminosity delivered by the LHC (green) and recorded by the ATLAS Experiment (yellow) during pp collision for Run 3 (2022–2024). Figures from Ref. [53].*

The beam parameters are defined as follows: N_b is the number of bunches; N_p is the number of protons per bunch; $f_{\text{rev}} = 11.25\,\text{kHz}$ is the revolution frequency of the beams; F is the geometric reduction factor due to the angle of beam crossing at the interaction points ($F = 1$ for head-on collisions); and σ_x and σ_y are the horizontal and vertical beam sizes respectively [54]. At the LHC, the design value for the instantaneous luminosity is $\mathcal{L} = 10^{34}\,\text{cm}^{-2}\,\text{s}^{-1}$ for pp collisions. The integrated luminosity,

$$\mathcal{L}_{\text{int}} = \int_0^T \mathcal{L}(t)dt, \tag{4.3}$$

is a measure of how many collisions have occurred over a period of time T or, more simply, a measure of the total data collected.

Run 3 of the LHC is expected to deliver an integrated luminosity of $250\,\text{fb}^{-1}$ of pp collision data between 2022 and 2026 [55]. The integrated luminosity delivered to the ATLAS Experiment for each year of pp collisions is shown in Figure 4.3a. Focusing on the 2022 and 2023 data used in this thesis, Figure 4.3a highlights the complications that resulted in a lower integrated luminosity than expected. An incident at interaction point 8 along the LHC ring in 2023 resulted in the end of pp data taking in July instead of October. The integrated luminosity recorded and declared *good for physics* in 2022 and 2023 was $31.4\,\text{fb}^{-1}$ and $27.2\,\text{fb}^{-1}$ respectively. By contrast, 2024 has been the highest delivering year so far with $117.6\,\text{fb}^{-1}$ recorded by the end of October 2024. Figure 4.3b illustrates

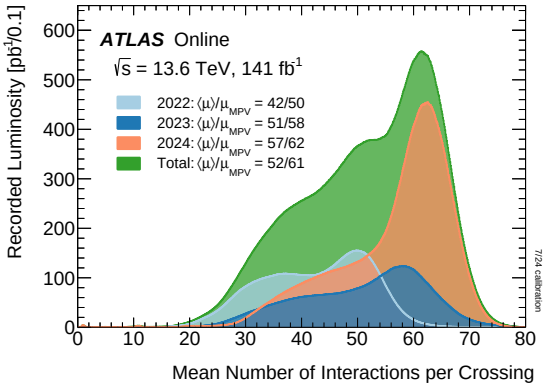

Figure 4.4 *Luminosity-weighted distribution of the average number of interactions per bunch crossing (pile-up) for each year of pp collision data during Run 3 (2022–2024) to date. Figure from Ref. [53].*

the integrated luminosity delivered to the ATLAS Experiment during Run 3 (2022–2024) to date, already exceeding the $139\,\text{fb}^{-1}$ delivered during Run 2. Given the time constraints of this thesis, the data collected in 2024 was not ready for analysis and so is not included in this thesis.

Another important parameter to consider at the LHC is *pile-up*, referred to as the presence of other pp collisions within the event of interest. In the context of this thesis, the event of interest is $H \to \gamma\gamma$. A simple way to quantify pile-up is to quote the average number of interactions per bunch crossing. As the integrated luminosity increases, both the number of events of interest and pile-up increase. The average number of interactions per bunch crossing is shown in Figure 4.4 for each year of pp collision data during Run 3.

4.2 The ATLAS detector

ATLAS [55–57] is a general-purpose detector designed to exploit the full discovery potential of the LHC. The detector has close to full coverage of the solid angle and a forward-backward symmetry with respect to the interaction point. A combination of tracking, calorimetry and spectrometry techniques are used to form the six detector subsytems that make up the ATLAS detector: Pixel Detector, Semiconductor Tracker (SCT), Transition Radiation Tracker (TRT), Electromagnetic Calorimeter (ECal), Hadronic Calorimeter (HCal) and Muon Spectrometer (MS). This combination of different detecting subsystems is used to reconstruct the trajectories of all particles that travel through the detector.

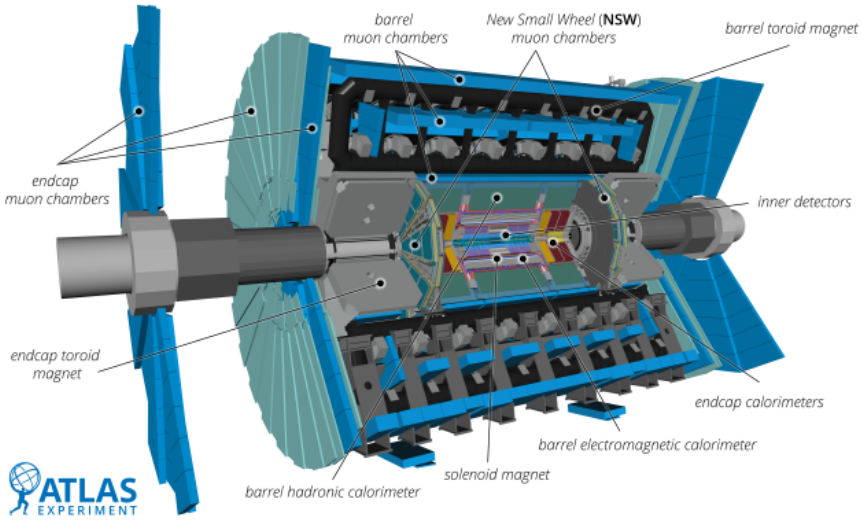

Figure 4.5 *A cut-away view of the ATLAS detector showing all subdetector systems. Figure from Ref. [55].*

The ATLAS detector is 25 m tall and 44 m long with a total weight of 7000 t, similar to the weight of the Eiffel Tower. A diagram of the ATLAS detector with the labelled subsystems is shown Figure 4.5. The Pixel Detector, SCT and TRT subsystems form the Inner Detector (ID). The ID is a tracking system designed to allow charged particles to pass through whilst accurately measuring their position. The ECal works by absorbing and measuring the energy of electrons and photons as they interact with matter. The HCal samples the energy of hadrons as they interact with atomic nuclei. Most particle trajectories are stopped in the calorimeter system, except for muons and neutrinos. The MS identifies and measures the momenta of the muons. Furthermore, the magnetic system is designed to bend the tracks of charged particles for momentum measurements. The magnetic system consists of a thin, superconducting solenoid surrounding the ID cavity and three large, superconducting toroids surrounding the calorimeter system [58].

In the following sections, the ATLAS detector is discussed with an emphasis on the subsystems most relevant to this thesis. Given the focus on ggF and $q\bar{q} \to H$ production in the $H \to \gamma\gamma$ decay channel, the most crucial component of the ATLAS detector is the ECal which is used to identify and measure the energy of photons.

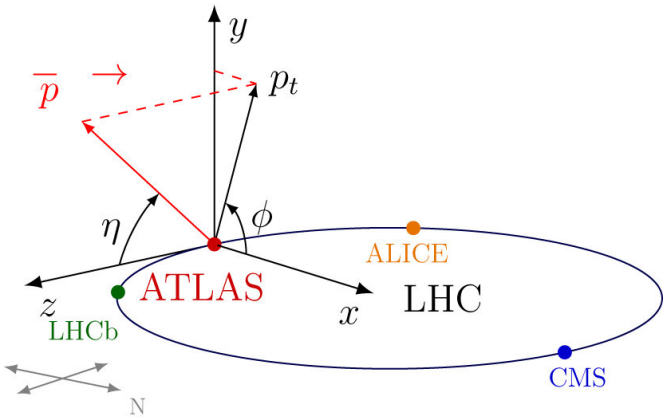

Figure 4.6 *The ATLAS coordinate system illustrated in the context of the LHC ring. Figure from Ref. [59].*

4.3 Coordinate system

The ATLAS Experiment uses a right-handed coordinate system with the origin at the centre of the detector, known as the nominal interaction point. In Cartesian coordinates, (x, y, z) are defined as follows: the z-axis coincides with the beam pipe; the x-axis points towards the centre of the LHC ring; and the y-axis points towards the sky. A diagram of the coordinate system with respect to the LHC ring is shown in Figure 4.6. In spherical coordinates, θ and ϕ are defined as follows: θ is the polar angle in the $r-z$ plane between the z-axis and momentum vector $\vec{p}$; and ϕ is the azimuthal angle in the $x-y$ plane between the x-axis and the projection of momentum in the transverse plane, p_T.

At a hadron collider, the momentum of the incoming protons is fixed to the beam energy. The momentum of the colliding partons, however, is unknown and so the boost of the initial colliding system is also unknown. It is therefore convenient to consider variables that are invariant to boosts along the z-direction. This is true for the transverse momentum,

$$p_T = \sqrt{p_x^2 + p_y^2}, \tag{4.4}$$

which must be conserved and equal to zero. Since the z-component of momentum, p_z, is not Lorentz invariant, it is convenient to replace it with another variable, *rapidity*, that depends on p_z and the energy, E, of the particle. Rapidity, y, is defined as

$$y = \frac{1}{2} \ln \left(\frac{E + p_z}{E - p_z} \right), \tag{4.5}$$

where the difference in rapidity, Δy, is Lorentz invariant for boosts in the z-axis. Rapidity is essentially a measure of how forwards (closer to the positive z-axis) or backwards a particle is with respect to the beam line. At high-energy colliders, it is common to consider *pseudorapidity* instead as

$$\eta = -\ln \tan\left(\frac{\theta}{2}\right), \tag{4.6}$$

which depends on the polar angle. The ATLAS detector, for example, has a maximum acceptance of $|\eta| < 4.9$.

4.4 Magnet system

The ATLAS magnet system [60] is designed to bend the trajectories of charged particles to make momentum measurements. The radius of curvature, r, is proportional to the transverse momentum of the particle, given by

$$r = \frac{p_T}{qB}, \tag{4.7}$$

where q is the charge of the particle and B is the constant magnetic field strength. By measuring the curvature of a particle's trajectory, both the charge and momentum of the particle can be determined.

ATLAS features two types of superconducting magnet systems: a solenoid magnet and three toroid magnets. The central solenoid [61], aligned with the beam pipe, produces a 2 T axial magnetic field for the ID tracking system. There are three toroid magnets in the ATLAS detector used to measure muon momentum: one barrel toroid [62] surrounding the centre of the experiment generating a magnetic field of 0.5 T; and two endcap toroids [63] at either end of the detector generating magnetic fields of 0.5 T.

4.5 Tracking: the Inner Detector

The Inner Detector (ID) [65, 66] is the first detector subsystem to detect the decay products of collisions. Combining high-resolution detectors with continuous tracking elements, the ID is used to measure the direction, momentum and charge of electrically-charged particles produced in pp collisions.

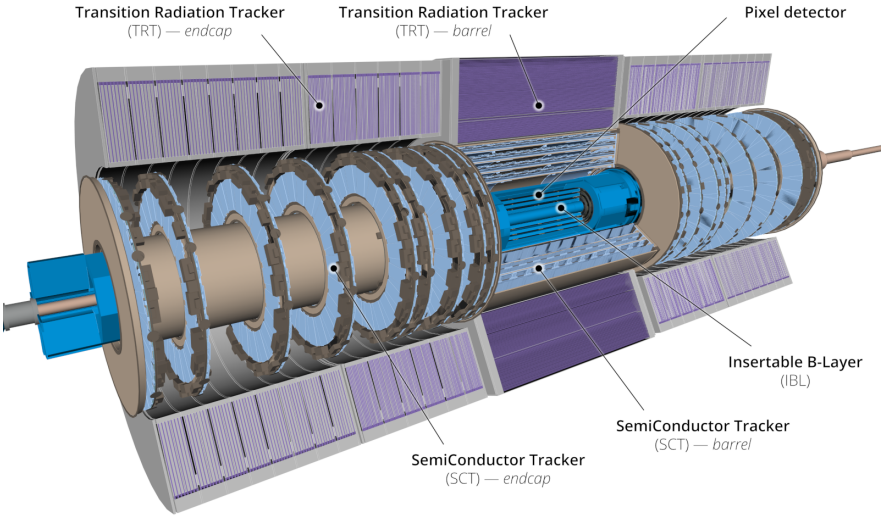

Figure 4.7 *Cross-section view of the ATLAS ID. The ID is divided into three subsystems: Pixel Detector, SCT and TRT. Each subsystem is divided into barrel and end-cap regions. The IBL is the innermost layer of the Pixel Detector added during the first long shutdown of the LHC between Run 1 and Run 2. Figure from Ref. [55].*

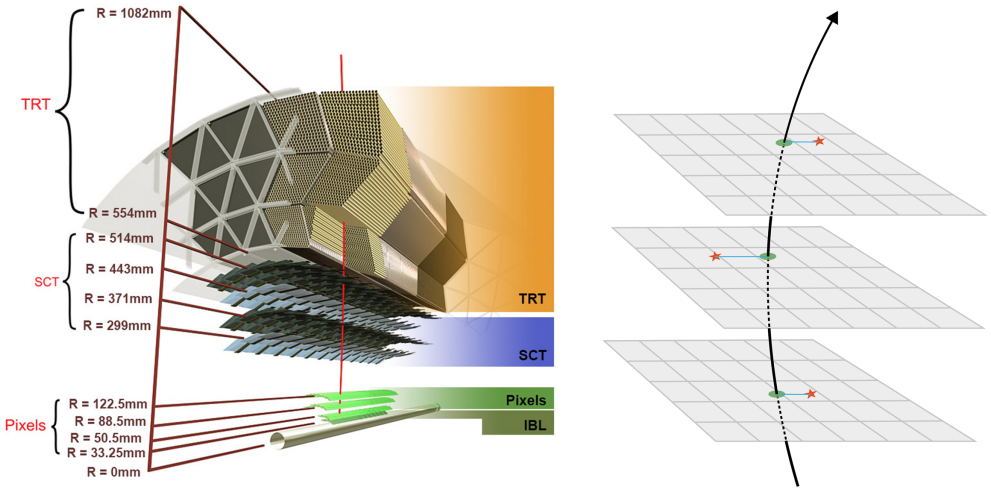

Figure 4.8 *(Left) Three-dimensional visualisation of the ID barrel region and its four components: the IBL, Pixel Detector, SCT and TRT. (Right) schematic representation of a charged particle crossing the ID subsystems. Red stars indicate detector measurements (hit) and the fitted track is in black. Green dots indicate where the track intersects with the surface whilst the blue lines represent the track-to-hit residuals. Figure from Ref. [64].*

Figure 4.7 shows a cross-section view of the ID system which is divided into three subsystems: Pixel Detector, Semiconductor Tracker (SCT), and Transition Radiation Tracker (TRT). By construction, the ID is split into three units: a barrel region ($|\eta| < 1$) and two identical end-cap regions. The total system provides full coverage over $|\eta| < 2.5$. The Pixel Detector and SCT form the precision tracking detectors in the ID. At larger radii, the TRT offers a high number of tracking points allowing for continuous tracking.

Pixel Detector

As the first detection point, the Pixel Detector [67, 68] is designed to provide very high granularity and precision measurements close to the interaction point. Silicon pixel technology enables measurements to be made with a resolution of the order of tens of microns. The nominal pixel size is 50 µm × 400 µm in the $(r\phi, z)$ plane for the barrel region and the $(r\phi, r)$ plane for the end-cap regions. Charged particles traversing through silicon will release electron-hole pairs through ionisation. A voltage is applied across the silicon sensors causing these charge carriers to drift towards the readout electronics. The signal from the readout electronics is referred to as a particle *hit*.

The Pixel Detector is composed of three barrel layers and a total of six end-cap disks (three on either side of the barrel). The Insertable B-Layer (IBL) [69] is the fourth, innermost layer added between the beam pipe and the existing Pixel Detector. Installed during the first long shutdown of the LHC (between Run 1 and Run 2), the IBL is designed to enhance the resolution near the beam pipe.

Semiconductor Tracker

Surrounding the Pixel Detector, the Semiconductor Tracker (SCT) [70, 71] is a precise silicon microstrip detector. The SCT is composed of four cylindrical barrel layers and nine disks in each end-cap. Uniform in design, the barrel modules consist of silicon-strip sensors parallel to the beam axis with a pitch of 80 µm and approximate length of 12 cm. At this stage in the ID, lower resolution silicon strips are used to reduce cost whilst maintaining high precision tracking. To mitigate the lower resolution, the silicon strips are arranged in pairs (glued back-to-back) with an angle of 40 mrad between them.

Transition Radiation Tracker

The third and final component of the ID is the Transition Radiation Tracker (TRT) [72]. The basic elements of the TRT are thin-walled drift tubes, referred to as straws, as shown in Figure 4.8. A single straw is 4 mm in diameter with a gold-plated tungsten anode wire at the centre. The TRT only provides $r\phi$ information with a resolution of the order of 100 microns. This lower precision is compensated by a large number of measurements — for particles with $|\eta| < 2$, 35-40 tubes are typically crossed.

The straws are filled with a xenon-based gas mixture. As charged particles pass through a straw, they ionise the gas. The negatively charged electrons drift towards the anode wire and create a signal that is read out by the electronics. Moreover, the transition radiation can provide information of the particle type. As a relativistic particle traverses the boundary between the materials in the TRT, transition radiation photons are emitted. The gas in the straws absorbs these photons and an additional signal is readout. The intensity of the signal is proportional to the Lorentz factor, $\gamma = E/m$, of the particle. Combined with an energy measurement, the TRT can provide information on the particle type [73].

Figure 4.8 is a three-dimensional representation of the three detector subsystems that form ID in the barrel region. The diagram on the right is a schematic representation of a charged particle traversing the layers of ID. Section 6.1 introduces how measurements from the ID are used to reconstruct particle trajectories, referred to as *tracks*.

4.6 Calorimetry

Calorimetry [74] is the process by which a particle's energy is absorbed and the energy deposit is converted into a measurable signal that relates to the particle's energy. In contrast to tracking, the particle is completely absorbed in calorimetry and its trajectory is stopped within the detector.

The ATLAS calorimeter system is divided into an Electromagnetic Calorimeter (ECal) and Hadronic Calorimeter (HCal). The ECal measures charged or neutral particles that interact electromagnetically, such as electrons and photons, whilst the HCal measures strongly interacting particles. Calorimeters can be

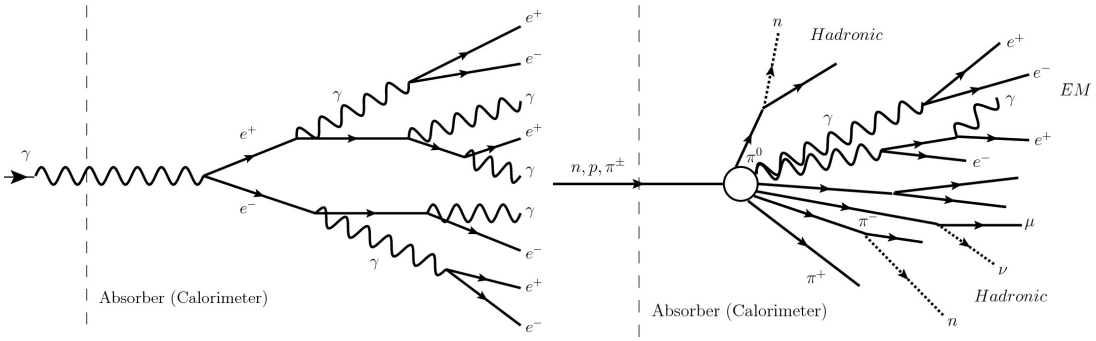

(a) *Electromagnetic shower* **(b)** *Hadronic shower*

Figure 4.9 *(a) Electromagnetic shower initiated by a high-energy photon. (b) Hadronic shower initiated by high-energy protons, neutrons or pions. Figures from Ref. [75].*

further classified according to their design. ATLAS adopts sampling calorimetry technology for both the electromagnetic and hadronic calorimeters. Sampling calorimeters consist of alternating layers of *absorbing* and *active* materials. Absorbing layers consist of a high-density material used to stop incoming particles by creating a shower of secondary particles with a lower energy. The active layers measure the energy deposited by the charged particles in the shower.

4.6.1 Electromagnetic and hadronic showers

As high-energy electrons interact in a medium, photons are radiated through bremsstrahlung. These photons in turn produce electron-positron pairs through pair production. This process of bremsstrahlung and pair production continues to produce a cascade of photons, electrons and positrons, known as an electromagnetic shower illustrated in Figure 4.9a. The radiation length, X_0, characterises electromagnetic interactions of high-energy electrons and photons in matter. X_0 is a material property that depends on the density and atomic number of the medium. The shower continues until the average energy of the particles falls below the critical energy, at which point electrons and positrons lose energy primarily via ionisation. Consequently, the shower has a maximum number of particles for a given number of radiation lengths.

Charged hadrons, such as protons and charged pions, traversing matter lose energy through ionisation. Furthermore, both charged and neutral hadrons can interact via the strong force with the nuclei in the medium. Particles produced in the primary hadronic interaction subsequently interact further down stream in

the medium giving rise to a cascade of particles. In contrast to electromagnetic showers which develop uniformly, hadronic showers are more variable since there are many possible final states. Additionally, any neutral pions, π^0, produced in the shower decay instantaneously by $\pi^0 \to \gamma\gamma$ resulting in an electromagnetic component of the shower [75] as illustrated in Figure 4.9b.

Calorimeters must provide good containment of the electromagnetic and hadronic showers and so calorimeter depth is an important design consideration.

4.6.2 Energy resolution

The precision with which calorimeters measure energy is referred to as the energy resolution. The measured energy in a calorimeter fluctuates around the true energy of the shower and so the relative energy resolution is defined as

$$\frac{\sigma_E}{E} = \frac{a}{\sqrt{E}} \oplus \frac{b}{E} \oplus c, \tag{4.8}$$

where $\oplus$ indicates a quadratic sum. The terms a, b and c are the stochastic, noise and constant terms respectively. The stochastic term is due to the fluctuations in the shower development. The noise term arises from the electronic noise of the readout system and pile-up. The constant term accounts for nonuniformities in the detector responses, such as imperfections in the detector geometry or radiation damage [76].

4.6.3 Liquid Argon Calorimeter

The high granularity LAr Calorimeter [77], surrounding the ID, is divided into three sections as shown in Figure 4.10:

1. the Electromagnetic Calorimeter (ECal) in the barrel ($|\eta| < 1.475$) and end-cap ($1.37 < |\eta| < 3.2$) regions;
2. the Forward Calorimeter (FCal) providing additional electromagnetic coverage in the forward region ($3.1 < |\eta| < 4.9$); and
3. the Hadronic End-Cap (HEC) covering $1.4 \leq |\eta| \leq 3.2$.

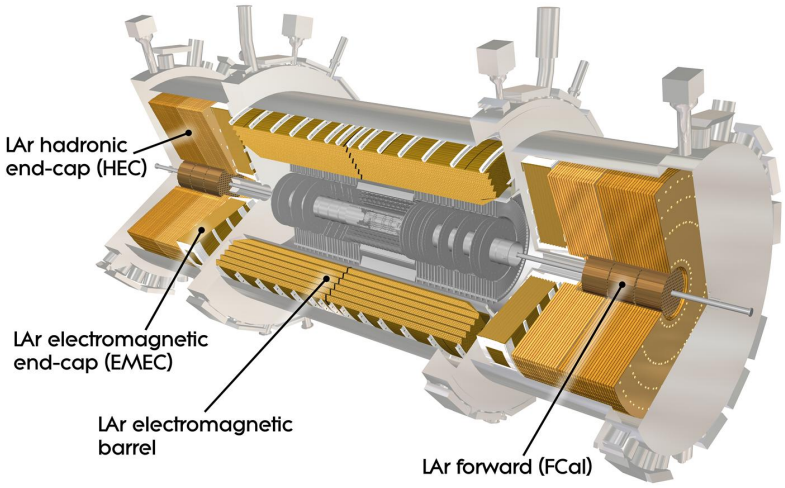

Figure 4.10 *Cross-section view of the ATLAS Liquid Argon (LAr) calorimetry system. Figure from Ref. [78].*

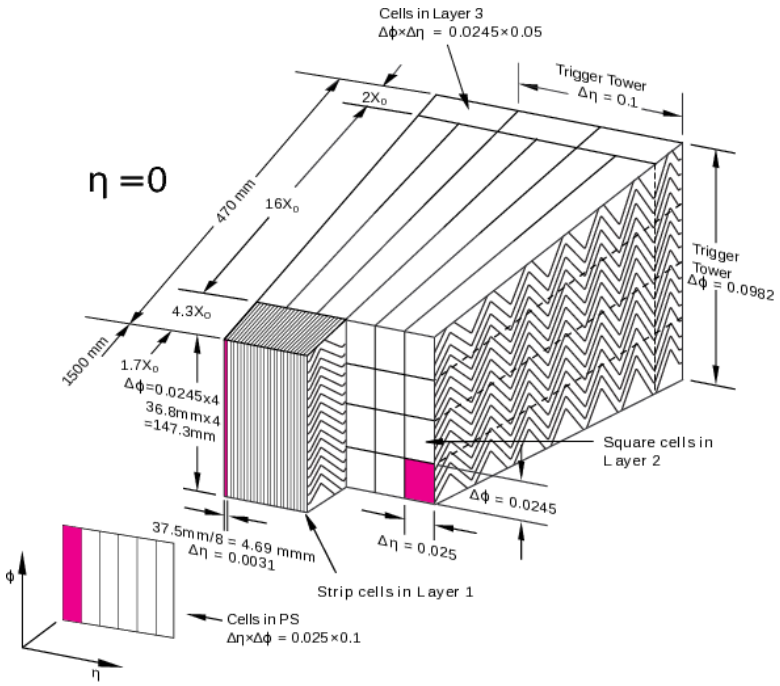

Figure 4.11 *Schematic of the accordion-shaped structure of the Electromagnetic Calorimeter (ECal). The granularity in (η, ϕ) of the cells within each of the three layers is illustrated. Additionally, the trigger towers are shown. Figure from Ref. [77].*

The LAr sampling technique, utilising *accordion-shaped* absorbers and electrodes, is adopted for the ECal. Lead layers absorb the incoming particles and subsequently create a shower of secondary particles. Within the active layer, the secondary particles ionise the liquid argon producing a measurable electric current. By measuring the detected currents, the energy of the original particle can be determined.

The characteristic accordion structure, shown in Figure 4.11, provides a large acceptance and uniform response over the full azimuthal range reducing the possibility of particles going undetected. The ECal has three active layers in the barrel region and two in the higher-η end-cap region ($2.5 < |\eta| < 3.2$). Figure 4.11 illustrates the layers within the barrel region of the ECal.

The first layer is the most finely segmented in η to allow for the separation of closely spaced photons, helping to distinguish between single photons and photons from π^0 decays. Since the largest fraction of energy is deposited in the second layer, this layer performs the main energy measurement. The third layer collects only the tail of the electromagnetic shower and so has the lowest granularity in η. A presampler (a thin LAr layer) compliments the ECal between $0 < |\eta| < 1.8$ to provide a measurement of the energy lost before the ECal.

In addition to the separation of photons from π^0 decays, the ECal is designed with a high granularity in the η direction for a number of reasons. A fine segmentation in η allows for precise measurements of shower width and shape which are used in photon identification. Moreover, a technique know as *pointing* [79] (detailed in Section 7.5.3) exploits the longitudinal segmentation of the ECal to locate the interaction point within a few tens of millimeters. This places a crucial role in the reconstruction of photon interaction vertices.

4.6.4 Tile Calorimeter

Surrounding the LAr calorimeter, the Tile Calorimeter (TileCal) [80] measures the energy of hadronic particles that do not deposit all their energy in the LAr calorimeter. The TileCal is divided into three parts: the central barrel region ($|\eta| < 1.0$) and two extended barrel regions ($0.8 < |\eta| < 1.7$). As a sampling calorimeter, it consists of steel layers and plastic scintillating tiles as the active medium. Similar to the LAr calorimeter, particles hit the steel layers and produce a shower of new particles. The plastic scintillators produce photons which can be

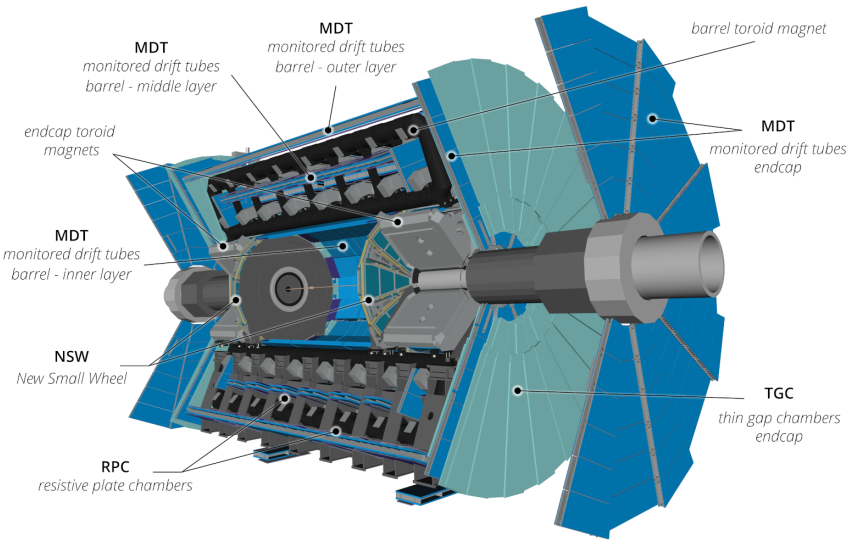

Figure 4.12 *Cross-section of the ATLAS muon system. Figure from Ref. [55].*

converted into a measurable electric current where the intensity is proportional to the original particle's energy. The scintillating light produced in the tiles is transmitted by wavelength shifting fibres to photomultiplier tubes (PMTs).

4.7 Spectrometry: the Muon Spectrometer

High-energy muons are minimally ionising and can penetrate through the thick layers of the ATLAS calorimeter system. As the outermost layer of the ATLAS detector, the Muon Spectrometer (MS) [81] is designed to measure the momenta of muons. It has stand-alone triggering and momentum measurement capabilities and uses a combination of precision and fast-response detectors to measure muon trajectories and momenta.

In the barrel region ($|\eta| \leq 1$), precision measurements of muon coordinates are provided by Monitored Drift Tubes (MDTs). The MDTs are positioned in and around the eight coils of the barrel toroid magnet. Composed of 3 cm wide aluminium tubes with a gold-plated tungsten-rhenium wire at the centre, MDTs are filled with a gas mixture designed to be ionised as a muon passes through.

The transition ($1 \leq |\eta| \leq 1.4$) and end-cap ($1.4 \leq |\eta| \leq 2.7$) regions of the MS are arranged perpendicular to the beam pipe in *wheels*. In the forward regions of the endcaps, close to the beam pipe, Cathode Strip Chambers (CSCs) with higher granularity are used to withstand higher rate conditions. The innermost

wheel in the MS endcap system was replaced entirely for Run 3 of the LHC with the New Small Wheel [82]. Figure 4.12 shows a cross-section view of the MS system illustrating the layout of the MDTs and the CSCs.

The fast-response detectors within the MS form part of the trigger system (introduced in Chapter 5) in the range $|\eta| \leq 2.4$. Resistive Plate Chambers (RPCs) are used in the barrel region whilst Thin Gap Chambers (TGCs) are used in the end-cap regions. The combined data from the fast-response detectors gives a coarse measurement of muon momentum. This information is used to decide whether to keep the event for further analysis.

4.8 Detector and accelerator upgrades

The initial installation of the ATLAS detector took place in 2008. Since then, it has undergone several hardware upgrades. The LHC most recently completed the second long-shutdown period (2018–2021) in preparation for Run 3. This period was used to implement the Phase-I [83] upgrades to the ATLAS detector. The main focus of this upgrade was to enhance the performance of the trigger system (introduced in Chapter 5), with a particular emphasis on maintaining the Level-1 (L1) hardware trigger rate at a manageable level.

After Run 3, the Phase-II [84] upgrade of the ATLAS detector is scheduled in preparation for the High Luminosity LHC (HL-LHC) [52]. The HL-LHC will provide unprecedented luminosities reaching a peak instantaneous luminosity of $\mathcal{L} = 7.5 \times 10^{34}\,\mathrm{cm}^{-2}\,\mathrm{s}^{-1}$, equivalent to approximately 200 pp collisions per bunch crossing. Moreover, the HL-LHC is predicted to increase the integrated luminosity by a factor of 10 beyond the design value of the LHC. Achieving such levels of integrated luminosity will be extremely beneficial for analyses that are statistically limited, such as the one presented in this thesis.

Chapter 5

The ATLAS trigger system

In this chapter, I introduce the ATLAS trigger system responsible for selecting and storing events of interest during data taking. The chapter provides a brief overview of the two-level architecture in the trigger system: the hardware-based Level-1 (L1) trigger and the software-based High-Level Trigger (HLT). A particular focus is given to the photon and diphoton triggers used in the $H \to \gamma\gamma$ analysis.

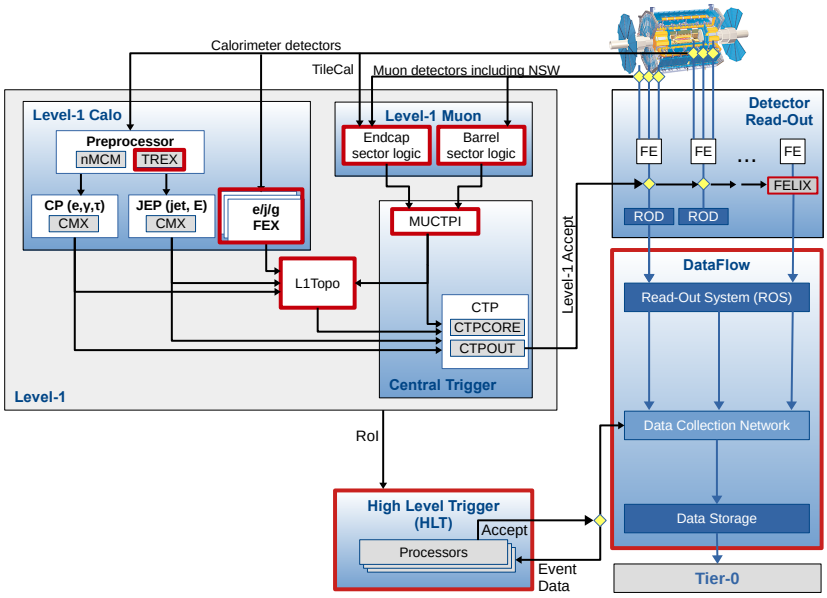

Figure 5.1 *The ATLAS Trigger and Data Acquisition system for Run 3. Specific updates for Run 3 are highlighted in red. Figure from Ref [85].*

5.1 Trigger and data acquisition

The aim of the ATLAS trigger system [86, 87] is to minimise the rate of recorded events whilst maintaining an excellent efficiency for interesting processes. It is neither possible nor desirable to store all data collected from pp collisions. Since interesting physics processes are rare, physicists are only interested in a small fraction of the events recorded at the LHC. It is also very expensive to store all events and so it is essential to reduce the rate of recorded events to a manageable level. The trigger system is therefore designed to keep only *events of interest* such as diphoton events for this thesis. Events are recorded at a rate of approximately 1 kHz from the LHC bunch crossing rate of 40 MHz.

Triggers employ a fast event rejection system used to quickly decide on whether to store an event for further analysis. These decisions are made based on characteristics of the event. It is common for triggers to use pre-defined thresholds on the energy or momentum of the particles in the event. The Trigger and Data Acquisition (TDAQ) system [88], shown in Figure 5.1, is responsible for the selection and recording of events. The trigger system has a two-level architecture: the hardware-based Level-1 (L1) trigger and the software-based High-Level Trigger (HLT).

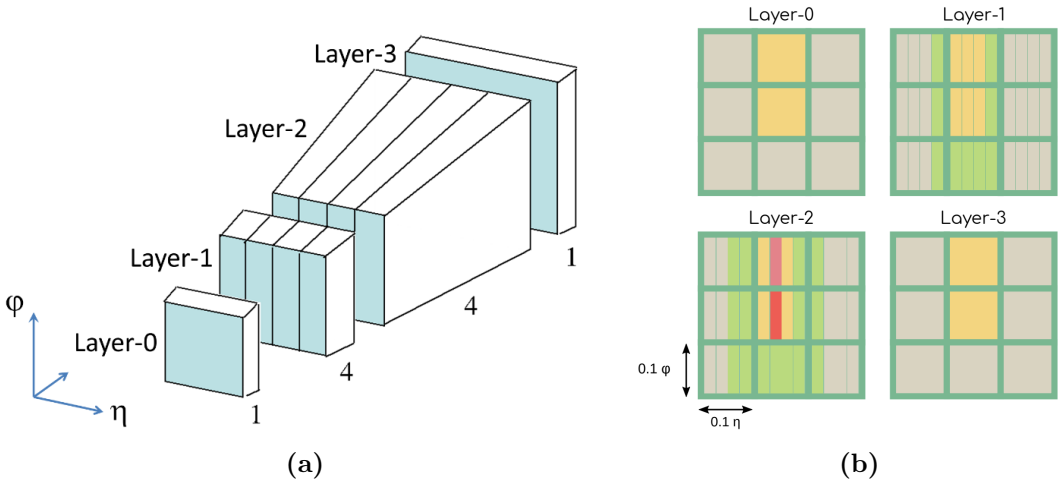

Figure 5.2 *(a) Granularity of the upgraded $\Delta\eta \times \Delta\phi = 0.1 \times 0.1$ trigger tower in the ECal for Run 3. The 1-4-4-1 architecture of the SuperCell provides ten energy values. Figure from Ref. [89]. (b) Cells of the ECal layers used by the L1 algorithm to build the RoIs. The red cell represents the local maximum, the pink is the most energetic neighbour in ϕ, clustering is represented by yellow cells and green cells are used for the isolation cuts. Figure from Ref. [90].*

5.2 Level-1 trigger

The L1 trigger [91, 92] is a hardware-based system using custom-built electronics to trigger on information from the calorimeter (L1Calo) and muon (L1Muon) detectors. With a low latency of less than 2.5 µs, the L1 trigger allows for quick decision-making in real time.

In this thesis, only events satisfying the single or diphoton triggers are considered in the $H \to \gamma\gamma$ measurement. The L1 trigger identifies a single electromagnetic object, or a pair of electromagnetic objects, passing a transverse energy, E_{T}, threshold. This is achieved by scanning the coarse information from the calorimeter with a $\Delta\eta \times \Delta\phi = 0.1 \times 0.1$ granularity to search for a potential region of interest (RoI) that exhibits these characteristics. A RoI is a defined space in the detector, identified by the L1 trigger, that is worth reconstructing in the HLT to search for interesting physics objects. Events passing the L1 trigger selection are sent to the central trigger processor to form the L1 trigger decision. The number of events passing a trigger per unit time is referred to as the *trigger rate*. The L1 trigger reduces the collision rate from 40 MHz to less than 100 kHz.

High pile-up levels associated with increasing luminosity degrade calorimeter resolution, thereby decreasing trigger efficiency. In preparation for Run 3, the L1Calo system was therefore upgraded to increase the granularity of the LAr trigger input in the ECal. Instead of a single trigger tower which combines all four layers of the ECal, they are read out separately. Moreover, in the first and second layer of the ECal, the granularity is increased four times in η. Figure 5.2a shows the new *SuperCell* granularity of each $\Delta\eta \times \Delta\phi = 0.1 \times 0.1$ trigger tower with a 1-4-4-1 sampling architecture used to provide ten energy values where the legacy system only provided one.

Furthermore, new feature extractor sub-systems were added to the L1Calo [93] with new reconstruction algorithms installed. Most notably for this thesis is the new Electromagnetic Feature Extractor (eFEX) trigger, exploiting the full SuperCell granularity to reconstruct electromagnetic objects. Figure 5.2b shows the cells of the ECal layers used in the L1 algorithm to build an RoI. These algorithms use a 0.3×0.3 window, as shown in Figure 5.2b, and select the local maximum of energy using only the second layer of the ECal as the seed cell (shown in red). Following this, the most energetic neighbouring cell in ϕ is selected (shown in pink) and the cluster is built (adding the cells in yellow) [90].

The legacy L1Calo triggers were used for 2022 data taking and the new eFEX triggers were used for 2023 data taking.

5.3 High-level trigger

The HLT [95] is a software-based system using dedicated reconstruction and selection algorithms based on the Athena offline software framework. Both fast trigger algorithms for early rejection and more precise, CPU-intensive algorithms are used in the HLT to reconstruct physics objects in real time, a process referred to as *online* reconstruction. Track reconstruction in the HLT follows a two-stage approach. The first stage is the fast track reconstruction, referred to as *fast tracking*. Fast tracking runs a custom pattern recognition stage and performs a quick fit to track candidates. Events of low interest are immediately rejected. The second stage is a slower, more precise reconstruction, referred to as *precision tracking*, which runs over all remaining events. Precision tracking refits all track candidates that have passed the fast tracking using a version of the full *offline* track reconstruction discussed in Section 7.2 [96].

Table 5.1 *Single photon and diphoton triggers [94] used in the Run 3 $H \to \gamma\gamma$ analysis. For the diphoton HLT trigger, the E_T selection is presented as $E_T >$ leading (sub-leading) photons. The photon candidate must also satisfy identification criteria based on the shower shape in the calorimeters.*

Trigger chain	L1 selection [GeV]	HLT selection [GeV]	Photon identification
2022 data taking			
Single photon	$E_{\mathrm{T}} > 22$	$E_{\mathrm{T}} > 140$	*loose* requirement
Diphoton	$E_{\mathrm{T}} > 20$	$E_{\mathrm{T}} > 35$ (25)	*medium* requirement
2023 data taking			
Single photon	$E_{\mathrm{T}} > 26$	$E_{\mathrm{T}} > 140$	*loose* requirement
Diphoton	$E_{\mathrm{T}} > 24$	$E_{\mathrm{T}} > 35$ (25)	*medium* requirement

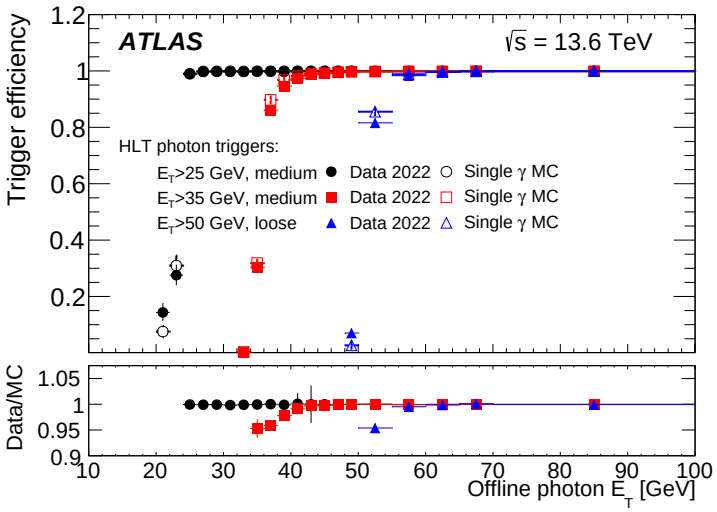

Figure 5.3 *Efficiency of the diphoton triggers for 2022 data taking as a function of the offline photon E_T. Efficiency is given with respect to the offline photons reconstructed with the tight identification and isolation requirements. Figure from Ref. [89].*

A dedicated computing farm is used to run HLT algorithms with a latency of around 500 ms. The HLT has an output rate of approximately 1 kHz, which is the maximum rate at which data can be written from detector to disc. Once an event is accepted by the HLT, the data is sent to permanent storage.

The combination of a L1 trigger item and a series of HLT algorithms is known as a *trigger chain*. Trigger chains are employed to select events of interest based on the physics signature. For an event to pass the HLT, it must pass all the selection criteria in the trigger chain. The trigger chains used to select the diphoton events used in this thesis are presented in Table 5.1. Figure 5.3 shows the efficiency of the diphoton trigger for 2022 data taking.

5.4 Trigger operations

Whilst the LHC is in operation, a shift crew is responsible for running and monitoring the ATLAS detector from Point-1 — where the detector cavern and control room are located. A team of trigger experts oversee the operation and data quality monitoring of the trigger system.

The full list of trigger chains used for data taking is known as the *trigger menu*. The trigger menu is adaptable to a variety of LHC beam conditions. During each fill cycle of the LHC, the instantaneous luminosity declines and resource availability increases. By applying *prescale factors*, trigger rates can be adjusted during the fills to maximise the usage of available resources. Prescales are used live from the control room to enable or disable triggers or execute them at a reduced rate. For a prescale value of n, an event has a $1/n$ probability of being kept by the trigger system.

Trigger rates are good indicators of the trigger system performance; they are highly sensitive to problems that could impact data taking. Rate monitoring is therefore essential for the smooth operation of the ATLAS Experiment.

Chapter 6

Trigger development for Run 3

In this chapter, I discuss my technical work on developing the trigger system for Run 3 data taking. The first technical project presented in this chapter is the optimisation of the Inner Detector (ID) tracking strategy in the HLT for the B-physics trigger signature. For this task, I worked closely with the ID trigger group to optimise the tracking architecture and ultimately improve the tracking efficiency. The second technical task presented in this chapter is the development of the Trigger Rate Presenter (TRP) dashboard for Run 3. I took over the role as main developer of TRP from the previous PhD student, Neofytos Themistokleous. His work focused on the upgrade and deployment of the new web-based dashboard in preparation for Run 3 data taking. Once the dashboard was fully operational, I worked on improving the user interface and experience for the shift crew and experts during data taking.

6.1 Optimisation of the Inner Detector tracking strategy in the HLT

This section discusses a technical project delivered as part of this thesis optimising the ID tracking strategy used in the B-physics trigger signature. The work presented in this section demonstrates how optimising HLT algorithms can improve the performance of the trigger system for Run 3 data taking.

In preparation for the increased luminosities expected in Run 3, upgrades to the trigger system were required. A particular focus was placed on optimising the HLT software to maintain trigger efficiencies whilst reducing resource consumption. Performing track reconstruction within a region of interest (RoI) is one example of conserving resources by limiting the detector region that is reconstructed. The default RoI parameters for ID trigger tracking are $\Delta\eta \times \Delta\phi = 0.75 \times 0.75$ extending in $z = \pm 225\,\text{mm}$ [97]. Using a fixed RoI size for all physics signatures, however, can lead to inefficiencies in the trigger system.

The aim of this study was to optimise the RoI parameters for the B-physics dimuon signature whilst maintaining signal efficiency. For the B-physics dimuon signature, the RoI setup was problematic for two reasons: RoIs can overlap leading to multiple copies of the same track; and the RoI extends the full $\pm 225\,\text{mm}$ range around the muon z position. The tracking timing and efficiency of the trigger reconstruction were therefore studied for varying RoI parameters.

The samples used in this study are simulated Run 2 data at a centre-of-mass energy of $\sqrt{s} = 13\,\text{TeV}$. The three samples studied include $B_S^0 \to J/\psi\phi$, $B^+ \to J/\psi K^+$ and $B_d \to K^*\mu\mu$. All events were generated using Pythia8 [98] and the CTEQ6L1 PDF set according to the A14 tune [99].

The HLT configuration of the B-physics dimuon trigger has five steps; the first four steps are muon triggers and the fifth step is the B-physics dimuon trigger. Changing the RoI size for the B-physics tracking only affects the number of events passing the B-physics dimuon step in the trigger chain — the muon triggers are unaffected. The efficiency is therefore calculated as the number of events passing the B-physics dimuon trigger over the first muon trigger in the trigger chain. To test the trigger efficiency, the trigger reconstruction was run whilst varying the $\Delta\eta \times \Delta\phi$ size and z-width of the RoI.

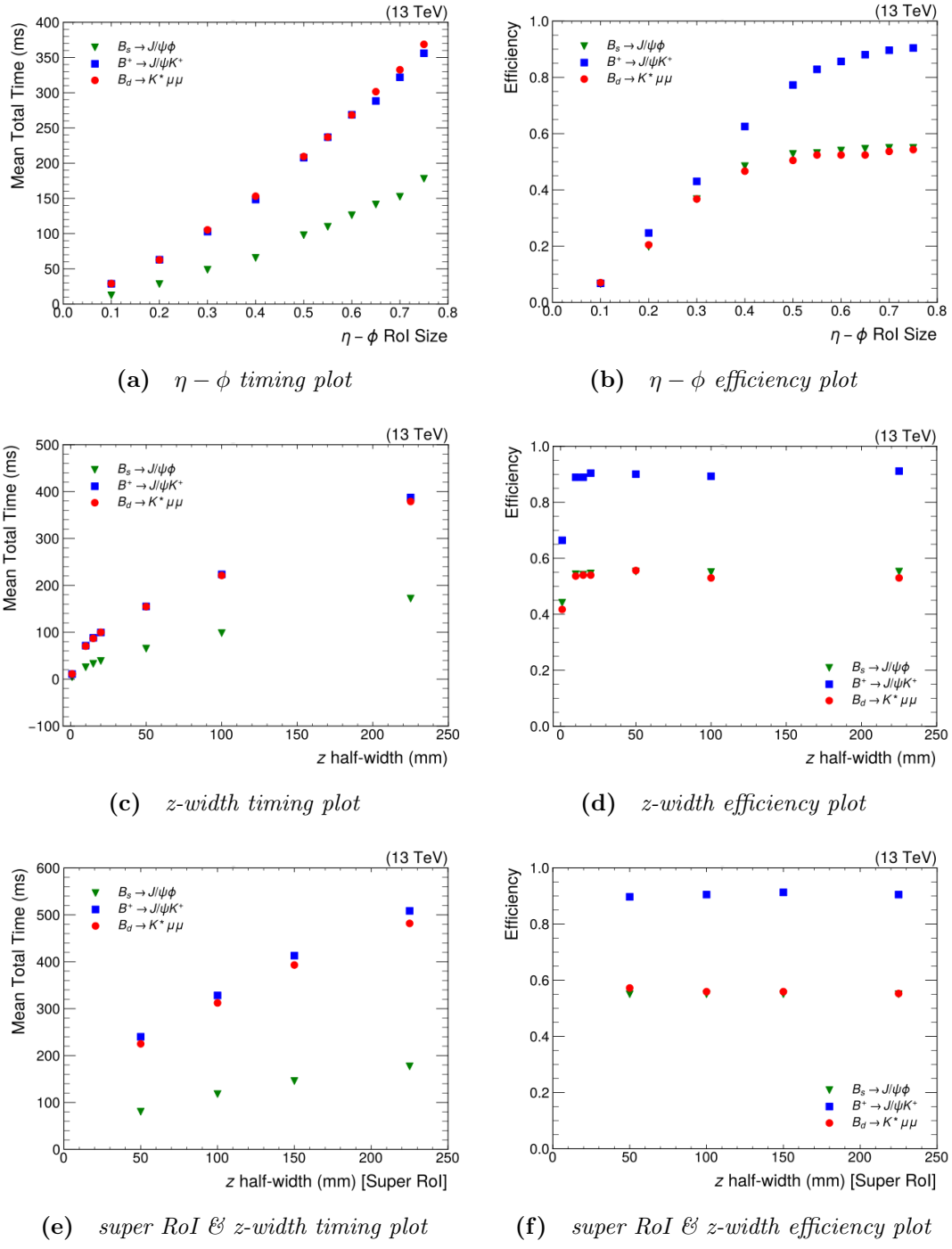

(a) *$\eta - \phi$ timing plot* **(b)** *$\eta - \phi$ efficiency plot*

(c) *z-width timing plot* **(d)** *z-width efficiency plot*

(e) *super RoI & z-width timing plot* **(f)** *super RoI & z-width efficiency plot*

Figure 6.1 *The mean total time to run the trigger reconstruction as a function of: (a) the $\Delta\eta \times \Delta\phi$ size of the RoI; (c) the z-width of the RoI; and (e) the z-width of the super RoI. The efficiency of the trigger reconstruction as a function of: (b) the $\Delta\eta \times \Delta\phi$ size of the RoI; (d) the z-width of the RoI; and (f) the z-width of the super RoI.*

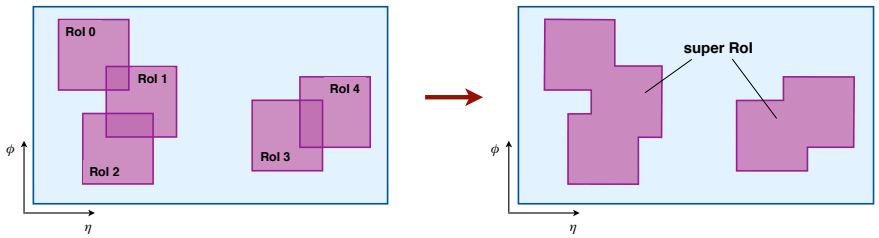

Figure 6.2 *Diagram illustrating how the super RoI tool reduces multiple processing in the trigger resulting from overlapping RoI in the detector. Figure from Ref [96].*

Reducing the $\Delta\eta \times \Delta\phi$ acceptance decreases the tracking timing as shown in Figure 6.1a. This, however, introduces a reduction in efficiency as Figure 6.1b demonstrates, particularly for the $B^+ \to J/\psi K^+$ channel. To maintain signal efficiency, the $\Delta\eta \times \Delta\phi$ size of the RoI was not reduced.

A similar study shows the tracking timing decreases as the z-width is reduced as shown in Figure 6.1c. Figure 6.1d shows that the efficiency remains roughly constant up to around $z = 10\,\text{mm}$. Decreasing the z-width from $z = 225\,\text{mm}$ to $z = 50\,\text{mm}$ reduces the tracking timing by approximately 60% for each sample whilst maintaining constant efficiency.

A further study using a *super RoI* was performed. The original tracking for the B-physics dimuon signature uses two separate RoIs around each muon. To reduce the overlap in using two RoIs, a new super RoI tool was implemented to form around both muons. Figure 6.2 illustrates how the super RoI is formed to reduce the overlap in the detector. Applying the super RoI tool with the default values for $\Delta\eta \times \Delta\phi$ and z-width introduces a 40% reduction in tracking timing. Combining the super RoI tool with $z = 50\,\text{mm}$ reduces the tracking timing by approximately 70% for each sample, as shown in Figure 6.1e, whilst maintaining constant efficiency in Figure 6.1f.

All the results presented in Figure 6.1 are based on Monte Carlo (MC) samples generated for Run 2 data. The results were validated on a sample of Run 3 data taken in 2022. In conclusion, reducing the z-width of the RoI has the greatest impact on reducing the tracking timing for the B-physics dimuon signature. Implementing the super RoI tool in addition to the z-width reduction has significantly reduced the tracking timing whilst maintaining excellent signal efficiency for data taking. The new super RoI tool for the B-physics dimuon signature combined with a z-width reduction to $z = 50\,\text{mm}$ is now being used in the ATLAS Run 3 trigger system.

6.2 Trigger Rate Presenter

This section discusses the development of the Trigger Rate Presenter (TRP) dashboard for Run 3. The technical work completed as part of this thesis focused on improving the dashboard user interface and experience for the shift crew and experts during Run 3 data taking. Ref. [100] details the development and deployment of a new web-based dashboard in preparation for Run 3.

The TRP dashboard is the primary tool used by shifters and experts to monitor live trigger rates in the ATLAS control room. The software application computes and visualises trigger rates and run information in real time. Furthermore, the TRP software archives rates for later offline reference. To enable easier rate monitoring outside Point-1, TRP has been upgraded to an entirely web-based dashboard [101].

The ATLAS Information Service (IS) [102] is a component of the TDAQ infrastructure. All TDAQ and detector applications publish information to the IS that is primarily used for online monitoring. Persistent Back-End for the ATLAS IS system of TDAQ (P-BEAST) [103] is a time-series database that stores operational data; it has the capacity to serve clients with data in quasi real-time, making it the ideal data source for web-based dashboards. Grafana [104] is an open source analytics and monitoring software designed for visualising data as a time series in a web browser. The new TRP dashboard is implemented on top of the Grafana dashboard builder and served the data by the P-BEAST persistency service.

TRP dashboard development

Figure 6.3 shows a snapshot of the new TRP dashboard as displayed in the ATLAS control room. The first panel shows the current status of ATLAS providing information such as the run number, beam status and trigger menu setup. At the top of the dashboard, there are various filtering options in the form of a text box or drop-down lists which were implemented as part of the technical work presented in this thesis. The L1 rate panel highlights advanced filtering options implemented on the dashboard:

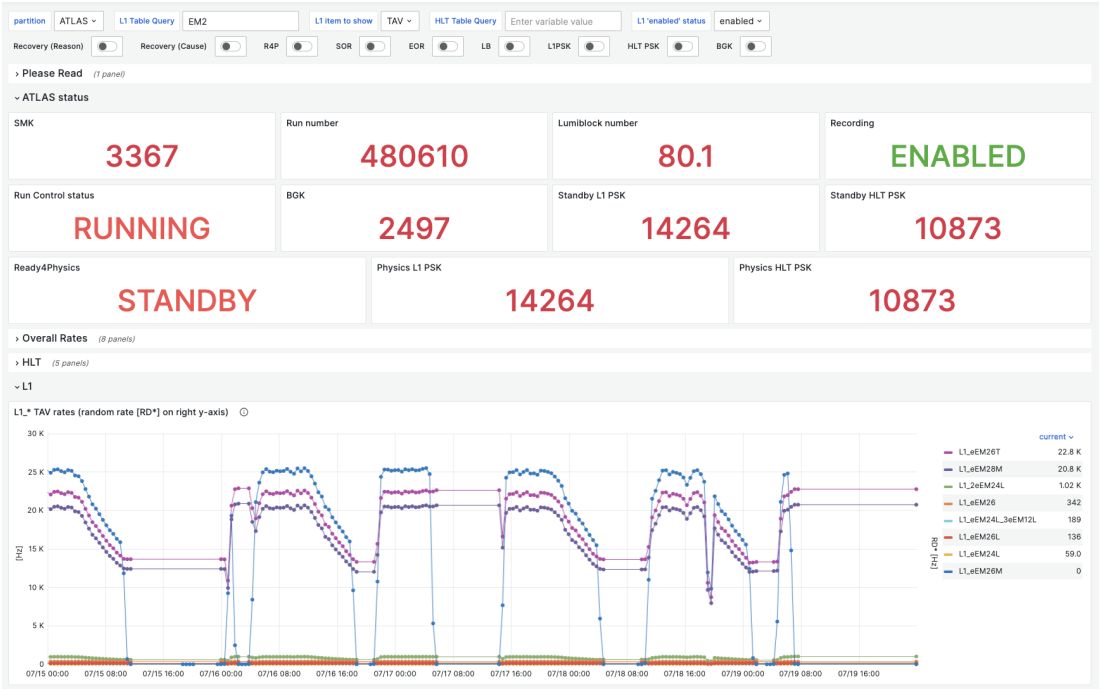

Figure 6.3 *A snapshot of the TRP dashboard as displayed in the ATLAS control room. At the top of the dashboard are various filtering options in the form of a text box or drop-down lists. The first panel shows the run status of ATLAS. The L1 rate panel highlights different filtering abilities on the dashboard.*

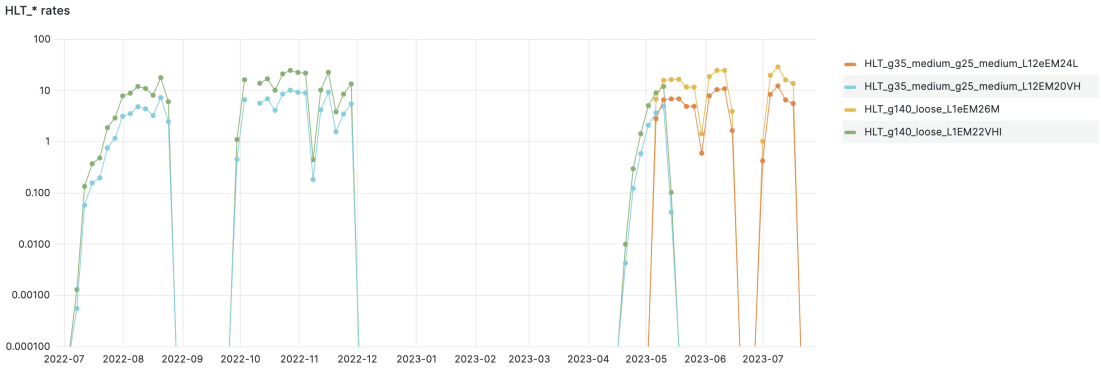

Figure 6.4 *Trigger rates for the photon triggers used in the $H \to \gamma\gamma$ analysis during 2022 and 2023 data taking. The green and blue lines represent the single and diphoton triggers respectively for the legacy L1 triggers. The single and diphoton triggers are shown in orange and red respectively for the new eFEX triggers commissioned during 2023 data taking.*

- `L1 Table Query` filters L1 items based on the trigger name, such as `EM2`;
- `L1 item to show` has the option to display trigger after veto (TAV) or trigger after prescale (TAP) rates; and
- `L1 'enabled' status` filters L1 rates based on the prescale status of the trigger.

The L1 panel in Figure 6.3 therefore displays TAV rates for all L1 triggers matching `EM2` that are enabled in the trigger menu.

Figure 6.4 shows the HLT rate panel on the TRP dashboard filtered to display the photon triggers used in the $H \to \gamma\gamma$ analysis during 2022 and 2023 data taking. The legacy L1 triggers, used for 2022 data taking, are shown for the single (green line) and diphoton (blue line) triggers. The decommissioning of the legacy L1 triggers during 2023 data taking is shown as the new eFEX triggers were commissioned for the single (orange line) and diphoton (red line) triggers.

The new TRP dashboard has been fully operational in the ATLAS control room since the start of Run 3 data taking in 2022.

Chapter 7

Reconstruction and physics objects

In reality, the ATLAS detector cannot measure the properties of particles directly. In this chapter, I discuss how detector signals from events stored by the trigger are reconstructed to identify physics objects, such as photons. Physics objects are the starting point for any ATLAS physics analysis. This chapter discusses, photons, electrons, muons, jets and missing transverse energy used in the $H \to \gamma\gamma$ cross-section measurement.

7.1 Physics objects for $H \to \gamma\gamma$ analyses

The physics objects of interest in this analysis depend on the production mode and decay channel of the Higgs boson. For ggF and $q\bar{q} \to H$ Higgs production in the $H \to \gamma\gamma$ decay channel, the experimental signature consists of two high-energy photons. The interpretation of the Yukawa coupling in the $H \to \gamma\gamma$ decay channel presented in Chapter 11 therefore analyses predominantly photon objects.

The work in this thesis, including Chapters 9 and 10, was performed within the ongoing Run 3 differential cross-section measurement. This measurement uses other production modes discussed in this thesis, namely VBF, VH and $t\bar{t}H$, which have additional signatures beyond the two high-energy photons as the Feynman diagrams in Figure 3.3 illustrate.

- VBF production is characterised by two outgoing quarks, observed as two forward jets in the detector.
- VH production is characterised by the decay products of a Z or W boson. In the case of a Z boson, the decay products could be two charged leptons or two neutrinos, the latter identified by missing energy in the detector. The decay products could be jets or a charged lepton and a neutrino from the hadronic and leptonic decay of the W-boson respectively.
- $t\bar{t}H$ production is characterised by two outgoing top quarks, observed in the detector as b-jets from the top quark decay and the decay products of the W boson.

This chapter will therefore discuss the reconstruction of photons, electrons, muons, jets and missing transverse energy.

7.2 Track reconstruction

The trajectories of charged particles, or *tracks*, were introduced in Section 6.1 as the basis for track reconstruction in the trigger system. Tracks play an important role in the reconstruction of the primary vertex and charged particles, the removal of pile-up and flavour tagging of jets. Experimental signatures left in the ID from charged particles traversing the detector are used to reconstruct tracks.

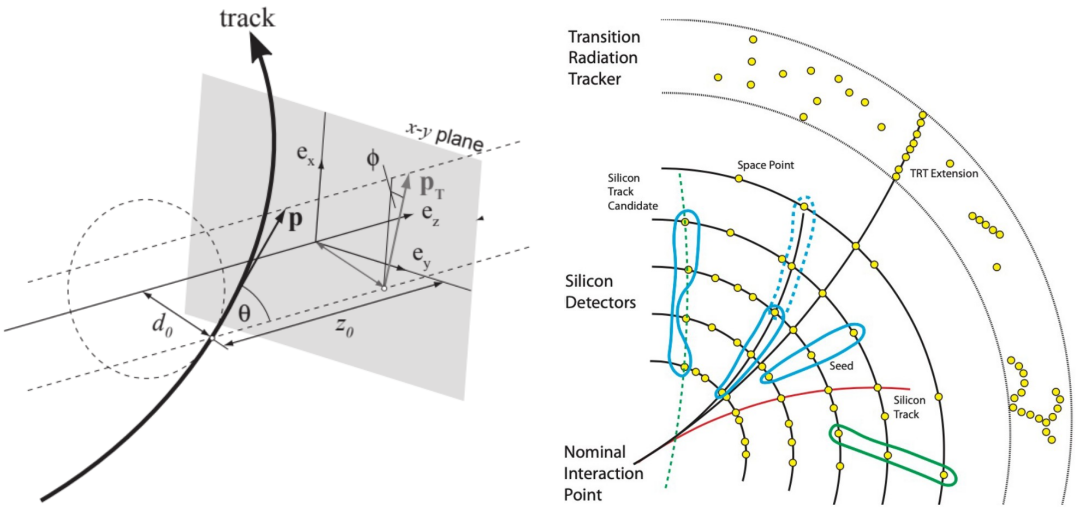

(a) *Track perigee representation* **(b)** *Track reconstruction*

Figure 7.1 *(a) Global track parameters using perigee representation: azimuthal angle, ϕ, polar angle, θ, transverse and longitudinal impact parameters, d_0 and z_0, and charge-to-momentum ratio, q/p. The point of reference is the interaction point in the detector. (b) Schematic of the track reconstruction algorithm in the ID. See text for more details. Figures from Ref. [105] and Ref. [106] respectively.*

In the presence of a magnetic field, charged particles follow a helical trajectory. A particle track in the ID is characterised using five parameters defined with respect to a reference point as illustrated in Figure 7.1a. The reference point is defined as the average position of pp interactions in the detector, known as the *beamspot position*. ATLAS employs a *perigee* representation [105] where track properties are measured at the point of closest approach to the beamline. These five parameters include the azimuthal angle, ϕ, the polar angle, θ, the transverse and longitudinal impact parameters, d_0 and z_0, and the charge-to-momentum ratio, q/p. The transverse impact parameter, d_0, represents the shortest distance between the track and the beamspot position in the transverse plane. The longitudinal impact parameter, z_0, corresponds to the distance of closest approach to the beamspot position in the longitudinal plane (along the beamline).

The track reconstruction algorithm [107] is split into four steps: clusterisation, track finding, ambiguity solving and extension to the TRT. The first stage of track reconstruction is the formation of clusters of hits in the ID. Three-dimensional measurements known as *space points* are formed from the clusters of hits, representing the point where a charged particle traversed the active material of the ID.

Table 7.1 *Quality criteria for track candidates to pass the ambiguity solver.*

Track quality criteria	
Track p_{T}	$p_{\mathrm{T}} > 400\,\mathrm{MeV}$
Pseudorapidity	$\lvert\eta\rvert < 2.5$ (from the detector acceptance)
N_{clusters}	≥ 7 clusters (12 expected)
Shared clusters	≤ 1 Pixel-only $\cup$ 2 SCT-only in the same layer
Holes	≤ 2 holes in Pixel & SCT $\cap \leq 1$ hole in Pixel
Impact parameters	$\lvert d_0\rvert < 2\,\mathrm{mm}$ and $\lvert z_0 \sin\theta\rvert < 3\,\mathrm{mm}$

Three space points reconstructed in the Pixel and SCT detectors combine to form a track seed as shown in Figure 7.1b. Seeds are classified as Pixel-only, SCT-only or mixed seeds. At this stage, cuts are applied to the seeds to improve the track purity defined as the fraction of seeds that result in good quality tracks. A combinatorial filter, known as a Kalman Filter [108], is used to build track candidates from track seeds and the remaining layers of the Pixel and SCT detectors. After all realistic combinations of space points are considered, an ambiguity solver is required to resolve track candidates with overlapping space points.

In the ambiguity solver [109], a quality score is assigned to each track based on simple measures of track quality. For example, expected clusters in a sensitive detector element that are missing along the track trajectory (known as holes) decrease the quality score. Track candidates are rejected by the ambiguity solver if they fail to meet the basic quality criteria summarised in Table 7.1.

Finally, track candidates that meet the quality criteria in Table 7.1 are fitted using the high-resolution ATLAS global fit tracker and added to the final track collection. Delaying the track fit until the final stage minimises the computational cost of the track reconstruction algorithm. At this stage, track candidates are extended to include space points in the TRT and a final track refit is performed to improve the momentum resolution.

7.3 Primary vertex

The *primary vertex* defines the location in the detector where the *pp* interaction with the highest momentum transfer between the protons, the so-called *hard process*, takes place. The primary vertex reconstruction [110] is split into two

stages: vertex finding and vertex fitting. Tracks that meet the quality criteria in Table 7.1 are used as input to the algorithm. A seed position is selected as the first vertex candidate. A combination of tracks and the seed position are used to identify the best vertex position. This process is iterative; in each iteration less compatible tracks are down-weighted and the vertex position is recomputed. After the vertex position is determined, incompatible tracks are removed and used to determine other vertices. Each vertex must have at least two tracks associated with it. This procedure is repeated until all tracks are associated with a vertex or until no additional vertex can be found from the remaining tracks. The vertex with the highest scalar sum of p_{T} of the associated tracks is selected as the primary vertex.

A new and improved primary vertex reconstruction algorithm was developed for Run 3. Primary vertex reconstruction for Run 2 was based on the iterative vertex finder (described above) which uses a single vertex fitter. For Run 3, an adaptive multi-vertex finder algorithm [111] was developed. This approach uses the global track pool to select tracks for new candidates — not just tracks that are incompatible with previous vertices. If the vertex candidate shares tracks with any previously fitted vertices, all of these vertices are fitted simultaneously.

7.4 Topological clusters

Upon reaching the calorimeter, particles interact with the detector material and deposit energy. Energy deposits in the calorimeters are grouped based on their topology to form *topo-clusters* [112] which are essential in the the reconstruction of physics objects such as electrons and photons. The formation of topo-clusters follows a sequence of seed and collect steps.

1. A topo-clusters begins with a calorimeter cell seed. The seed must have an energy deposit of at least four times the expected noise level.

2. Any adjacent cells with an energy of at least twice the noise level are added to the cluster. This process is repeated until no more cells can be added to the cluster.

3. To complete the topo-cluster, all remaining adjacent calorimeter cells are added irrepsective of their energy.

This process is referred to as 4-2-0 reconstruction, reflecting the energy requirements of the calorimeter cells. The formation of topo-clusters is most effective with a highly granular calorimeter like the one employed in the ATLAS detector.

7.5 Electron and photon reconstruction

The ECal cannot distinguish between electromagnetic showers originating from an electron or a photon. Energy deposits in the ECal, or topo-clusters, must be combined with tracking information from the ID to make the distinction. Photons do not have an electric charge and therefore do not leave a track in the ID, known as *unconverted photons*, unless they convert into an electron-positron pair, in which case they are referred to as *converted photons*.

A dynamic clustering algorithm [113] that exploits variable-sized clusters, termed *superclusters*, is used to reconstruct electrons and photons in the ATLAS detector. Within the central region of the ATLAS detector ($|\eta| < 2.47$), the electron and photon reconstruction procedure is as follows:

1. clusters of energy deposits in topologically connected cells of the ECal are reconstructed to form topo-clusters;
2. topo-clusters are matched to tracks in the ID and tracks are refitted to account for bremsstrahlung;
3. conversion vertices are reconstructed and matched with topo-clusters to identify converted photons;
4. superclusters are formed by merging topo-clusters; and
5. physics objects are built and their energies calibrated.

An electron is defined as an object consisting of a cluster and a matching track (or tracks). A converted photon is an object consisting of a cluster matched to a conversion vertex (or vertices). Conversely, an unconverted photon is an object consisting of a cluster that does not match a conversion vertex or electron track.

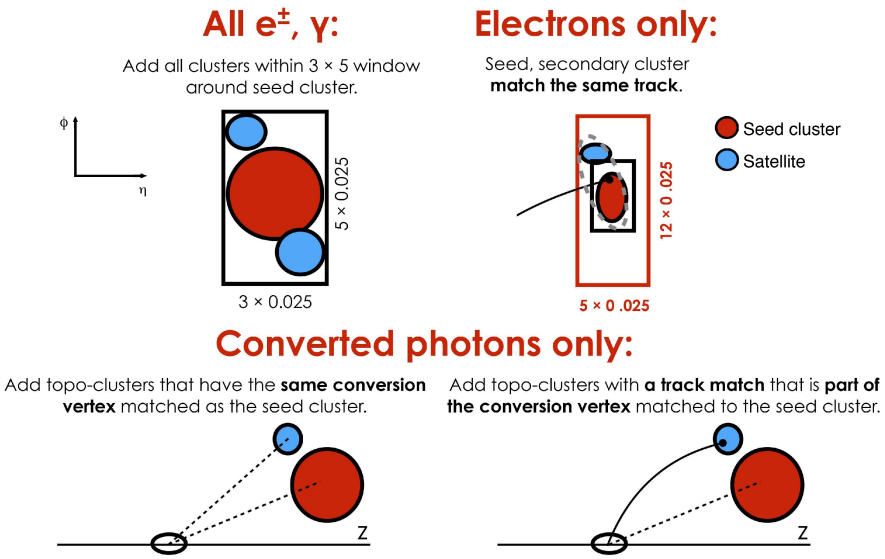

Figure 7.2 *Diagram of the superclustering algorithm for electrons and photons. Seed clusters are shown in red and satellite clusters in blue. Figure from Ref. [114].*

7.5.1 Supercluster reconstruction

After the track-matching is performed, a supercluster-building algorithm [113] is used to reconstruct electron and photon superclusters. Seed candidates are formed from topo-clusters which are sorted by p_{T} such that the remaining clusters have lower p_{T} than the seed. An electron supercluster seed is formed from a topo-cluster with an energy above 1 GeV and a matching track with at least four silicon hits. A photon supercluster seed is formed from a topo-cluster with an energy above 1.5 GeV and no track requirements. Remaining topo-clusters are identified as satellite cluster candidates, emerging from bremsstrahlung radiation or topo-cluster splitting. Satellite clusters must have a lower p_{T} than the seed cluster and lie within a window of $\Delta\eta \times \Delta\phi = 0.075 \times 0.125$ of the seed cluster barycentre — the geometric centre of the clusters. To form the final supercluster, satellite clusters are then added to the seed cluster candidates. Figure 7.2 illustrates the supercluster reconstruction algorithm for electrons and photons. For electrons, an additional satellite cluster search is performed in an extended window.

7.5.2 Photon identification

Whilst the procedure described above is effective at reconstructing *prompt photons* from the hard-scatter process, it can also reconstruct background objects

such as jets that are misidentified as photons. The main source of fake photons originate from the decay of neutral hadrons in jets or QCD jets that have high energy deposits in the ECal. The photon identification algorithm [115] is designed to efficiently select isolated, prompt photons and reject background from hadronic jets. The algorithm is constructed from one-dimensional selection criteria using properties of the shower shape, which are related to the energy deposition of the photon candidate in the calorimeters. There are three working points for photon identification: *loose*, *medium* and *tight*.

The loose working point is used in the photon preselection with a nominal efficiency of above 98% for prompt photons with $p_{\mathrm{T}} > 30\,\mathrm{GeV}$. It considers the lateral and longitudinal shape of the electromagnetic shower in the second layer of the calorimeter and the fraction of energy deposited in the HCal. Compared to background photons from jets, prompt photons originating from the $H \to \gamma\gamma$ event typically produce narrower energy deposits in the ECal with small leakage to the HCal.

The tight working point is used in the offline analysis of photon and diphoton events. Based on the same information as the loose working point, the tight selection imposes more stringent requirements on the shower shape variables. Moreover, additional information from the finely-segmented first layer of the ECal is included, such as the ratio of energy in the first layer to the total energy of the cluster. The criteria are separately optimised for converted photons and unconverted photons. The efficiency of the tight identification criteria varies with transverse energy, E_{T}: 84% (85%) at $E_{\mathrm{T}} = 25\,\mathrm{GeV}$ and 94% (98%) at $E_{\mathrm{T}} = 100\,\mathrm{GeV}$ for unconverted (converted) photons.

Prompt photons should not be accompanied by other energy deposits in the calorimeter or tracks in the ID. To further reject hadronic jet background, photon candidates are therefore required to be *isolated* from any other significant activity in the calorimeter and tracking detector. Surviving photon candidates are required to be isolated in the ID known as track-based isolation, and calorimeters, referred to as calorimeter-based isolation. Photon isolation is based on a cone of radius $\Delta R = \sqrt{(\Delta\eta)^2 + (\Delta\phi)^2} = 0.2$ around the photon candidate. To determine the track-based isolation, only tracks with $p_{\mathrm{T}} > 1\,\mathrm{GeV}$ that originate from the primary vertex are considered. The p_{T} of all tracks within a cone of $\Delta R = 0.2$ around the photon candidate is summed. Track-based isolation requires the p_{T}-

sum to be less than 5% of the photon p_{T}:

$$\frac{\sum p_{\mathrm{T}}^{\Delta R=0.2}}{p_{\mathrm{T}}^{\gamma}} < 0.05. \tag{7.1}$$

To determine calorimeter-based isolation, the sum of the E_{T} of all positive energy topological clusters within a cone of $\Delta R = 0.2$ around the photon candidate is used. Calorimeter-based isolation requires the E_{T} sum to be less than 6.5% of the photon E_{T}:

$$\frac{\sum E_{\mathrm{T}}^{\Delta R=0.2}}{E_{\mathrm{T}}^{\gamma}} < 0.065. \tag{7.2}$$

Both isolation requirements are required to help distinguish prompt photons from backgrounds that appear as neutral energy deposits in the calorimeter or tracks in the ID.

The photon reconstruction efficiency in the ATLAS detector is high, around 96% for prompt photons with $p_{\mathrm{T}} > 25\,\mathrm{GeV}$ [116]. A lower efficiency is observed for converted photons, in the order of 70% [114].

7.5.3 Diphoton vertex

The default ATLAS definition of the primary vertex relies on charged particle tracks. Since photons typically do not leave tracks in the ID, this method is not well suited for events where photons are among the most energetic objects [117]. Diphoton analyses, therefore, apply a custom selection of the primary vertex.

A neural network algorithm [116, 117] was designed to combine the two approaches used to identify the interaction point:

1. summing the transverse momenta of tracks associated with the vertex (see Section 7.3); and
2. exploiting the longitudinal segmentation of the ECal (a technique referred to as *pointing* [79]) to determine the trajectory of each photon candidate.

Using the photon pointing method, the vertex position along the beam axis (defined as z_{common}) is obtained by combining the trajectories of both photons, measured using the longitudinal segmentation the calorimeter.

The neural network was trained to distinguish between the hard-scatter vertex of

ggF events and vertices from pile-up. Furthermore, the algorithm was trained to distinguish between three cases: at least one photon converting into an electron-positron pair resulting in tracks associated to a reconstructed primary vertex; at least one converted photon with tracks containing hits in the silicon detectors; and both photons unconverted or associated to tracks containing only hits in the TRT.

The following variables were used as inputs to the algorithm:

- $(z_{\text{common}} - z_{\text{vertex}})/\sigma_z$ where z_{vertex} is the primary vertex position and z_{common} is identified from calorimeter pointing;
- $\log_{10}(\sum p_{\text{T}})$ and $\log_{10}(\sum p_{\text{T}}^2)$ where the sum of p_{T} is over all tracks associated with the vertex; and
- $\Delta\phi(\gamma\gamma, \text{vertex})$ is the angular separation between the diphoton system and the system defined by the vector sum of the track momenta.

The diphoton vertex algorithm has a selection efficiency of 71.4% for ggF compared to 52.2% for the default primary vertex selection [118].

7.6 Muon reconstruction

For muon identification, the main signature exploited in the ATLAS detector is that of a minimally-ionising particle, indicated by the presence of a track in the MS or characteristic energy deposits in the calorimeters. Muon reconstruction [119, 120] relies primarily on information from the ID and MS tracking systems. On occasion, information from the calorimeter subsystems is also used to determine track parameters, account for cases of large energy loss in the calorimeters and for MS-independent tagging of tracks in the ID as muon candidates.

Standalone muon reconstruction

Reconstruction of tracks in the MS begins with the identification of short, straight-line *track segments* reconstructed from hits within the individual MS subsystems. Hits in the MDTs are combined to form local track segments

identified using a Hough transform [121], which searches for hits aligned on a trajectory in the bending plane of the ATLAS detector. Segments in the MDTs are reconstructed by performing a straight-line fit to the hits found in each layer. Hits in the RPCs and TGCs measure coordinates orthogonal to the bending plane. Segments in the CSCs are built using a separate combinatorial search in the η and ϕ planes of the detector.

Preliminary track candidates are formed by combining track segments within different components of the MS. A loose requirement on the interaction point and a parabolic trajectory consistent with a first-order approximation of the muon bending in the magnetic field is used. A global χ^2 fit of the muon trajectory through the magnetic field is performed, accounting for possible interactions in the detector material and misalignments between different detector chambers. Outlier hits are removed and hits along the trajectory that were not originally assigned to the track candidate are added. The track is then refitted to account for the additional hits. Tracks that share a large fraction of hits with higher-quality tracks are removed. The final set of tracks is refitted with the loose interaction point constraint, accounting for energy loss in the calorimeters, and is extrapolated back to the beam line.

Global muon reconstruction

Global muon reconstruction is performed using information from the ID, MS and calorimeter systems. There are four different muon types depending on the presence or absence of MS and ID signatures: combined, segment-tagged, standalone and calorimeter-tagged muons.

- *Combined muons* have both an ID and MS track with a good match between the two yielding the best possible precision on the measurement of muon properties. These are the only muon type used in physics analyses.
- *Segment-tagged muons* have an ID track and segment tracks within layers of the MS which match well. There is, however, no global MS track. This occurs when a muon has low p_{T} or is in a region of the detector with poor MS coverage.
- *Standalone muons* do not have an ID track but do have a global MS track. Typically, this happens within $2.5 < |\eta| < 2.7$ where there is no ID coverage.

- *Calorimeter-tagged muons* have an ID track but no MS track. Additionally, there is an energy deposit in the calorimeter that matches the ID track and is consistent with a minimally-ionising particle.

7.7 Jet reconstruction

Free partons are not predicted and have not been observed in nature. Partons produced in pp collisions therefore undergo hadronisation. Hadronisation is the process by which parton collections form a set of colour-singlet hadrons, known as mesons and baryons. These hadrons typically form well-collimated jets of particles, measurable in the silicon tracker and hadronic calorimeter. Since the radiation from parton showering is considered to be approximately collinear to the original hard particle, a single jet is expected for every sufficiently hard parton. Procedures for defining jets are known as jet reconstruction algorithms. A jet algorithm is a systematic procedure used to cluster the final-state hadrons into jets.

The main jet clustering algorithm used by ATLAS is the anti-k_t algorithm [122] with a radius parameter of $R = 0.4$. The anti-k_t algorithm uses topo-cluster information as input. Topo-clusters are calibrated to match the energy deposits of electromagnetic particles in the calorimeter, referred to as the electromagnetic scale. A calibration factor, known as the local cluster weighting [123], can be applied to modify the energy of hadronic topo-clusters. To restore the energy scale of jets to particle level, a jet energy scale [124] calibration is applied to correct for experimental effects.

The particle-flow algorithm [125] combined tracking and calorimeter information to reconstruct jets with better energy and angular resolution. Tracks from the ID are matched to topo-clusters to form signals representing individual particles. Clusters that are not matched to any track are considered to arise from neutral particles. The final list of charged tracks and neutral clusters is used as input to the anti-k_t algorithm. This approach improves jet reconstruction and supression of jets due to pile-up.

7.7.1 Jet Vertex Tagger

High pile-up conditions at the LHC make identification of jets from the hard process a challenge. To surpress jets coming from pile-up interactions, a Jet Vertex Tagger (JVT) [126] algorithm is used.

The JVT is constructed using two variables: a modified version of the Jet Vertex Fraction (JVF) and $R_{p_{\mathrm{T}}}$. The JVF is a variable used in ATLAS to identify the primary vertex from which the jet originated. Applying a cut on the JVF can help remove jets that are not associated with the hard-scatter primary vertex. For a given jet_i, the JVF with respect to the primary vertex, PV_j, is defined as

$$\mathrm{JVF}(\mathrm{jet}_i, \mathrm{PV}_j) = \frac{\sum_m p_{\mathrm{T}}(\mathrm{track}_m^{\mathrm{jet}_i}, \mathrm{PV}_j)}{\sum_n \sum_l p_{\mathrm{T}}(\mathrm{track}_l^{\mathrm{jet}_i}, \mathrm{PV}_n)}, \tag{7.3}$$

where the following apply: m runs over all tracks originating from PV_j matched to jet_i; n runs over all primary vertices in the event; and l runs over all tracks originating from PV_n matched to jet_i. The variable $R_{p_{\mathrm{T}}}$ is defined as

$$R_{p_{\mathrm{T}}} = \frac{\sum_k p_{\mathrm{T},k}^{\mathrm{track}}(\mathrm{PV}_0)}{p_{\mathrm{T}}^{\mathrm{jet}}}, \tag{7.4}$$

where k runs over all tracks associated with the jet originating from the hard-scatter vertex, PV_0, and $p_{\mathrm{T}}^{\mathrm{jet}}$ is the fully calibrated jet p_{T} which includes pile-up subtraction. Figure 7.3 compares the distributions of the modified JVF and $R_{p_{\mathrm{T}}}$ for pile-up and hard-scatter jets.

For early Run 3 analyses looking at 2022 data, a Jet Vertex Tagger (JVT) multivariate discriminant is applied to jets with $p_{\mathrm{T}} < 60\,\mathrm{GeV}$ to distinguish those originating from the hard process.

More recently for Run 3, a neutral network JVT discriminant is applied [127] and the JVT cut is now dynamic depending on the p_{T} and η of the jet.

7.7.2 Jet flavour tagging

Jet flavour tagging [128] works on the principle that hadrons containing bottom and charm quarks have measureable lifetimes. Input jet kinematics, impact parameter and secondary vertex information is used to train a multivariate

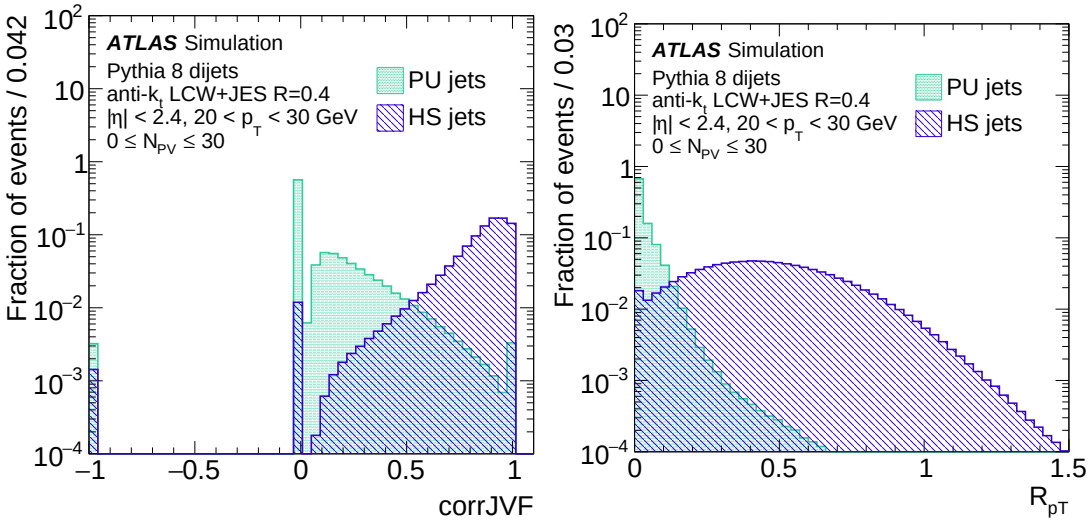

(a) *Modified JVF* **(b)** R_{p_T}

Figure 7.3 *Distribution of (a) modified Jet Vertex Fraction (JVF), referred to as corrJVF, and (b) R_{p_T} for pile-up (PU) and hard-scatter (HS) jets with $20 < p_T < 30\,\text{GeV}$. Figures from Ref. [126].*

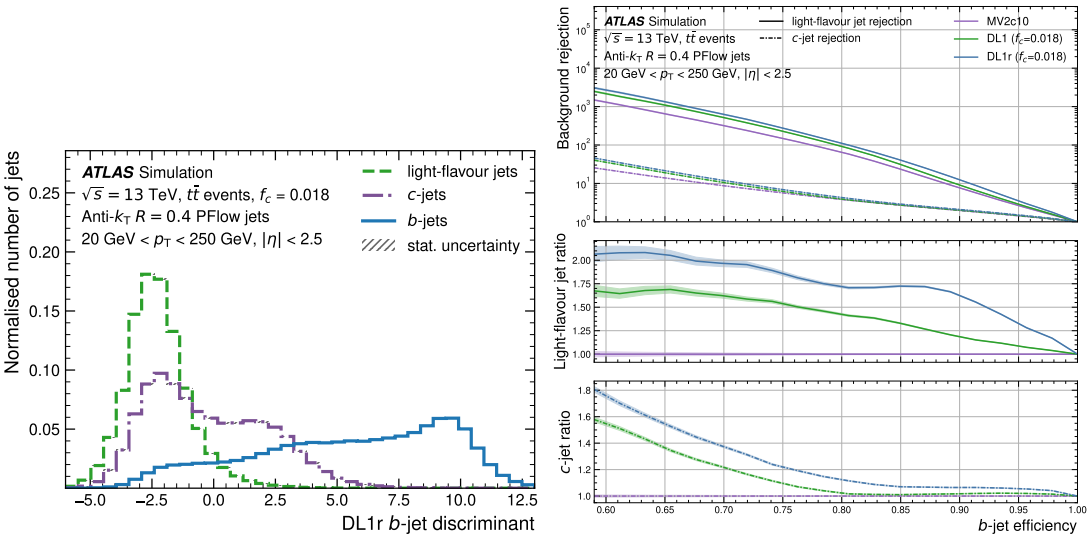

(a) *b-jet discriminant* **(b)** *Light-flavour and c-jet rejection*

Figure 7.4 *(a) Distribution of the outputs from the DL1r b-tagging algorithm for b-jets, c-jets and light-flavour jets in $t\bar{t}$ simulated events. (b) Light-flavour and c-jet rejection factors as a function of b-tagging efficiency for different high-level tagging algorithms. Figures from Ref. [128].*

neural network algorithm, `DL1r`, to provide the following discriminant outputs: b-probability, c-probability and light-flavour probability. The probabilities are combined into a b-tagging and c-tagging score used to identify jets originating from bottom and charm quarks respectively.

Figure 7.4a shows the distribution of the b-tagging discriminant for b-jets, c-jets and light-flavour jets. Furthermore, Figure 7.4b shows the light-flavour jet and c-jet rejection factors as a function of b-tagging efficiency for different high-level tagging algorithms. The `DL1r` algorithm is used in the Run 3 $H \to \gamma\gamma$ cross-section analysis with an efficiency of 70%.

7.8 Missing transverse energy

Since protons collide head-on at the interaction point, the total transverse momentum of the system is zero. The sum of the transverse momentum of all particles produced in the collision should therefore be zero. Missing Transverse Energy (MET) [129], $E_{\mathrm{T}}^{\mathrm{miss}}$, is an essential observable for the ATLAS Experiment which serves as a proxy for the transverse momentum carried by undetected particles produced in pp collisions. In the SM, MET typically serves as a proxy for any neutrinos produced in an event.

Applying conservation of momentum, MET is calculated by balancing the transverse momentum observed in the detector. MET has two components: the *hard component* refers to the selected hard objects in the event, such as electrons, muons, photons and jets; and the *soft component* refers to any remaining low p_{T} particles in the event estimated from tracks that are matched to the diphoton primary vertex but not associated with any physics object. MET is therefore defined as

$$\begin{aligned}\vec{E}_{\mathrm{T}}^{\,\mathrm{miss}} &= \left(E_x^{\mathrm{miss}}, E_y^{\mathrm{miss}}\right) \\ &= -\Bigg(\underbrace{\sum_{\substack{\text{selected}\\ \text{leptons}}} \vec{p}_{\mathrm{T}}^{\,e,\mu,\tau} + \sum_{\substack{\text{selected}\\ \text{photons}}} \vec{p}_{\mathrm{T}}^{\,\gamma} + \sum_{\substack{\text{selected}\\ \text{jets}}} \vec{p}_{\mathrm{T}}^{\,j}}_{\text{hard term}} + \underbrace{\sum_{\substack{\text{unused}\\ \text{tracks}}} \vec{p}_{\mathrm{T}}^{\,\mathrm{track}}}_{\text{soft term}} \Bigg).\end{aligned} \tag{7.5}$$

Chapter 8

$H \to \gamma\gamma$ cross-section measurements

In this chapter, I introduce the ATLAS Run 2 and Run 3 $H \to \gamma\gamma$ cross-section analyses presented in Ref. [7] and Ref. [118] respectively. I focus on techniques deployed in these analyses, which are referenced in my thesis work, including: diphoton event selection; event selection for cross-section measurements targeting the main Higgs production modes (ggF, VBF, VH and $t\bar{t}H$); Higgs signal invariant mass modelling; and systematic uncertainties of the cross-section measurements. Finally, I summarise the Yukawa interpretation procedure used in the Run 2 analysis to set limits on the bottom and charm quark Yukawa couplings which I build upon in my thesis work.

8.1 Run 2 and Run 3 datasets

This chapter describes two $H \to \gamma\gamma$ cross-section measurements. The Run 2 measurement presented in Ref. [7] was performed with the full 139 fb^{-1} of pp collision data recorded at a centre-of-mass energy of $\sqrt{s} = 13\,\text{TeV}$. The early Run 3 measurement presented in Ref. [118] was performed with the first 31.4 fb^{-1} of pp collision data recorded at a centre-of-mass energy of $\sqrt{s} = 13.6\,\text{TeV}$.

8.2 Event selection

For the $H \to \gamma\gamma$ event selection, an initial preselection requires events to have at least two photon candidates, with transverse energy $E_\text{T} > 25\,\text{GeV}$, satisfying the loose identification criteria detailed in Section 7.5.2. For events with more than two photon candidates, the two photons with the highest E_T are selected to form the diphoton system.

The final event is selected if the leading and subleading E_T photon candidates satisfy $E_T/m_{\gamma\gamma} > 0.35$ and 0.25 respectively. Kinematic cuts are applied to ensure photons are well-reconstructed within the ECal. To ensure signal events are retained for a boosted Higgs boson, asymmetric cuts are applied to the photon candidates.

The photon candidates must also meet the tight identification criteria and the calorimeter and track-based isolation requirements detailed in Section 7.5.2, designed to suppress background contributions from misidentified jets and non-prompt photons.

Finally, the invariant mass of the diphoton system must be within the range $105 < m_{\gamma\gamma} < 160\,\text{GeV}$. Focusing on the invariant mass region around the Higgs boson mass, this selection allows for a narrow signal peak on top of the continuum background.

8.2.1 Selection of jets, leptons and E_T^miss objects

Jets (including b-jets), leptons and E_T^miss objects are used in the cross-section analysis to target the main Higgs boson production modes.

Jets

As detailed in Section 7.7, jets are reconstructed using the anti-k_t algorithm with a radius parameter of $R = 0.4$. The inputs come from the particle-flow algorithm which combines information from the calorimeters and the ID. Jets must satisfy $p_{\mathrm{T}} > 25\,\mathrm{GeV}$ and $|y| < 4.5$. To suppress jets originating from pile-up, the JVT discriminant is applied to jets with $p_{\mathrm{T}} < 60\,\mathrm{GeV}$ and $|\eta| < 2.4$.

Jets with $|\eta| < 2.4$ containing b-hadrons (b-jets) of $p_{\mathrm{T}} > 5\,\mathrm{GeV}$ are identified using the `DL1r` b-tagging algorithm, introduced in Section 7.7.2, with the 70% efficiency working point.

Leptons

Reconstructed from topo-clusters (see Section 7.5), electron candidates are required to satisfy $p_{\mathrm{T}} > 15\,\mathrm{GeV}$ and $|\eta| < 2.47$, excluding the transition region $1.37 < |\eta| < 1.52$. Furthermore, they must pass the medium identification requirements and the isolation requirements based on the calorimeter and track information detailed in Ref. [114].

Muons candidates, reconstructed from tracks in the ID and MS (see Section 7.6), must satisfy $p_{\mathrm{T}} > 15\,\mathrm{GeV}$ and $|\eta| < 2.7$. Additionally, muons are selected using the medium identification requirements and must also satisfy the calorimeter and track-based isolation requirements detailed in Ref. [120].

Missing transverse energy

$E_{\mathrm{T}}^{\mathrm{miss}}$ is calculated as the negative vector sum of the transverse momenta of all reconstructed physics objects in the event as described in Section 7.8.

8.2.2 Higgs boson production modes

Subregions of phase space are defined to target the main Higgs production modes using the following selection criteria:

- **VBF-enhanced**: events with at least two jets where the leading and subleading jets have a large invariant mass, $m_{jj} \geq 600\,\mathrm{GeV}$, and large

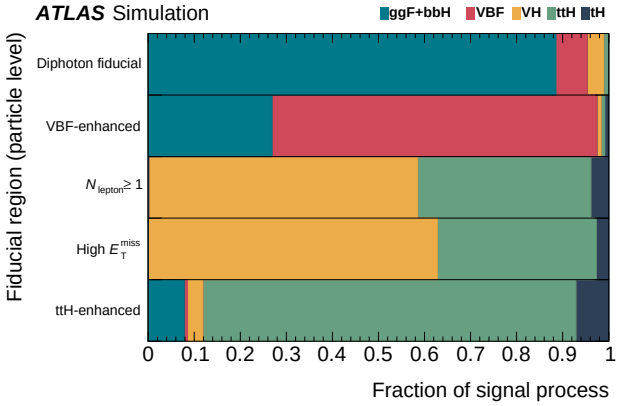

Figure 8.1 *Composition of Higgs boson production modes in the fiducial regions. Figure from Ref. [7].*

rapidity separation, $|\Delta y_{jj}| \geq 3.5$. This subregion exploits the two forward, high-energy jets in the VBF experimental signature.

- $\boldsymbol{N_{\text{lepton}} \geq 1}$: events with at least one charged lepton (electron or muon) with transverse momentum $p_{\text{T}}^{l} > 15\,\text{GeV}$. This subregion exploits the experimental signature of the leptonic W boson decay in VH and $t\bar{t}H$ production.

- **High** $\boldsymbol{E_{\text{T}}^{\text{miss}}}$: events with a large MET, $E_{\text{T}}^{\text{miss}} > 80\,\text{GeV}$, and diphoton transverse momentum, $p_{\text{T}}^{\gamma\gamma} > 80\,\text{GeV}$. This subregion region exploits the experimental signature of the neutrino in VH and $t\bar{t}H$ production modes.

- $\boldsymbol{t\bar{t}H}$**-enhanced**: events with at least one b-jet and either: (1) no leptons and at least four jets; or (2) at least one lepton and at least three jets. This subregion region exploits the experimental signature of the decay of the top quark, $t \to W^{+}b$, where the W boson decays leptonically or hadronically.

8.2.3 Fiducial phase space

The cross-section measurements are compared to theory predictions obtained at particle level before any detector effects are applied. Fiducial phase space is defined to closely match the detector level event selection requirements whilst aiming to minimise model dependence from any extrapolation. The requirements for the diphoton fiducial region are summarised in Table 8.1. Relative to full phase space, the signal acceptance of the diphoton fiducial region is 50%.

Table 8.1 *Requirements for the diphoton fiducial region. The isolation transverse energy is defined as the scalar sum of p_T for all stable charged particles (mean lifetime $c\tau > 10$ mm) with $p_T > 1\,\text{GeV}$ within a cone of $\Delta R = 0.2$ around the photon. Table from Ref. [118].*

Photons	
Leading (sub-leading) $p_{\text{T},\gamma}$	$p_{\text{T}}^{\gamma}/m_{\gamma\gamma} > 0.35\,(0.25)$
Pseudorapidity	$\lvert\eta\rvert < 2.37$ and outside $1.37 < \lvert\eta\rvert < 1.52$
Isolation ($\Delta R = 0.2$)	$E_{\text{T}}^{\text{iso}}/E_{\text{T}}^{\gamma} < 0.05$
Di-photon system	
Mass window	$105\,\text{GeV} < m_{\gamma\gamma} < 160\,\text{GeV}$

Fiducial subregions are defined to target the main Higgs boson production modes using the same selection criteria introduced in Section 8.2.2. The fiducial region requirements are particle level analogues of the reconstructed physics object requirements. For example, the high $E_{\text{T}}^{\text{miss}}$ fiducial region requires high momentum neutrinos. For each fiducial region, the expected composition of Higgs boson production modes is shown in Figure 8.1.

The early Run 3 measurement was performed using only the baseline diphoton fiducial region. The full Run 3 cross-section measurement, however, will include the additional fiducial subregions as seen in the Run 2 measurement.

8.3 Modelling of the invariant mass spectrum

The Higgs boson signal yield is extracted from an analytic fit to the diphoton mass, $m_{\gamma\gamma}$, spectrum in the range $105 < m_{\gamma\gamma} < 160\,\text{GeV}$.

8.3.1 Signal model

The Higgs boson signal can be observed in the invariant mass distribution of the diphoton system. Expected to follow a Breit-Wigner curve, the $m_{\gamma\gamma}$ distribution is a resonance peaking at the Higgs boson mass, m_H. Since the photon energies are measured with finite resolution, the observed distribution is smeared. The Higgs boson resonance is modelled using the double-sided Crystal Ball (DSCB) function. Figure 8.2 shows the shape DSCB function. The performance of the DSCB function in modelling the $m_{\gamma\gamma}$ distribution is validated in Chapter 10.

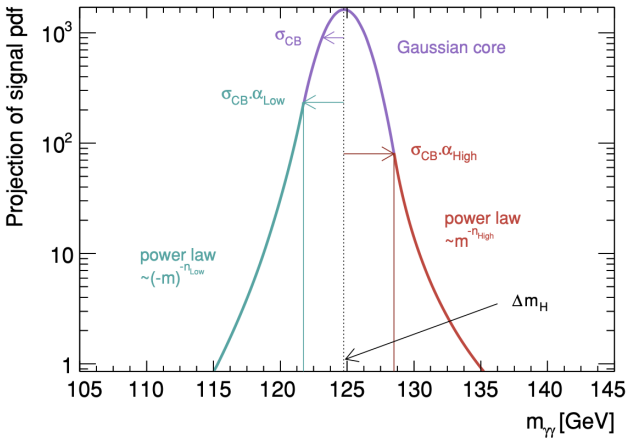

Figure 8.2 *Double-sided Crystal Ball function used to model the signal invariant mass distribution. Figure from Ref. [130].*

Characterised by a Gaussian central component and two power-law tails, there are six shape parameters that describe the DSCB function. The Gaussian component models the central part of the distribution where the signal peak is located. The Higgs mass and experimental resolution are mapped to the mean and width of the Gaussian component, denoted by μ_{CB} and σ_{CB} respectively. The independent power-law tails model the low- and high-mass tails of the distribution. The positions where the Gaussian core transitions to the power-law tails are denoted by α_{low} and α_{high}. Similarly, the exponents of the tails are denoted by n_{low} and n_{high}. The analytic form of the DSCB function [131] is given by

$$\mathrm{CB}(m_{\gamma\gamma}) = N \times \begin{cases} e^{-t^2/2} & \text{if } -\alpha_{low} \leq t \leq \alpha_{high} \\ e^{-\frac{1}{2}\alpha_{low}^2} \left[\frac{1}{R_{low}} \left(R_{low} - \alpha_{low} - t\right)\right]^{-n_{low}} & \text{if } t < -\alpha_{low} \\ e^{-\frac{1}{2}\alpha_{high}^2} \left[\frac{1}{R_{high}} \left(R_{high} - \alpha_{high} - t\right)\right]^{-n_{high}} & \text{if } t > \alpha_{high}, \end{cases}$$

where $t = (m_{\gamma\gamma} - \mu_{CB})/\sigma_{CB}$, $R_{low} = \alpha_{low}/n_{low}$ and $R_{high} = \alpha_{high}/n_{high}$. The shape parameters are determined by performing a fit to simulated $H \to \gamma\gamma$ decays. The normalisation factor, N, is determined in the fit to the data.

8.3.2 Background model and spurious signal

The main sources of background are the non-resonant production of prompt and isolated diphotons ($\gamma\gamma$) and the misidentification of hadronic jets as photons (γj, jj). The fraction contributed by each background component is measured in data using a two-dimensional double-sideband method detailed in Ref. [132]. From the early Run 3 analysis, the fraction of the three components is measured

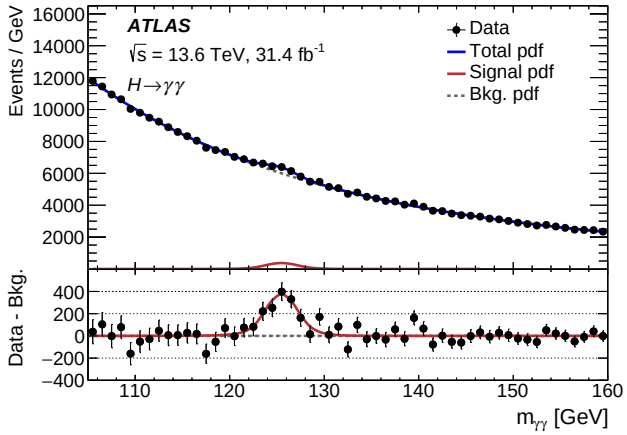

Figure 8.3 *Diphoton invariant mass spectrum within the $H \to \gamma\gamma$ fiducial region as observed for the early Run 3 data. The signal, background and total probability density functions are shown in the fit to the data. Figure from Ref. [118].*

to be $73.0 \pm 1.9\%$ for $\gamma\gamma$, $23.6 \pm 1.5\%$ for γj and $3.4 \pm 0.4\%$ for jj.

The sum of the background components is characterised by a smooth falling distribution and can be parameterised by an empirical function. Several functional forms for parameterisation of the $m_{\gamma\gamma}$ distribution are studied, including power-law functions, Bernstein polynomials and exponential functions of polynomials. The functional form used in both publications is an exponential function of a second-order polynomial in $m_{\gamma\gamma}$:

$$\mathcal{B}(m_{\gamma\gamma}; \alpha) = \exp\left(\alpha_1 + \alpha_2 m_{\gamma\gamma} + \alpha_3 m_{\gamma\gamma}^2\right). \tag{8.1}$$

The spurious signal yield is defined as the measured signal yield obtained in a signal-plus-background fit to the background-only template. The absolute value of the spurious signal yield is taken as the background modelling uncertainty.

8.4 Fit procedure

The $pp \to H \to \gamma\gamma$ fiducial cross-section is measured through an analytic fit to the $m_{\gamma\gamma}$ spectrum which combines the signal and background parameterisations, as shown in Figure 8.3. In the inclusive measurement, the measured signal yields are corrected to particle level using a correction factor derived from simulation. This factor accounts for both detector effects and contributions from signal events

outside the acceptance region.

The signal yield is obtained through a profile likelihood fit to the $m_{\gamma\gamma}$ spectrum. It is parameterised as

$$\begin{aligned} N_S &= \sigma_{\text{fid}} \times \mathcal{L} \times \mathcal{C}_{\mathcal{F}} \\ &= \{\sigma_{\text{tot}} \times \mathcal{B}_{\gamma\gamma} \times \mathcal{A}\} \times \mathcal{L} \times \mathcal{C}_{\mathcal{F}}, \end{aligned} \tag{8.2}$$

where $\mathcal{L}$ is the integrated luminosity, $\mathcal{C}_{\mathcal{F}}$ is the correction factor and σ_{fid} is the fiducial cross-section defined in terms of the total cross-section, σ_{tot}, branching ratio, $\mathcal{B}_{\gamma\gamma}$, and signal acceptance, $\mathcal{A}$. The correction factor is defined as the ratio of the number of signal events selected at detector level to the number of signal events selected at particle level, applying the selection criteria described in Section 8.2. The signal acceptance is the fraction of signal events passing the particle level fiducial selection described in Section 8.2.3. Derived inclusively assuming a SM ratio of all Higgs boson production modes, the correction factor derived from simulated signal samples is 71.6% in Ref. [118].

8.5 Systematic uncertainties

Several sources of uncertainty affect the $pp \to H \to \gamma\gamma$ fiducial cross-section measurement which can be broken down into two categories: uncertainties affecting the shape of the $m_{\gamma\gamma}$ signal and background distributions; and those impacting the detector and fiducial corrections to the measured signal yields. The uncertainty in the luminosity measurement also affects the measurement.

Sources of uncertainty impacting the modelling of the $m_{\gamma\gamma}$ signal are introduced from the energy scale and resolution of the photon. Uncertainties in the energy scale of the photon result in a shift of the peak position. Uncertainties in the energy resolution of the photon result in a broadening or narrowing of the signal peak. Detailed in Ref. [114], these uncertainties are estimated from $Z \to ee$ decays. Moreover, the uncertainty in the Higgs boson mass affects the peak position [29]. The spurious signal quantifies the associated systematic uncertainty with the choice of analytic function used to model the background distribution.

The experimental uncertainties are as follows: the efficiency of the photon trigger; the identification and isolation selections; the impact of the diphoton vertex selection; the estimation of the energy scale and resolution of the photon; and

Table 8.2 *Breakdown of the uncertainties in the Run 2 inclusive diphoton fiducial cross-section measurement. Table from Ref. [7].*

Source	Uncertainty [%]
Statistical uncertainty	7.2
Systematic uncertainties	6.0
Background modelling (spurious signal)	3.6
Photon energy scale & resolution	3.3
Photon selection efficiency	2.5
Luminosity	1.7
Pile-up modelling	1.3
Trigger efficiency	1.0
Theoretical modelling	0.4
Total	9.4

the modelling of pile-up.

The efficiency of the diphoton photon trigger is estimated with an uncertainty of about 2% using the bootstrap method detailed in Ref. [87]. The photon identification efficiency is measured using data-driven techniques, detailed in Ref. [114]. Moreover, the photon isolation efficiency is evaluated by varying track and calorimeter isolation scale factors. For the diphoton vertex selection, the algorithm efficiency is computed in both data and simulation; the difference between the two is evaluated using $Z \to ee$ events. Furthermore, changes to the photon energy scale and resolution result in the migration of events in and out of the fiducial region thus affecting the fiducial cross-section measurement. Finally, modelling of pile-up is derived by reweighting simulated events to match the observed pile-up distribution in data [133].

Theoretical uncertainties arise from modelling the Higgs boson signal with simulated event samples, including the matrix element generator and modelling the parton shower and hadronisation. A signal composition uncertainty is estimated by varying the production cross-sections within the measured uncertainties as detailed in Ref. [3].

The uncertainties in the Run 2 $H \to \gamma\gamma$ cross-section measurement are summarised in Table 8.2. The uncertainties for the early Run 3 measurement are extrapolated from Run 2 and so contain additional uncertainties to account for the change in conditions at the LHC. Given the additional uncertainties in extrapolating, the Run 2 uncertainties are more representative of the uncertainties associated with a full Run 3 dataset.

8.6 Fiducial cross-section results

For Run 2, the value of the fiducial cross-section at 13 TeV extracted from the fit to the $m_{\gamma\gamma}$ spectrum is

$$\sigma_{\text{fid}} = 67 \pm 5\,(\text{stat.}) \pm 4\,(\text{syst.})\,\text{fb} = 67 \pm 6\,\text{fb}, \tag{8.3}$$

which is in agreement with the SM prediction of $\sigma_{\text{fid}} = 64 \pm 4\,\text{fb}$ [134].

For the early Run 3 publication, the value of the fiducial cross-section at 13.6 TeV extracted from the fit to the $m_{\gamma\gamma}$ spectrum is

$$\sigma_{\text{fid}} = 76 \pm 11\,(\text{stat.})^{+9}_{-7}\,(\text{syst.})\,\text{fb} = 76^{+14}_{-13}\,\text{fb}, \tag{8.4}$$

also in agreement with the SM prediction of $\sigma_{\text{fid}} = 67.6 \pm 3.7\,\text{fb}$.

8.7 Yukawa interpretation

The Yukawa interpretation in the Run 2 $H \to \gamma\gamma$ cross-section publication in Ref. [7] set limits on the bottom and charm quark Yukawa couplings using the Higgs boson p_{T} spectrum. As discussed in Section 3.7.3, variations in the coupling strength modifiers κ_b and κ_c impact both the shape and normalisation of the $p_{\text{T},\gamma\gamma}$ spectrum.

Modifications in κ_b and κ_c impact the ggF and $q\bar{q} \to H$ production modes. Introduced in Section 3.2.2, the state-of-the-art cross-section values for $b\bar{b} \to H$ (Equation 3.3) and $c\bar{c} \to H$ (Equation 3.4) production were used in this publication. Furthermore, the parameterisation of the $pp \to H$ cross-section as a function of κ_b and κ_c is presented in Equation 3.11.

The $H \to \gamma\gamma$ branching ratio is also affected by changes in the $H \to \gamma\gamma$ partial width and the total Higgs boson decay width, which is primarily affected by modifications in the $H \to b\bar{b}$ and $H \to c\bar{c}$ decay widths. Variations in the $H \to \gamma\gamma$ branching ratio with κ_b and κ_c were estimated using HDECAY [135, 136] for this publication. The parameterisation is summarised in Table 3.4. All Higgs boson couplings, except κ_b and κ_c, are set to their SM value with $\kappa = 1$.

Two different fitting strategies were employed to extract limits on κ_b and κ_c, each

Table 8.3 *Observed and expected constraints at 95% confidence level on the bottom and charm Yukawa coupling modifiers, κ_b and κ_c respectively. The limits on a given coupling are extracted whilst fixing the other coupling to the SM value. Confidence intervals are presented for both the shape-only and shape+normalisation strategies. Table adapted from Ref. [7].*

Fit set-up	κ	Observed 95% CL	Expected 95% CL
Shape-only	κ_c	$[-12.6,\ 18.3]$	$[-10.1,\ 17.3]$
	κ_b	$[-3.5,\ 10.3]$	$[-2.5,\ 8.1]$
Shape+norm	κ_c	$[-2.5,\ 2.3]$	$[-3.0,\ 3.1]$
	κ_b	$[-1.1, -0.8] \cup [0.8,\ 1.1]$	$[-1.2, -0.9] \cup [0.8,\ 1.2]$

with an increasing level of model dependence:

1. **shape-only:** considers the shape of the measured $p_{\mathrm{T},\gamma\gamma}$ spectrum; and
2. **shape+normalisation:** accounts for both shape and normalisation changes in the measured $p_{\mathrm{T},\gamma\gamma}$ spectrum due to variations in the cross-section and branching ratio.

For the interpretation, the cross-section is parameterised as a function of κ_b and κ_c in each bin of $p_{\mathrm{T},\gamma\gamma}$. To extract limits on κ_b and κ_c, the statistical interpretation of the $p_{\mathrm{T},\gamma\gamma}$ distribution is performed with the profile likelihood method. The complete measurement likelihood for the $p_{\mathrm{T},\gamma\gamma}$ distribution is compared with the predictions which are parameterised as a function of κ_b and κ_c. Finally, the limits at 95% confidence level are determined using a test statistic based on the ratio of profile likelihoods [137]. The measured differential cross-section is used within the $p_{\mathrm{T},\gamma\gamma}$ range up to 200 GeV where it is most sensitive to variations of κ_b and κ_c. All other Higgs boson couplings are set to their SM value with $\kappa = 1$.

Table 8.3 summarises the observed and expected constraints on κ_b and κ_c at 95% confidence level for the two fitting strategies. Stricter limits are obtained when considering the shape+normalisation effects of the $p_{\mathrm{T},\gamma\gamma}$ distribution. As the dominant effect, the normalisation of the $p_{\mathrm{T},\gamma\gamma}$ spectrum is more sensitive to variations in the Yukawa couplings than the shape.

Figure 8.4 shows the Run 2 data compared to predictions of κ_c at 95% confidence level for the two fitting strategies. The two-dimensional limits in Figure 8.5 are extracted by varying κ_b and κ_c simultaneously. For the shape+normalisation fitting strategy, the observed limits on κ_b are stronger than those on κ_c. Since

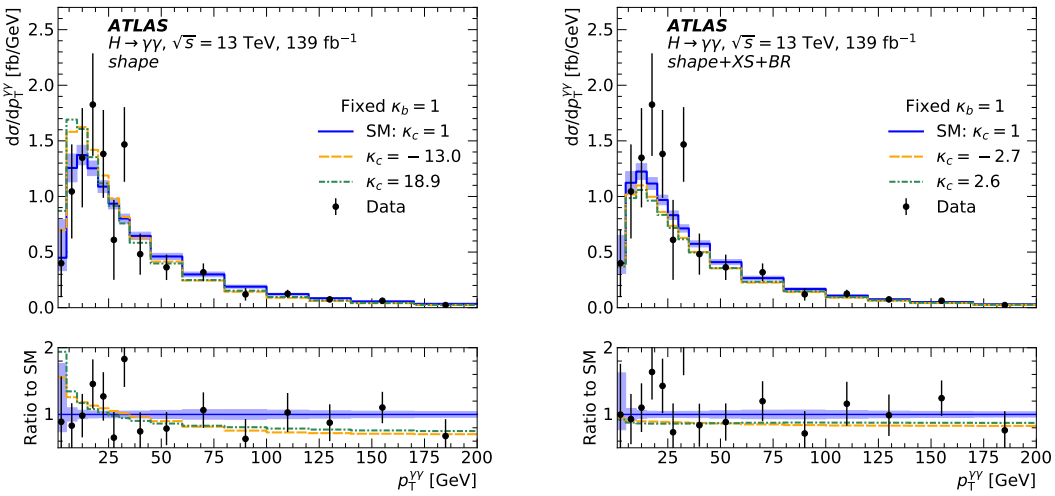

(a) *shape-only, κ_c template* **(b)** *shape+normalisation, κ_c template*

Figure 8.4 *Observed fiducial differential cross-section times branching ratio for the diphoton transverse momentum distribution, $p_{T,\gamma\gamma}$, using different values of κ_c corresponding to the 95% confidence level. The green and orange lines correspond to the upper and lower limits respectively. Two different fitting strategies were used: (a) shape-only and (b) shape+normalisation (shape+XS+BR). Figures from Ref. [7].*

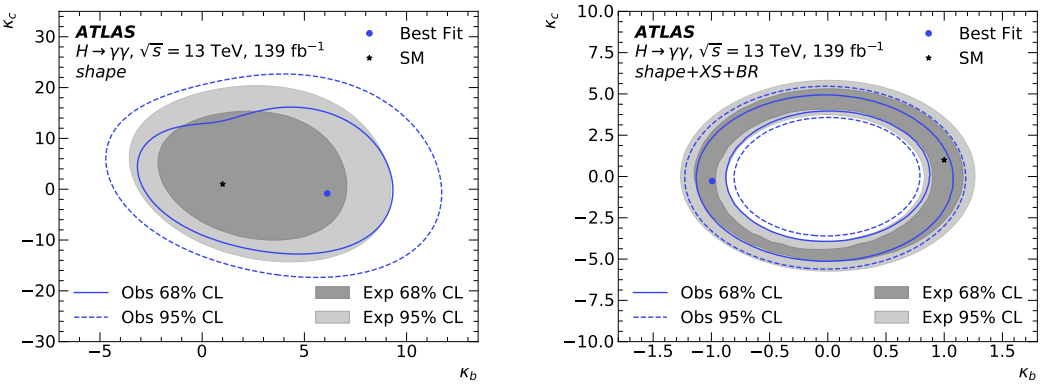

(a) *shape-only limits* **(b)** *shape+normalisation limits*

Figure 8.5 *Observed and expected two-dimensional limits on κ_b and κ_c when considering modifications of (a) the shape and (b) shape+normalisation. Limits are presented at both 95% and 68% confidence levels. Figures from Ref. [7].*

$b\bar{b} \to H$ production and the κ_b terms in the ggF cross-section are larger compared to the corresponding κ_c terms, the observed limits on κ_b are stronger than those on κ_c. The values on κ_b around zero can therefore be excluded which leads to the doughnut shape of the non-excluded parameter region in Figure 8.5b.

Furthermore, for the shape+normalisation strategy, more stringent constraints on κ_c are achieved through the $H \to \gamma\gamma$ measurement compared to the direct $H \to c\bar{c}$ search presented in Table 3.5.

Chapter 9

Data validation

In this chapter, I focus on the validation of simulated and experimental data used in the $H \to \gamma\gamma$ analysis. This study is essential to ensure the simulated events used to develop an analysis accurately model the $H \to \gamma\gamma$ signal and background processes. This thesis uses the combined data taken in 2022 and 2023 which has not yet been used in ATLAS publications. The software used to analyse this dataset, and its corresponding simulated samples, has been developed during my thesis and its performance not yet validated for the $H \to \gamma\gamma$ analyses. The 2022 data and software have already been validated and used in a publication, making them a reliable reference in this thesis.

The chapter begins with a discussion of the datasets used in this thesis. A validation study of simulated ggF events is presented, comparing different software versions developed for the $H \to \gamma\gamma$ analysis. This validation study was part of my contribution to the $H \to \gamma\gamma$ cross-section analysis and so validation of photons and additional objects, such as jets, was performed. Finally, I discuss the validation of the data control regions to assess how well the $\gamma\gamma$+jets sample models the background.

9.1 Datasets

9.1.1 Experimental data

The analysis in this thesis is performed on the 2022 and 2023 Run 3 *pp* collision data collected by the ATLAS Experiment at the LHC. At a center-of-mass energy of 13.6 TeV, $31.4\,\text{fb}^{-1}$ and $27.2\,\text{fb}^{-1}$ of integrated luminosity were recorded in 2022 and 2023 respectively. The uncertainty on the integrated luminosity is 2.2% [138] and 2.0% [139] for 2022 and 2023 data-taking periods respectively. A total luminosity of $58.6\,\text{fb}^{-1}$ is used for the analysis with a combined uncertainty of 2.0%.

Table 9.1 *Selection cutflow of the $H \to \gamma\gamma$ measurement using 2022 and 2023 Run 3 datasets corresponding to $31.4\,\text{fb}^{-1}$ and $27.2\,\text{fb}^{-1}$ of integrated luminosity respectively. Run 3 pp collision data is recorded at a centre-of-mass energy of 13.6 TeV. Rows highlighted in orange indicate significant differences in the cutflow between the two datasets.*

Selection step	2022 (31.4 fb^{-1})		2023 (27.2 fb^{-1})	
	Events	Rel. eff.	Events	Rel. eff.
All events	156635104	100.0%	158344208	100.0%
No duplicates	156635104	100.0%	158344128	100.0%
Good runs list	152701968	97.5%	149712048	94.5%
Pass trigger	136773040	89.6%	125093752	83.6%
Detector data quality	136763968	100.0%	125085168	100.0%
Has primary vertex	136763904	100.0%	125085168	100.0%
2 loose photons	14865821	10.9%	14651988	11.7%
e-γ ambiguity	14865821	100.0%	14651988	100.0%
Trigger match	10427911	70.1%	9027158	61.6%
Tight identification	3581034	34.3%	3062436	33.9%
Isolation	1502712	42.0%	1350657	44.1%
Rel. p_{T} cuts	1301128	86.6%	1166364	86.4%
$m_{\gamma\gamma} \in$ [105,160] GeV	307996	23.7%	263095	22.6%
Events per fb^{-1}	9809 ± 99		9673 ± 98	

Table 9.1 shows the event selection cutflow of the $H \to \gamma\gamma$ measurement for the 2022 and 2023 datasets. The full event selection is described in Chapter 8. Only events that pass the single or diphoton triggers described in Chapter 5 (Table 5.1) are used. The main takeaway from Table 9.1 is an issue with the trigger performance for the 2023 dataset. The lower efficiency in the *pass trigger* and *trigger match* steps for 2023 data taking is unexpected.

9.1.2 Simulated data

Simulated data is used to validate the analysis and to understand the expected signal and background distributions. Datasets are simulated with different Monte Carlo (MC) generators. All simulated signal samples are passed through a simulation of the ATLAS detector using GEANT4 [140, 141]. The background samples are simulated with either GEANT4 (2022 SW) or fast simulation AtlFast3 [142] (2022+23 SW). Table 9.2 summarises the MC samples used in this data validation study.

Table 9.2 *Simulated signal and background event samples. The first column indicates the software version used to produce the MC samples. The pile-up conditions, denoted by $\langle\mu\rangle$, are shown in the second column. The mean number of interactions per bunch crossing is $\langle\mu\rangle = 42$ and $\langle\mu\rangle = 51$ for 2022 and 2023 data-taking periods respectively.*

Software	$\langle\mu\rangle$	Generator	Accuracy	Parton shower
		Signal (ggF)		
2022 2022+23 2022+23+fix	42	POWHEG	NLO NNLO	PYTHIA
		Background ($\gamma\gamma$+jets)		
2022	42	MADGRAPH5_AMC@NLO	NLO	PYTHIA
2022+23	51	SHERPA	NNLO	SHERPA

Signal samples (ggF)

Three different ggF signal samples were validated corresponding to different software versions:

1. **2022 SW:** software release developed for the analysis of the 2022 dataset;
2. **2022+23 SW:** software release developed for the analysis of the combined 2022 and 2023 dataset; and
3. **2022+23+fix SW:** identical to 2022+23 SW but with a corrected JVT implementation. For 2022+23 SW, the JVT implementation previously discarded prompt jets incorrectly. In this version, the JVT is correctly applied, retaining prompt jets whilst rejecting jets from pile-up.

All ggF samples were simulated using the POWHEG [143–145] MC generator. For the 2022 SW, NLO accuracy was achieved following the MiNLO [146] approach. For 2022+23 SW and 2022+23+fix SW, NNLO accuracy was achieved using next-to-next-to-leading order parton shower (NNLOPS) [147] simulation of Higgs boson production. The PDF4LHC21 set [148] of PDFs was used in all matrix element calculations for the hard scattering process. The samples were interfaced to PYTHIA 8.3 [149] to simulate the $H \to \gamma\gamma$ decay, parton showering and hadronisation. For all ggF samples, pile-up was modelled on the 2022 data-taking period with an average of 42 interactions per bunch crossing.

Background samples ($\gamma\gamma$+jets)

In the $H \to \gamma\gamma$ measurement, background simulated samples consist of non-resonant prompt diphoton production within $90 < m_{\gamma\gamma} < 175\,\text{GeV}$. Two background samples are used corresponding to the 2022 and 2023 data-taking periods.

Modelling 2022 data-taking conditions with $\langle\mu\rangle = 42$, the production of non-resonant diphoton events was generated using MADGRAPH5_AMC@NLO [26] at NLO accuracy. The NNPDF3.0 [150] NLO PDF set was used. Parton showering was simulated using PYTHIA 8.3.

Modelling 2023 data-taking conditions with $\langle\mu\rangle = 51$, events were generated using SHERPA 2.2 [151] for the hard scattering matrix element and parton showering. The NNPDF3.0 PDF set was used at NNLO accuracy.

9.2 Validation of ggF simulated samples

This section discusses the validation study conducted for the three ggF MC samples listed in Table 9.2. As the dominant Higgs production mode at the LHC and a key probe of the Yukawa coupling, ggF serves as the primary signal process for the analysis presented in this thesis. The 2022 SW formed the baseline of this study, validating the updated 2022+23 SW software developed for the analysis of the combined 2022 and 2023 dataset.

Comparing the 2022 SW and 2022+23 SW ggF MC samples, Table 9.3 presents the relative efficiency of each stage in the $H \to \gamma\gamma$ event selection. Between the two samples, the main difference in the selection efficiency appears in the isolation

Table 9.3 *Selection cutflow efficiency for ggF MC samples produced using different software versions: 2022 SW and 2022+23 SW. Rows highlighted in orange indicate significant differences in the cutflow efficiency between the two samples.*

Selection step	**2022 SW** rel. eff.	**2022+23 SW** rel. eff.
Pass trigger	57.6%	57.7%
Detector data quality	100.0%	100.0%
Has primary vertex	100.0%	100.0%
2 loose photons	88.3%	88.8%
e-γ ambiguity	100.0%	100.0%
Trigger match	97.1%	97.0%
Tight identification	87.9%	87.9%
Isolation	89.3%	91.4%
Rel. p_{T} cuts	92.9%	93.0%
$m_{\gamma\gamma} \in [105,160]$ GeV	100.0%	100.0%

step. This is expected, however, due to the new isolation leakage correction implemented in 2022+23 SW. All other selection steps show a good agreement between the two samples.

9.2.1 Photons

Photons are the primary particles of interest in the $H \to \gamma\gamma$ analysis. The transverse momentum of the diphoton system, $p_{\mathrm{T},\gamma\gamma}$, characterises the fundamental kinematics of the Higgs boson. Additionally, the relative transverse momenta of the leading and subleading photons, $p_{\mathrm{T},\gamma 1}/m_{\gamma\gamma}$ and $p_{\mathrm{T},\gamma 2}/m_{\gamma\gamma}$, provide insights into the kinematics of the Higgs boson decay. It is crucial to validate that the diphoton kinematics behave as expected in MC simulated samples.

Figure 9.1 presents photon kinematics for the different ggF MC samples. In the baseline 2022 SW sample (black line), the matrix element was calculated at NLO accuracy. In contrast, the 2022+23 SW (blue marker) and 2022+23+fix SW (red marker) samples were generated at NNLO accuracy and show a good agreement with one another. The observed differences in photon kinematics relative to the 2022 SW sample can be attributed to the higher-accuracy matrix element calculation. Thus, the photon kinematics behave as expected.

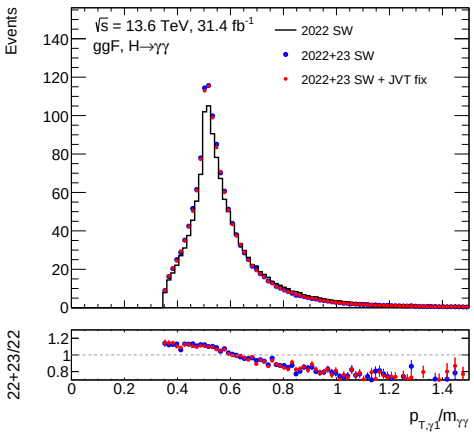

(a) *Relative* $p_{T,\gamma 1}$

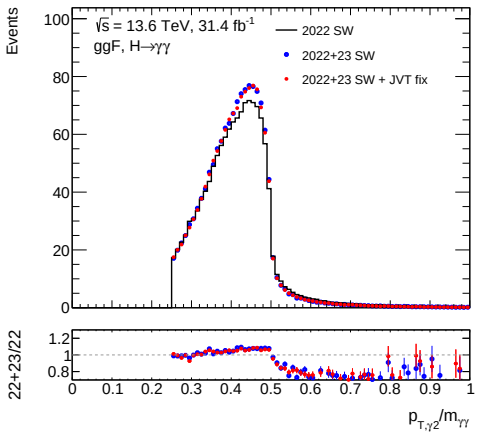

(b) *Relative* $p_{T,\gamma 2}$

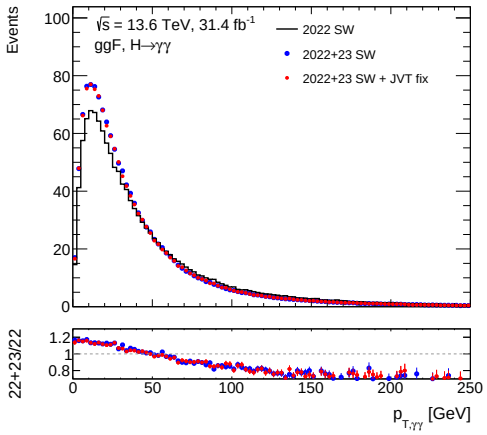

(c) $p_{T,\gamma\gamma}$

Figure 9.1 *Validation plots of photon kinematics: (a) relative* $p_{T,\gamma 1}$*, (b) relative* $p_{T,\gamma 2}$ *and (c)* $p_{T,\gamma\gamma}$ *for the ggF MC samples listed in Table 9.2. Three samples are compared corresponding to different software versions: (1) 2022 SW (black line); (2) 2022+23 SW (blue marker); and (3) 2022+23+fix SW (red marker).*

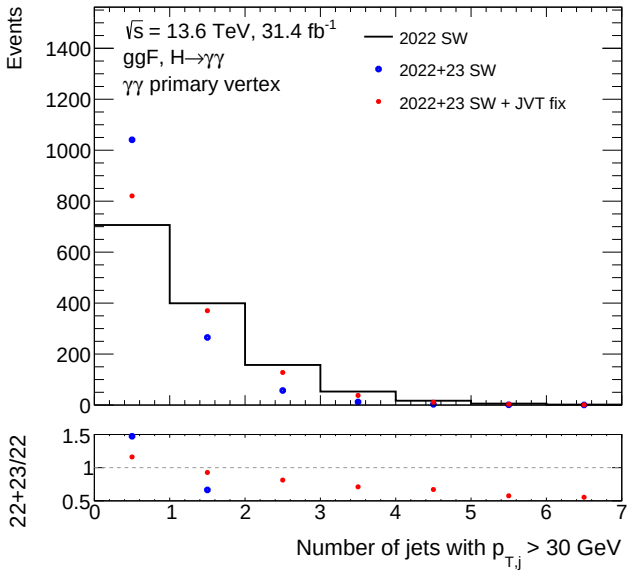

Figure 9.2 *Validation plot of jet multiplicity for the ggF MC samples listed in Table 9.2. Three samples are compared corresponding to different software versions: (1) 2022 SW (black line); (2) 2022+23 SW (blue marker); and (3) 2022+23+fix SW (red marker).*

9.2.2 Jets

The validation of jet objects was performed for the new software as part of the $H \to \gamma\gamma$ cross-section analysis.

There are two different collections of reconstructed jets (see Section 7.7) available in $H \to \gamma\gamma$ generated MC samples that use different primary vertices:

1. **Athena jet collection** defined using the standard hard-scatter primary vertex (Section 7.3) denoted as $\sum_{\text{tracks}} p_{\text{T}}$ primary vertex; and
2. **$\gamma\gamma$ jet collection** defined using the $H \to \gamma\gamma$ custom primary vertex (Section 7.5.3) denoted as $\gamma\gamma$ primary vertex.

The $\gamma\gamma$ jet collection is the primary jet collection used in $H \to \gamma\gamma$ analyses.

Figure 9.2 presents the jet multiplicity distribution for the $\gamma\gamma$ jet collection. In the 2022+23 SW sample (blue marker), the distribution appears significantly softer compared to the 2022 SW sample (black line). The 2022+23 SW sample therefore exhibits a higher number of events with no jets, suggesting the Jet Vertex Tagger (JVT) (see Section 7.7.1) may have been applied differently between the two samples.

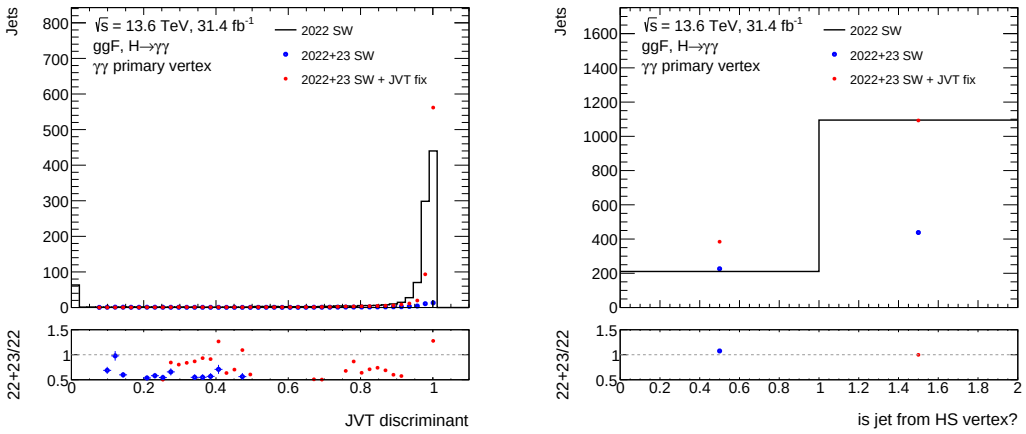

(a) *γγ jet collection* **(b)** *γγ jet collection*

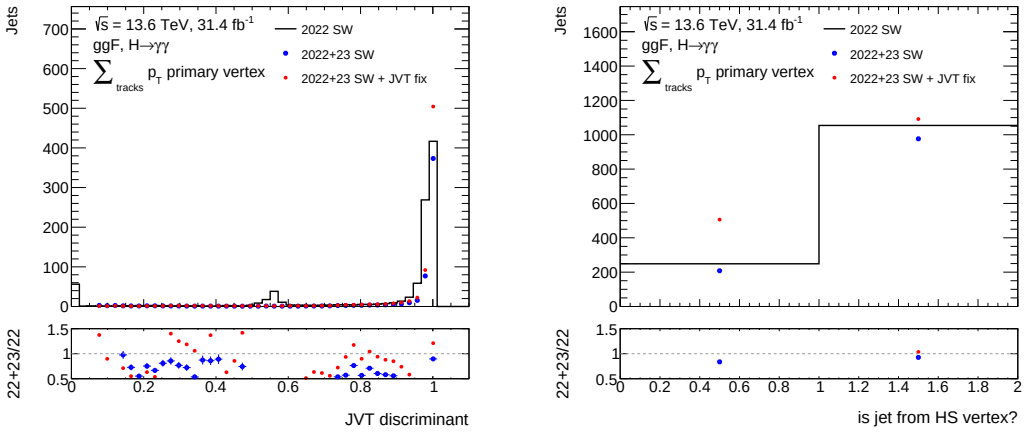

(c) *Athena jet collection* **(d)** *Athena jet collection*

Figure 9.3 *Validation of JVT for different jet collections. Three samples are compared corresponding to different software versions: (1) 2022 SW (black line); (2) 2022+23 SW (blue marker); and (3) 2022+23+fix SW (red marker). (a) & (b) show the JVT discriminant and hard-scatter vertex flag for the γγ jet collection. For the hard-scatter vertex flag, a value of 1 indicates the reconstructed jet is truth-matched to a jet originating from the hard-scatter. (c) & (d) show the same for the Athena jet collection.*

Figure 9.3a presents the JVT discriminant for the $\gamma\gamma$ jet collection. The first observation is the peak at zero for the 2022 SW sample (black line) which indicates the JVT discriminant cut is not applied; a peak at zero is consistent with jets from pile-up which cutting on the JVT discriminant aims to suppress. In contrast, the JVT distribution for the 2022+23 SW sample (blue marker) starts at around 0.1 which indicates the new dynamic JVT cut is applied. Furthermore, the peak around one for the 2022 SW sample is consistent with prompt jets from the hard-scatter which the cut on the JVT discriminant aims to keep. The peak around one is suppressed for the 2022+23 SW sample (blue marker), indicating that the JVT cut is discarding prompt jets incorrectly. Figure 9.3b confirms this which shows the hard-scatter vertex flag for the $\gamma\gamma$ jet collection. Around 1100 jets are identified as originating from the hard-scatter vertex for the 2022 SW sample (black line) compared to around 400 jets for the 2022+23 SW sample (blue marker) — approximately a 65% reduction in hard-scatter jets.

Figure 9.3c presents the JVT discriminant for the Athena jet collection. As observed for the $\gamma\gamma$ jet collection, the JVT cut is not applied for the 2022 SW sample (black line). Similarly, for the 2022+23 SW sample (blue marker), the dynamic JVT cut is applied. The peak around one is present for both the 2022 SW and 2022+23 SW samples indicating that the JVT is implemented correctly. This is confirmed in Figure 9.3d which shows the hard-scatter vertex flag for the Athena jet collection. The 2022 SW (black line) and 2022+23 SW (blue marker) distributions are consistent with one another confirming the JVT is correctly implemented in the Athena jet collection.

This validation study identified a bug in the JVT implementation for the $\gamma\gamma$ jet collection in the 2022+23 SW. The developers for the $H \to \gamma\gamma$ software have since fixed the bug and an updated software version, 2022+23+fix SW, has been released.

Returning to Figure 9.2, the jet multiplicity for the 2022+23+fix SW sample (red marker) is more consistent with the 2022 SW sample (black line). Since the JVT cut is not applied to the 2022 SW sample, the remaining differences between the 2022 SW and 2022+23+fix SW samples are expected.

Similarly, returning to Figure 9.3, the JVT discriminant and hard-scatter vertex flag are shown for the 2022+23+fix SW (red marker) sample. Figures 9.3a and 9.3b show that the JVT is now correctly implemented in the $\gamma\gamma$ jet collection. Figures 9.3c and 9.3d confirm the JVT remains correctly implemented in the

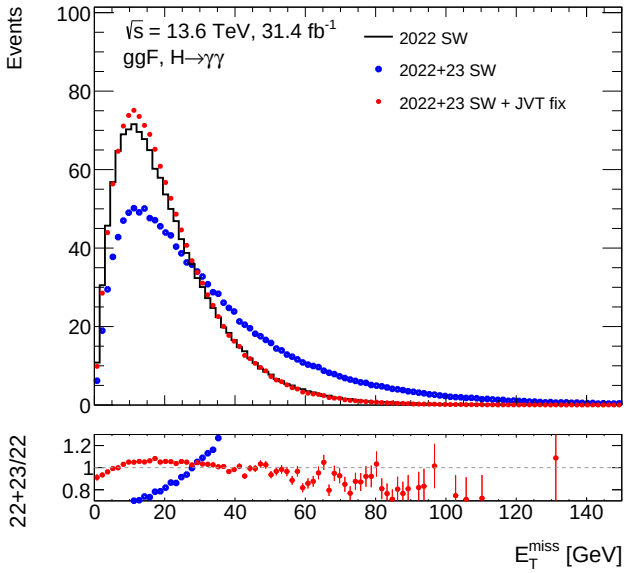

Figure 9.4 *Validation plot of MET for the ggF MC samples. Three samples are compared corresponding to different software versions: (1) 2022 SW (black line); (2) 2022+23 SW (blue marker); and (3) 2022+23+fix SW (red marker).*

Athena jet collection. For the 2022+23+fix SW sample, both jet collections behave as expected.

9.2.3 Missing transverse energy

MET, introduced in Section 7.8, is calculated by balancing the transverse momentum of all particles in the event. Since MET is calculated using the $\gamma\gamma$ jet collection, the bug in the JVT implementation is reflected in the MET distribution as shown in Figure 9.4. A broader MET distribution is observed for the 2022+23 SW sample (blue marker) compared to the 2022 SW (black line). Discarding prompt jets increases the soft component of MET resulting in higher *fake* MET. For the 2022+23+fix SW sample (red marker), the MET distribution with the JVT fix implemented shows a much better agreement with the 2022 SW sample (black line) as expected.

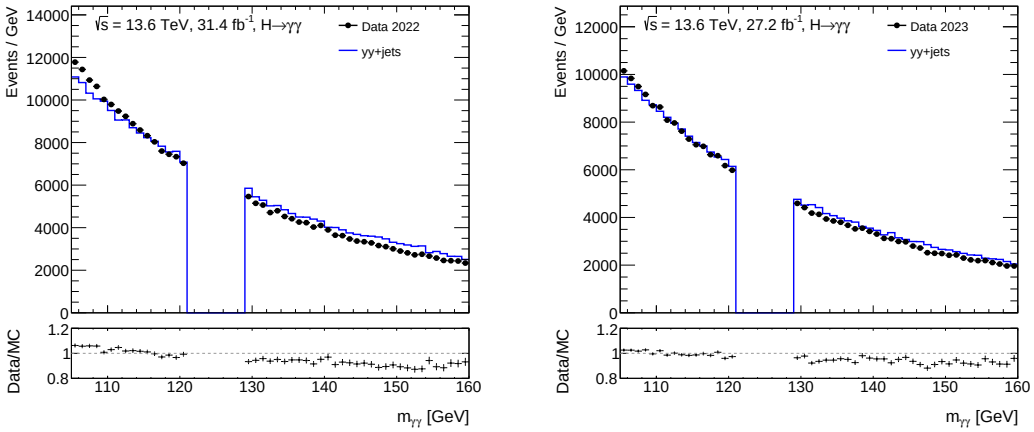

(a) *2022 data control regions* **(b)** *2023 data control regions*

Figure 9.5 *Validation plots of the $m_{\gamma\gamma}$ data control regions for 2022 and 2023 datasets. Data are represented with black markers. Simulated background $\gamma\gamma$+jets MC samples are shown in blue lines. The simulated samples are produced with the relevant pile-up conditions for the 2022 and 2023 data-taking periods.*

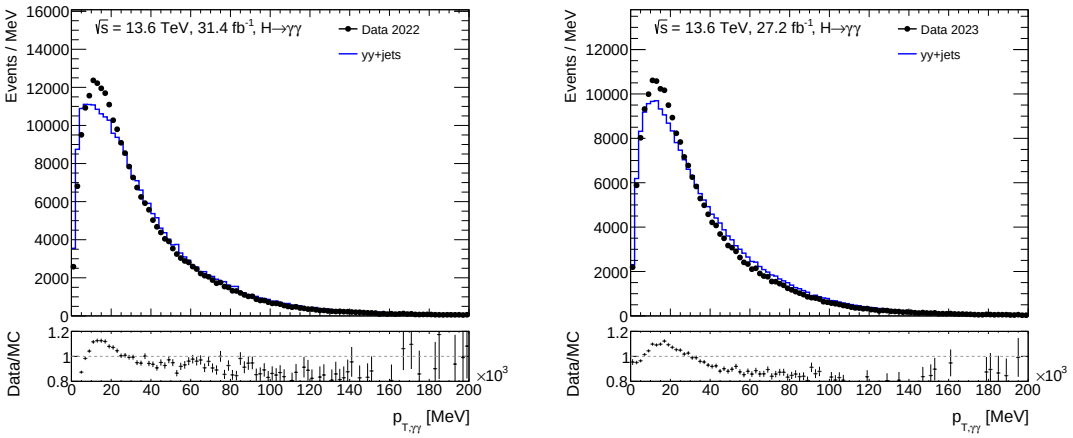

Figure 9.6 *Validation of $p_{T,\gamma\gamma}$ in the data control regions for the 2022 and 2023 datasets. Data are represented with black markers. Simulated background $\gamma\gamma$+jets MC samples are shown in blue lines.*

9.3 Validation of data control regions

The Higgs boson signal is measured in the diphoton invariant mass, $m_{\gamma\gamma}$, spectrum. The signal and control regions are defined as:

- **Signal region**: $121 < m_{\gamma\gamma} < 129\,\text{GeV}$; and
- **Control regions**: $105 < m_{\gamma\gamma} < 121\,\text{GeV}$, $129 < m_{\gamma\gamma} < 160\,\text{GeV}$.

Whilst developing the analysis, the signal region in the data is blinded. The data control regions, however, are used to understand the expected background distributions.

The $m_{\gamma\gamma}$ control regions for the 2022 and 2023 datasets are shown in Figure 9.5. To model the background in the control regions, the $\gamma\gamma$+jets MC samples from Table 9.2, simulated with the relevant pile-up for the 2022 and 2023 data-taking periods, are plotted. Non-resonant $\gamma\gamma$ production is the dominant background measured at around 73% for the 2022 data (see Section 8.3.2). In Figure 9.5, the $\gamma\gamma$+jets samples have been scaled to the data in the control regions. The $m_{\gamma\gamma}$ distributions for the $\gamma\gamma$+jets MC samples are therefore not representative of the full background composition. As a result, differences between the data and MC distributions are observed. This is reflected in the photon kinematics in the control regions, as shown in Figure 9.6. The background samples for the respective data-taking periods are consistent with one another. Using $\gamma\gamma$+jets to model the background in the control regions, however, is sub-optimal.

9.4 Summary

This chapter focuses on the validation of the combined 2022+2023 dataset, the corresponding simulated samples and the software used to analyse them. The goal of this validation is to identify any issues that could impact this thesis and the ongoing $H \to \gamma\gamma$ analyses. Through this validation study, a software bug affecting jets and MET was identified. After the bug was fixed by the developers, this thesis demonstrates that the data and simulated samples under validation align with the expectations based on the 2022 reference samples. The combined 2022+2023 dataset, simulated samples and analysis software can therefore be considered validated.

Chapter 10

Signal modelling

In this chapter, I present the signal modelling I performed for the $H \to \gamma\gamma$ cross-section analysis. This study validated the signal modelling parameterisation using MC generated events produced with the software developed for the analysis of the combined 2022+2023 dataset. The simulated events and software used in the early Run 3 publication in Ref. [118], analysing the 2022 dataset, served as the baseline for comparison. Different regions of phase space that are sensitive to different Higgs boson production modes are studied. The signal modelling is compared for each of these regions and the results are presented here.

10.1 Simulated data

To model the $H \to \gamma\gamma$ signal in the cross-section analysis, the main Higgs boson production modes at the LHC are considered: ggF, VBF, VH and $t\bar{t}H$. For these production modes, the signal modelling was performed with MC generated $H \to \gamma\gamma$ samples produced using the different software versions introduced in Section 9.1.2:

1. **2022 SW**: software release developed for analysis of the 2022 dataset; and
2. **2022+2023 SW**: software release developed for the analysis of the combined 2022+2023 dataset with the JVT fix included (referred to as 2022+23+fix SW in Chapter 9).

From henceforth the 2022+23+fix SW will be referred to as 2022+2023 SW.

Simulated $H \to \gamma\gamma$ signal events are compared for ggF, VBF, WH, ZH and $t\bar{t}H$ Higgs boson production. All samples used the PDF4LHC21 set of PDFs in the matrix element calculation. The samples were produced using the POWHEG generator and interfaced to PYTHIA for parton showering and hadronisation.

10.2 Diphoton fiducial region

Table 10.1 *Expected number of events ($N = \sigma \times BR \times \mathcal{L} \times \epsilon$) in the diphoton fiducial region. An integrated luminosity of $\mathcal{L} = 31.4\,\text{fb}^{-1}$, $H \to \gamma\gamma$ branching ratio of $BR = 0.23\%$ and cutflow efficiency of $\epsilon = 36\%$ is assumed. SM predictions for the Higgs boson production cross-section values at 13.6 TeV are used.*

Process	$\sigma \times$ BR [fb]	Expected events
ggF	118.43	1338.69
VBF	9.25	104.56
$pp \to WH$	3.30	37.28
$pp \to ZH$	2.14	24.18
$t\bar{t}H$	1.29	14.60
Total		1519.13

Table 10.1 shows the expected number of events in the diphoton fiducial region for the different Higgs boson production modes. Assuming a cutflow efficiency

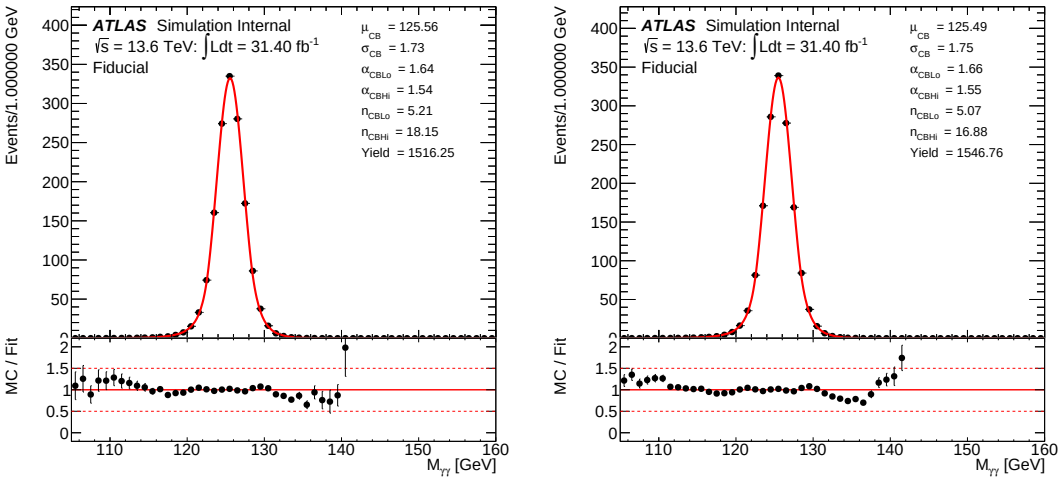

(a) *Diphoton fiducial, 2022 SW* **(b)** *Diphoton fiducial, 2022+2023 SW*

Figure 10.1 *DSCB fit to simulated $H \to \gamma\gamma$ events for the diphoton fiducial region with (a) 2022 SW and (b) 2022+2023 SW.*

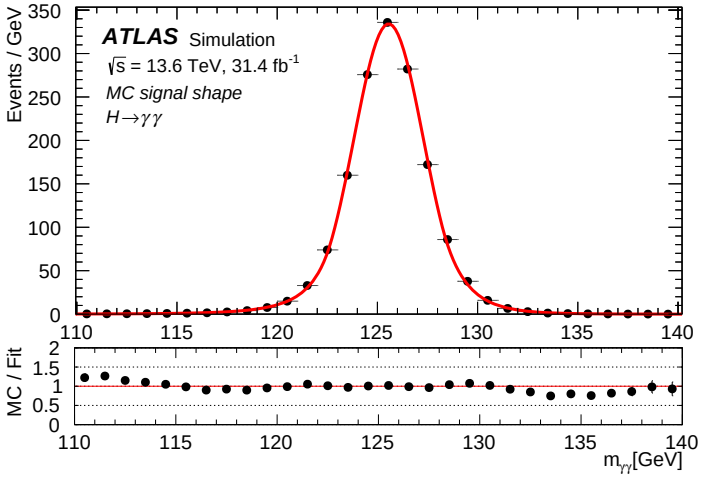

Figure 10.2 *DSCB fit to simulated $H \to \gamma\gamma$ events in the diphoton fiducial region from the early Run 3 measurement in Ref. [118].*

Table 10.2 *Comparing signal modelling yields in the different fiducial regions for the different software versions: 2022 SW and 2022+2023 SW. The percentage difference in the yield between both software versions is also shown.*

Fiducial region	2022 SW Yield	2022+2023 SW Yield	Difference [%]
Diphoton	1516.25	1546.76	+2.0
VBF-enhanced	36.11	34.09	−5.8
$N_{\text{lepton}} \geq 1$	11.61	12.06	+3.8
High $E_{\text{T}}^{\text{miss}}$	15.51	12.51	−21.4
$t\bar{t}H$-enhanced	12.69	14.97	+16.5

of 36% from the 2022 SW, the total expected number of events is 1519.13 for $31.4\,\text{fb}^{-1}$ of integrated luminosity. For both the 2022 SW and 2022+2023 SW, the yields from the DSCB fit to the $m_{\gamma\gamma}$ distribution for the diphoton fiducial region are shown in Figure 10.1. The percentage difference between the expected number of events and the fit yield is −0.19% and +1.80% for the 2022 SW and 2022+2023 SW, respectively.

The DSCB fit to simulated $H \to \gamma\gamma$ events from the early Run 3 publication is shown in Figure 10.2. The samples used were generated with the 2022 SW. The DSCB shape peaks at approximately 340 events, consistent with the distributions shown in Figure 10.1. Excluding the tails, the ratio plots in Figure 10.1 show the fits are consistent with the data points for both software versions.

The signal yields are 1516.25 and 1546.76 for the 2022 SW and 2022+2023 SW respectively. The difference between the yields for both software versions is +2.0%, as shown in Table 10.2. Given the improvement in the isolation requirements for the 2022+2023 SW discussed in Section 9.2, an increase of around 2% in the yield is expected and observed in the data (see Table 9.1). This is also reflected in the difference between the expected number of events and the 2022+2023 SW yield. The signal modelling in the diphoton fiducial region is as expected for both software versions, indicating that the 2022+2023 SW accurately models the $H \to \gamma\gamma$ signal in this region.

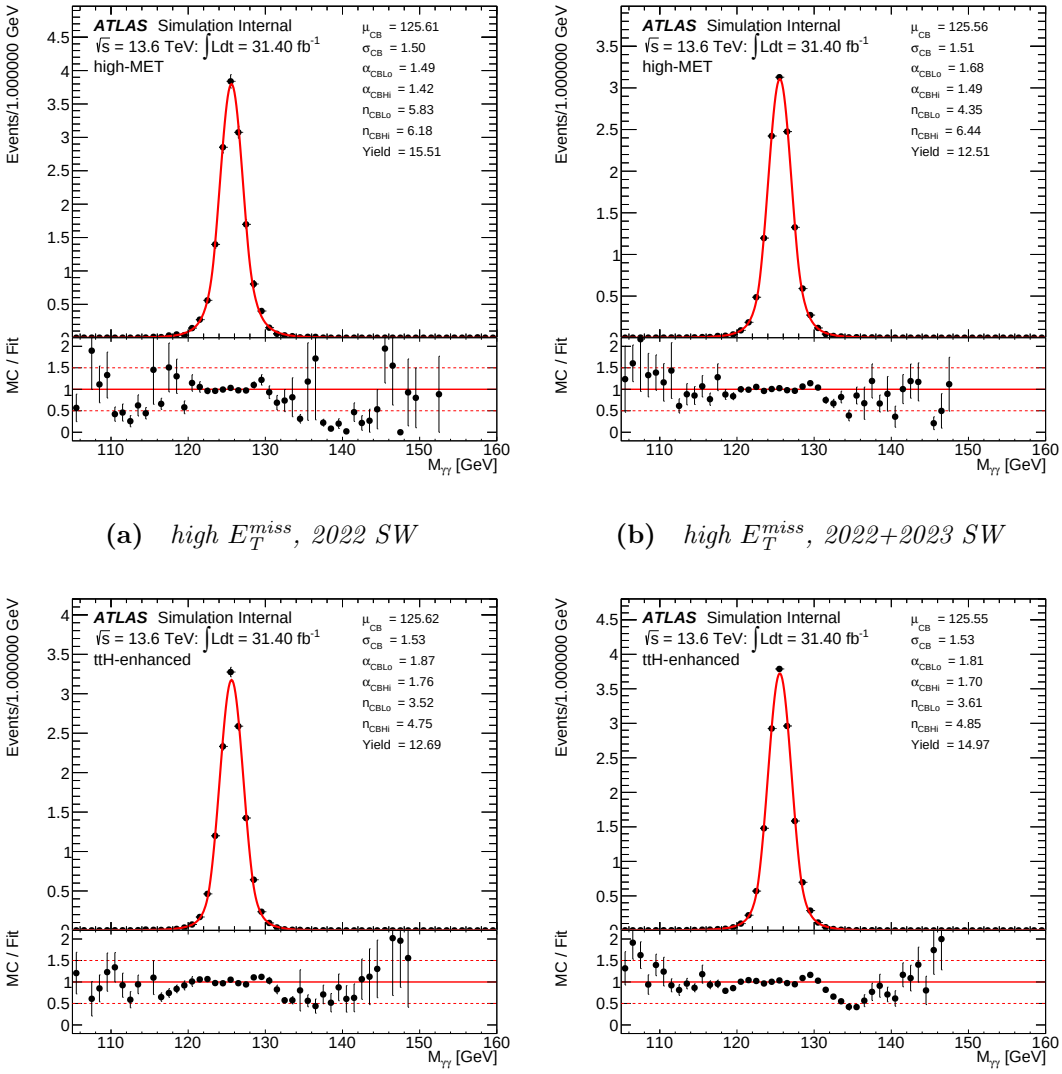

(a) *high E_T^{miss}, 2022 SW* **(b)** *high E_T^{miss}, 2022+2023 SW*

(c) *$t\bar{t}H$-enhanced, 2022 SW* **(d)** *$t\bar{t}H$-enhanced, 2022+2023 SW*

Figure 10.3 *DSCB fit to simulated $H \to \gamma\gamma$ events in the high E_T^{miss} and $t\bar{t}H$-enhanced fiducial subregion with (a) & (c) 2022 SW and (b) & (d) 2022+2023 SW.*

10.3 Fiducial subregions

The different fiducial regions allow for the validation of the $H \to \gamma\gamma$ signal, using the DSCB function introduced in Section 8.3.1, for different Higgs boson production modes.

Table 10.2 compares the signal yields extracted from the DSCB fit to the $m_{\gamma\gamma}$ distribution for all fiducial regions introduced in Section 8.2.3. Since the fiducial subregions were not used in the early Run 3 publication, there are no previous results for comparison at 13.6 TeV. The 2022 SW, however, was used in the publication and thus serves as the baseline for comparison in this study.

As discussed in the previous section, a +2% increase is expected in the signal yield for the 2022+2023 SW due to the improved isolation requirements. This is reflected in the diphoton and $N_{\text{lepton}} \geq 1$ fiducial regions as shown in Table 10.2. Modelling of the $H \to \gamma\gamma$ signal is as expected in these regions.

For the VBF-enhanced subregion, the difference in the signal yield is −5.8% for 2022+2023 SW compared to 2022 SW. As discussed in Section 9.2.2, the JVT discriminant cut is not applied in the 2022 SW. Since the JVT cut is applied in the 2022+2023 SW, a reduction in jets from pile-up is observed. This is expected to result in a lower signal yield in the VBF-enhanced region, explaining the observed difference between the samples.

The high $E_{\text{T}}^{\text{miss}}$ subregion shows the largest discrepancy between the two software versions with a −21.4% difference in the signal yield. The fits are shown in Figures 10.3a and 10.3b for 2022 SW and 2022+2023 SW respectively. The height of the fitted DSCB is approximately 4 events for 2022 SW, compared to about 3 events for 2022+2023 SW. Validation of $E_{\text{T}}^{\text{miss}}$ was discussed in Section 9.4 for ggF simulated events. Whilst the JVT fix improved the $E_{\text{T}}^{\text{miss}}$ distribution for 2022+2023 SW, some residual differences in Figure 9.4 remain between the two software versions which are not yet fully understood.

Similarly, the $t\bar{t}H$-enhanced subregion shows a +16.5% difference in the signal yield between the two software versions. The fits are shown in Figures 10.3c and 10.3d for the 2022 SW and 2022+2023 SW respectively. The peak heights differ with 2022 SW peaking at approximately 3.2 events and 2022+2023 SW peaking at around 3.8 events. Additionally, the fits in Figure 10.3c and 10.3d both peak below the data points. This will have some effect on the signal yield

extracted from the fit but is unlikely the sole cause of the observed differences. The remaining differences between the two software versions require further investigation.

10.4 Summary

This chapter focuses on validating the modelling of the $H \to \gamma\gamma$ signal for the new software developed to analyse the combined 2022+2023 dataset. The goal of this study is to ensure that the new software accurately models the $H \to \gamma\gamma$ signal in the different regions of phase space, sensitive to different Higgs production modes, studied in the $H \to \gamma\gamma$ cross-section analysis. This study observes that the signal modelling performs as expected compared to the reference for three out of five regions studied. The signal modelling is in these regions can therefore be considered validated. The remaining two regions show large discrepancies between the reference and samples under validation. The residual differences are yet to be understood and require further investigation.

Chapter 11

Constraining up, down and charm quark Yukawa couplings

In this chapter, I present the novel technique I developed for constraining the charm and light (up and down) quark Yukawa couplings. The sensitivity to quark couplings comes from the difference between quark-initiated ($q\bar{q} \to H$) and gluon-initiated (ggF) Higgs boson production. In the $H \to \gamma\gamma$ cross-section measurement in Ref. [7], this difference was used to set stringent constraints on the charm quark Yukawa coupling. For Run 3, I introduce first-generation quarks into the analysis, exploiting their distinct parton distribution function (PDF). To simultaneously account for the quark versus gluon initial state differences and the differences in the PDFs, my analysis develops the technique used in Run 2 further by introducing a neural network classifier. Furthermore, the expected two-dimensional limits on the light and charm quark Yukawa couplings are presented here with an outlook to the full Run 3 and HL-LHC datasets.

11.1 Datasets

11.1.1 Data and pseudo-data

This thesis uses $58.6\,\text{fb}^{-1}$ of the Run 3 dataset (see Section 9.1.1). The analysis presented in this thesis is expected to be published with a larger ATLAS Run 3 dataset. The data is therefore blinded in the signal region and expected bounds on the quark Yukawa couplings are extracted using simulated ggF events (see Section 9.1.2) to model the SM signal.

The *pseudo-data* used in this thesis consists of: blinded partial Run 3 data, extrapolated background counts in the signal region and simulated ggF events.

11.1.2 Simulated data

The signal samples used to train the neural network classifier are summarised in Table 11.1. The samples were produced using the MadGraph5_aMC@NLO generator with the light quark Yukawa couplings implementation from Ref. [152], courtesy of the author. Furthermore, the samples were interfaced to Pythia for parton showering and hadronisation. All samples are generated at $\sqrt{s} = 13.6\,\text{TeV}$ and containing particle-level events meaning no detector effects are included.

Table 11.1 *Samples used to train the neural network classifier.*

Process	Generator	Accuracy	Parton shower
ggF $cc \to H$ $uu, dd \to H$	MadGraph5_aMC@NLO	NLO QCD	Pythia

The event generation is performed at NLO in QCD and the corresponding $u\bar{u} \to H$ production diagrams are shown in Figure 11.1. In addition to the eight diagrams shown in Figure 11.1, the eight corresponding charge conjugate diagrams ($u \to \bar{u}$, $\bar{u} \to u$) are also included.

Figure 11.2 shows example higher order production diagrams, not included in the event generation or the functional forms parameterising the κ_u effects (see Table 3.4), calculated at NNLO in QCD. Likewise, higher order diagrams affecting

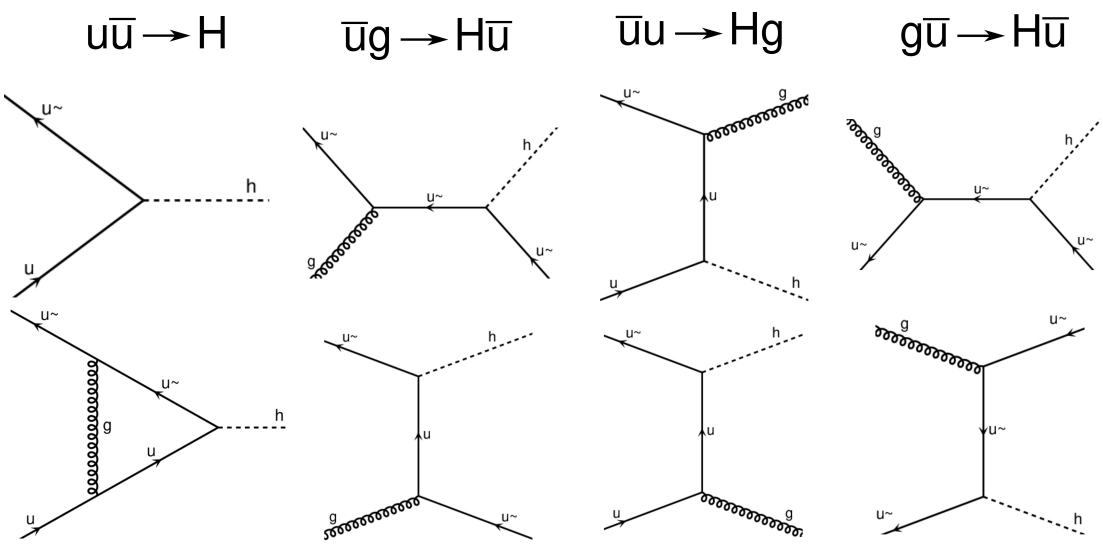

Figure 11.1 *Feynman diagrams included in $u\bar{u} \to H$ production at NLO in QCD. Corresponding charge conjugate diagrams ($u \to \bar{u}$, $\bar{u} \to u$) are also included. Figure generated with* MadGraph5_aMC@NLO *[26].*

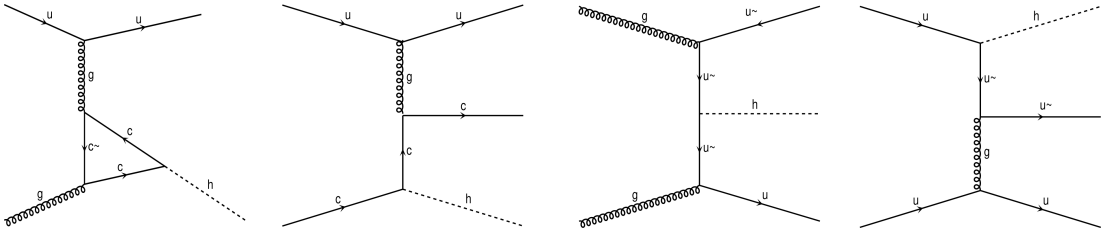

Figure 11.2 *Example NNLO QCD diagrams not included in the $u\bar{u} \to H$ production. The first two diagrams show that, at higher orders, variations of κ_c would also affect the $u\bar{u} \to H$ production. The third and fourth diagrams show the production via two initial state gluons or two valence quarks respectively which would affect the final state kinematics. Figure generated with* MadGraph5_aMC@NLO *[26].*

the Higgs decay are not considered in the functional forms. The first two diagrams in the figure show that, at higher orders, variations of κ_c (and equivalently κ_t or κ_b) would also affect $u\bar{u} \to H$ production. Considering production or decay effects beyond NLO in QCD, κ_u is therefore an effective parameter.

11.1.3 Event selection

The full event selection described in Section 8.2 is used in this analysis. To calculate expected number of signal events, an efficiency of 36% is assumed from the total cutflow efficiency for ggF simulated events. The total cutflow

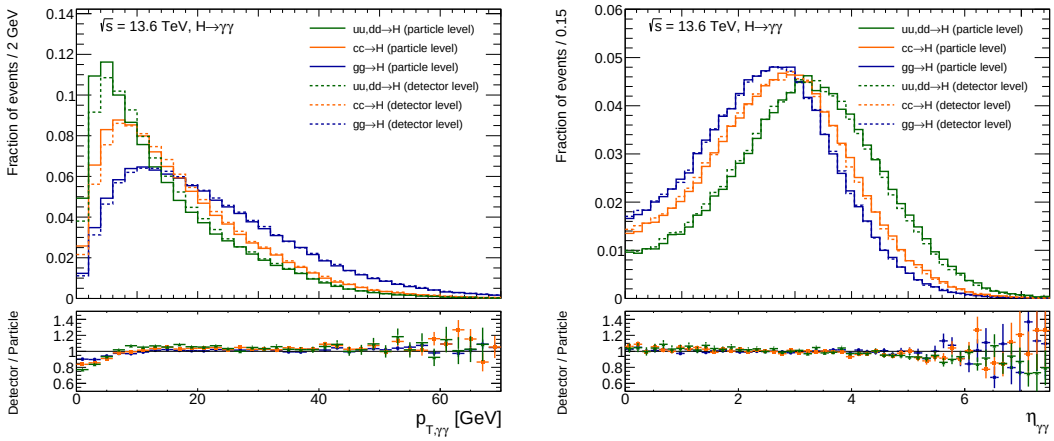

(a) $p_{T,\gamma\gamma}$, *particle vs. detector level* **(b)** $\eta_{\gamma\gamma}$, *particle vs. detector level*

Figure 11.3 *Diphoton (a) $p_{T,\gamma\gamma}$ and (b) $\eta_{\gamma\gamma}$ distributions at particle vs. detector level.*

includes kinematic, trigger, reconstruction and isolation efficiencies as detailed in Section 9.2.

The focus of this analysis is on Higgs production modes that are sensitive to the charm and light quark Yukawa couplings. All other production modes are considered background and are reduced by applying additional cuts to the data. Section 8.2.2 introduced subregions of phase space which are sensitive to VBF, VH and $t\bar{t}H$ production modes. The cuts used to define these subregions are inverted here to reduce the contributions from these production modes. See Appendix A for more details.

11.1.4 Parametric detector response for photons

The samples used to train the neural network are particle-level events. To train on samples that are realistic representations of data, detector effects must be included. It is computationally expensive to simulate the full detector response and so an alternative approach is used. This was achieved by applying a parameteric detector response developed in Ref. [153] to apply detector effects to the photon four-momenta. Figure 11.3 compares the $p_{\mathrm{T},\gamma\gamma}$ and $\eta_{\gamma\gamma}$ distributions for the three samples in Table 11.1 at particle and detector level. Given the high resolution of the ECal, adding the detector effects has a minimal effect on the distributions.

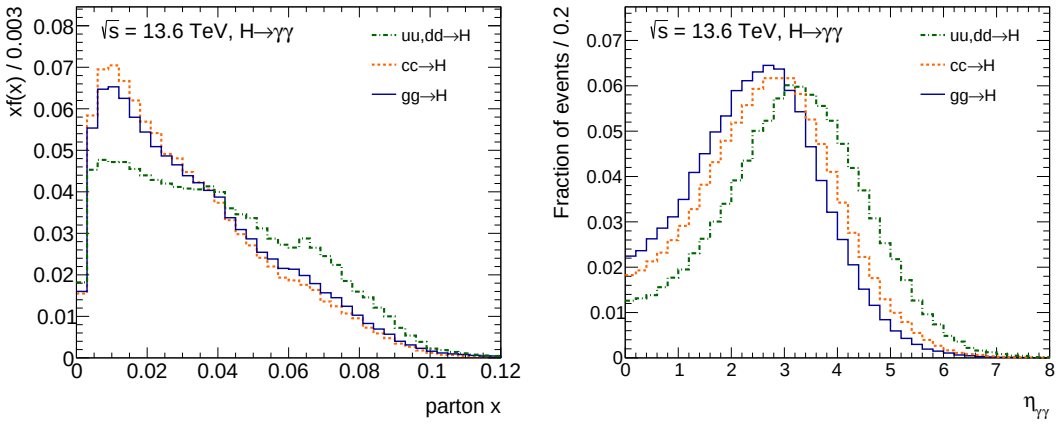

(a) *Partonic x* **(b)** *Pseudorapidity*

Figure 11.4 *PDF effects for different Higgs production modes illustrated through (a) partonic x and (b) pseudorapidity of the diphoton system.*

11.2 Signal neural network classifier

This section introduces a neural network classifier designed to distinguish between different Higgs boson production modes. The aim of this classifier is to create three orthogonal signal regions that are sensitive to the charm and light (up and down) quark Yukawa couplings defined as follows:

1. **ggF-enhanced**: sensitive to the Yukawa couplings through the quark-loop-induced ggF production;
2. **κ_c-enhanced**: sensitive to the charm quark Yukawa coupling through $c\bar{c} \to H$ production; and
3. **$\kappa_{u,d}$-enhanced**: sensitive to the light quark Yukawa couplings through $u\bar{u} \to H$ and $d\bar{d} \to H$ production.

11.2.1 Feature selection

Ref. [32] demonstrates that exploiting the Higgs rapidity and p_{T} distributions offers greater sensitivity to the light quark Yukawa couplings than solely measuring the inclusive Higgs cross-section.

The Yukawa interpretation from the Run 2 $H \to \gamma\gamma$ cross-section publication in Ref. [7] used only the $p_{\mathrm{T},\gamma\gamma}$ spectrum as the discriminating variable to separate

$c\bar{c} \to H$ and ggF production modes. As described in Section 3.7.3, the $p_{\mathrm{T},\gamma\gamma}$ spectrum is sensitive to the quark Yukawa couplings through differences in initial state radiation, dictated by the colour charge of the incoming partons. The difference in initial state radiation between quarks and gluons applies to all quark flavours; up, down, strange, charm and bottom. Ref. [7] sets the up, down and strange quark couplings to the SM values and extracts two-dimensional constraints on the charm and bottom quark couplings. The bottom quark coupling is well-constrained from direct $H \to b\bar{b}$ measurements which can be used to set a stringent constraint on the charm quark Yukawa coupling.

This analysis introduces the rapidity of the diphoton system as a discriminating variable to enhance the sensitivity to the light quark Yukawa couplings. Since the first-generation quarks are valence quarks in the colliding protons, $u\bar{u} \to H$ and $d\bar{d} \to H$ production have an asymmetry in the distribution of partonic x compared to ggF, $s\bar{s} \to H$, $c\bar{c} \to H$ and $b\bar{b} \to H$. This is illustrated in Figure 11.4a which plots partonic x for the different Higgs production modes. Peaking in the forward region of the detector, the asymmetry in $u\bar{u} \to H$ and $d\bar{d} \to H$ production is reflected in the pseudorapidity of the diphoton system as shown in Figure 11.4b.

In the remainder of this analysis, the following assumptions are made:

- $\boldsymbol{\kappa_b}$ **is set to 1**. $H \to b\bar{b}$ measurements constrain κ_b within $\sim 10\%$ of the SM value [154] with an expected uncertainty of $\sim 4\%$ at the HL-LHC [155]. Thus, any allowed variation of κ_b would have a small impact on this analysis.
- $\boldsymbol{\kappa_c}$ **is treated as a free-floating parameter** to be constrained in the dedicated κ_c-enhanced signal region.
- $\boldsymbol{\kappa_s}$ **is set to 1** to simplify the presentation of the results. In this analysis, the effects of the κ_s variation are indistinguishable from the κ_c variation. At the HL-LHC, $H \to c\bar{c}$ measurements are expected to constrain κ_c to within $\sim 20\%$ of the SM value [155], breaking the degeneracy.
- $\boldsymbol{\kappa_u}$ **is a free-floating parameter, with the assumption** $\boldsymbol{\kappa_d = \kappa_u}$**,** and is constrained within the dedicated $\kappa_{u,d}$-enhanced signal region.

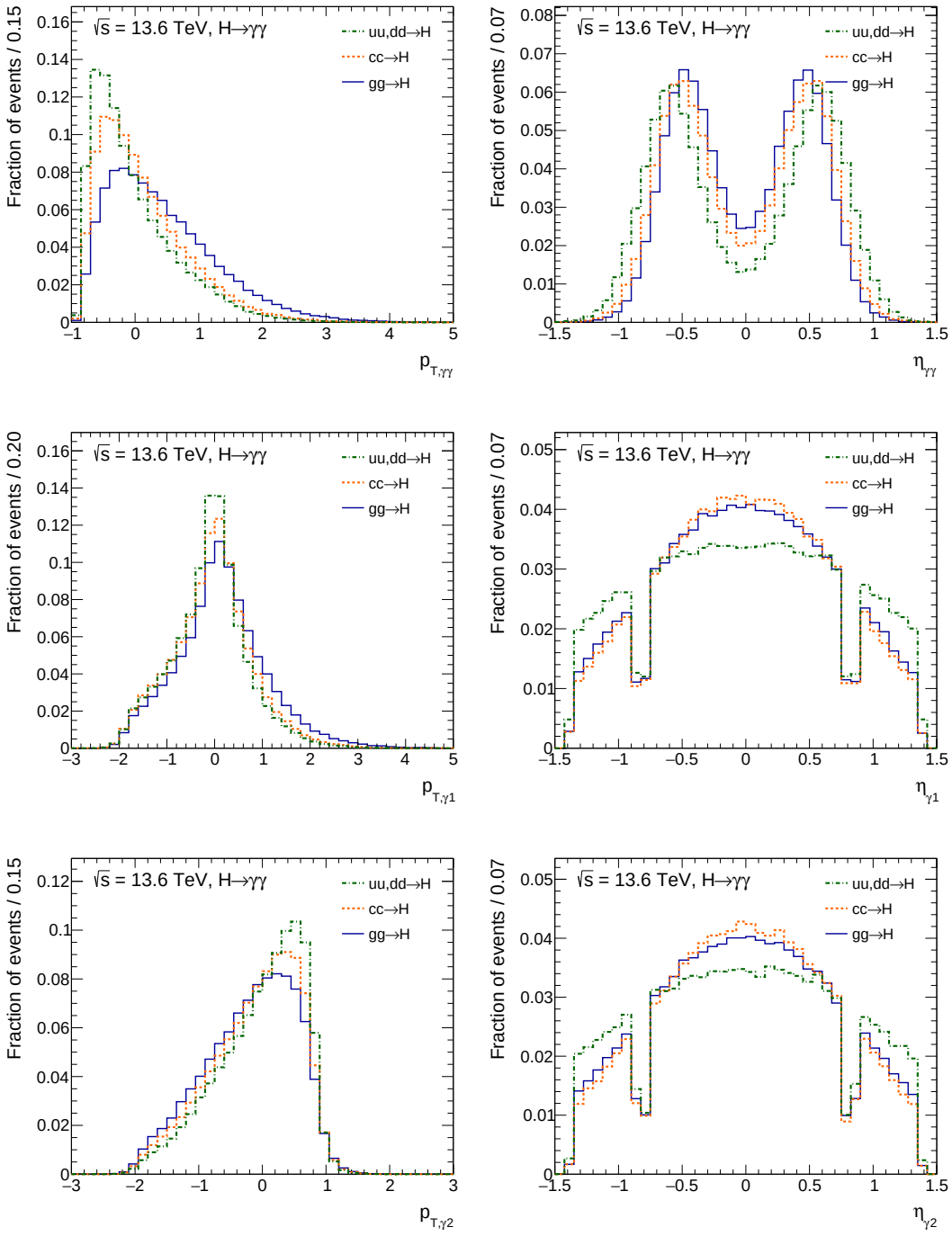

Figure 11.5 *Example input features distributions after applying the robust scaling method.*

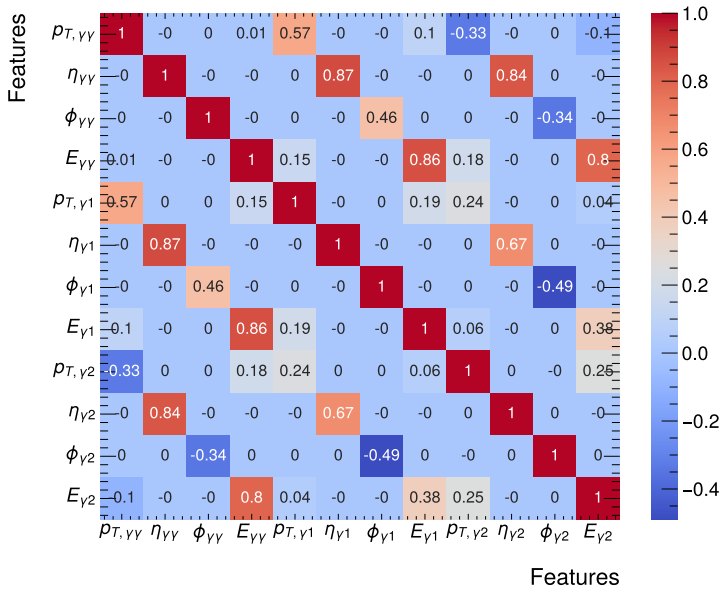

Figure 11.6 *Correlation matrix of the input features used in the signal classifier. Perfect positive and negative correlation are given by 1 and -1 respectively. A value of 0 indicates no correlation.*

Feature scaling

In total the signal classifier was trained on 12 features: the four vector components $(p_{\mathrm{T}}, \eta, \phi, E)$ of the diphoton system and the leading photons detailed in Table 11.2.

Table 11.2 *Input features to neural network signal classifier.*

Description	Features
Transverse momentum	$p_{\mathrm{T},\gamma\gamma}$, $p_{\mathrm{T},\gamma1}$, $p_{\mathrm{T},\gamma2}$
Pseudorapidity	$\eta_{\gamma\gamma}$, $\eta_{\gamma1}$, $\eta_{\gamma2}$
Azimuthal angle	$\phi_{\gamma\gamma}$, $\phi_{\gamma1}$, $\phi_{\gamma2}$
Energy	$E_{\gamma\gamma}$, $E_{\gamma1}$, $E_{\gamma2}$

The classification uses a neural network which is sensitive to the scale of the features. Ensuring features are normalised to a similar scale prevents the model from being biased towards features with larger scales. Generally, scaling techniques divide the variable by some constant and therefore do not change the shape of the distribution. Different normalisation techniques, such as standardisation, were tested to determine the most suitable for the feature scaling. Robust scaling was chosen since it is more suitable for handling outliers in the

data.

Robust scaling is a normalisation technique that scales variables to the median and quantiles of the data. It is calculated as

$$x' = \frac{x - \text{median}(x)}{\text{IQR}(x)} \tag{11.1}$$

where $\text{IQR}(x) = \text{Q3} - \text{Q1}$ is the interquartile range of the feature and Q1 and Q3 are the first and third quartiles respectively [156]. Figure 11.5 shows a sample of input feature distributions after apply the robust scaling method.

The correlation matrix of the features is shown in Figure 11.6. As expected, the diphoton kinematics are correlated with the leading and subleading photon kinematics.

11.2.2 Neural network architecture

The neural network classifer was built using the Keras [157] package. The model is designed to classify events into three classes: (1) ggF; (2) $c\bar{c} \to H$; and (3) $uu, dd \to H$.

Table 11.3 *Neural network classifier architecture and hyperparemeters.*

Layers	Neurons	Activation function
Input layer	20	ReLU
Hidden layer	10	ReLU
Output layer	3	Sigmoid
Loss function		
Categorical cross-entropy		$L(\hat{y}, y) = -\sum_{i=1}^{C} y_i \log(\hat{y}_i)$
Optimiser		
Adam	learning rate	0.001

The model architecture is presented in Table 11.3. The number of neurons in the hidden layers were manually optimised. Since the model predicts three classes, the output layer must have three neurons. The neurons are connected such that each neuron in a given layer receives a weighted sum of neurons from the previous layer which is then transformed by an activation function.

The activation function in a neural network introduces non-linearity and therefore

allows the algorithm to learn complex patterns. The input and hidden layers both use the ReLU activation function defined as $f(x) = \max(0, x)$. Positive values are unchanged and negative values are replaced by zero. The output layer uses the sigmoid activation function, $f(x) = \frac{1}{1+e^{-x}}$, to ensure the output predicts a probability.

The loss function is defined to quantify how good the model predictions are. The goal is therefore to find the best weight parameters that minimise the loss function. Specifically designed for multi-class classification, the categorical cross-entropy loss function is used and defined as

$$L(\hat{y}, y) = -\sum_{i=1}^{C} y_i \log(\hat{y}_i), \tag{11.2}$$

where y_i is the true value, $\hat{y}_i$ is the prediction and C is the total number of classes [158]. In this case, the loss function measures the difference between the true class labels and the predicted probabilities in the classification task.

An optimiser is used to update the model weights and biases during training. The Adam [159] optimiser is used for this model.

Regularisation techniques are used to prevent overfitting. L2-regularisation is used in this model and prevents overfitting by penalising situations where the weights become too large.

Callback techniques are used to improve the training efficiency. Early stopping callback is applied to stop training if the loss has not improved within a defined number of training steps.

11.2.3 Model performance

The performance of the model was evaluated by comparing the accuracy and loss for the validation and training datasets as shown in Figure 11.7. An 80:20 split was used for training and validation. Both the accuracy and loss show good agreement between the training and validation datasets indicating the model is not overfitting. Since the model predicts three classes, an accuracy of 43% is an improvement on random guessing at 33%.

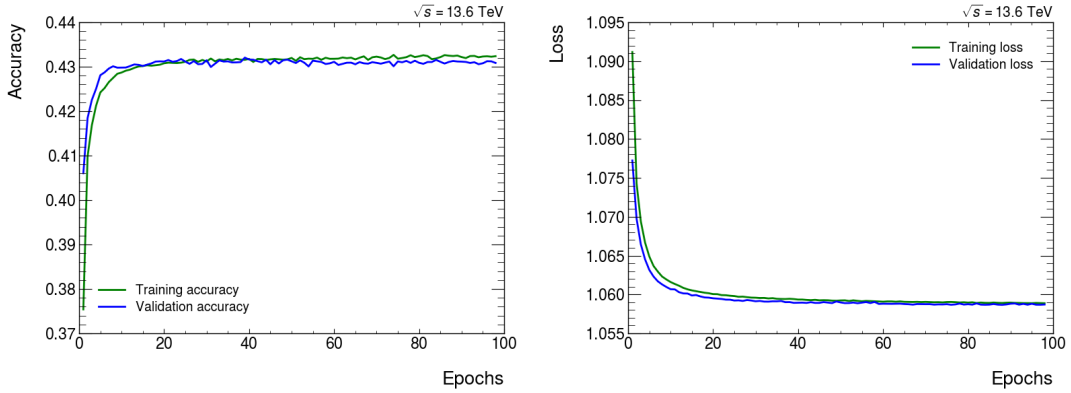

(a) *Validation and training accuracy* **(b)** *Validation and training loss*

Figure 11.7 *Performance metrics of the signal classifier for the training and validation datasets: (a) accuracy; and (b) loss.*

11.2.4 Defining orthogonal signal regions

Discriminant distributions are used to define three orthogonal signal regions. The discriminant is defined as the probability of a given event belonging to a particular class. Figure 11.8 presents the orthogonal discriminant distributions for each signal region. The orthogonal signal regions are defined using the discriminant cuts shown in Table 11.4. As demonstrated in Figure 11.8, the cuts on the discriminant are located where the signal and background intercept.

Table 11.4 *Discriminant cuts defined from the signal-background intersection of the discriminant distributions, shown in Figure 11.8, to create orthogonal signal regions. The discriminant distributions are orthogonal: events that fail the $\kappa_{u,d}$ cut enter the ggF distribution; events that fail both the $\kappa_{u,d}$ and ggF cuts enter the κ_c distribution.*

Signal region	Discriminant cut	Event selection
$\kappa_{u,d}$	$d_u > 0.5$	Pass d_u cut
ggF	$d_g > 0.56$	Fail d_u cut and pass d_g cut
κ_c	-	Fail d_u and d_g cuts

Figure 11.9 shows the confusion matrix for the orthogonal signal regions. In each predicted class, the largest fraction of events is from the corresponding true class as shown from the diagonal elements. The off-diagonal elements show misidentified events. The contributions from off-diagonal elements are greatest for the classification of $c\bar{c} \to H$ events. This is suggestive of limited separating power for $c\bar{c} \to H$ production from the other production modes as reflected in the discriminant distribution in Figure 11.8c.

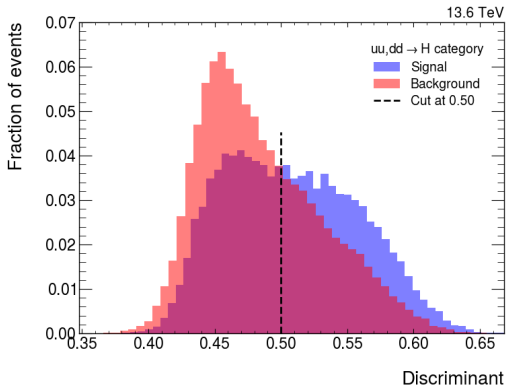

(a) *$\kappa_{u,d}$-enhanced signal region*

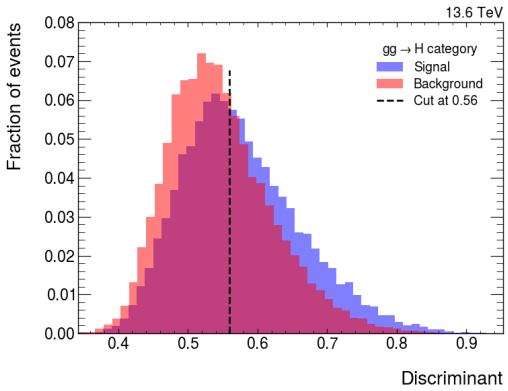

(b) *ggF-enhanced signal region*

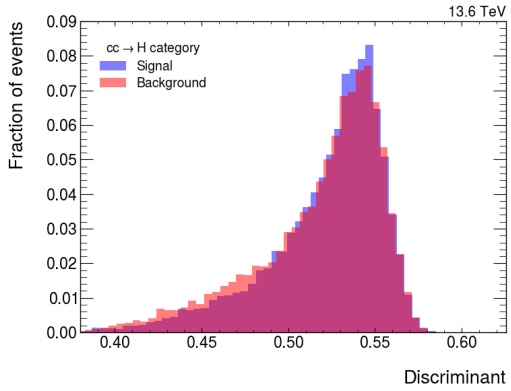

(c) *κ_c enhanced signal region*

Figure 11.8 *Discriminant distributions used to define orthogonal signal regions: (a) $\kappa_{u,d}$-enhanced; (b) ggF-enhanced; and (c) κ_c enhanced. The signal is the process corresponding to the signal region (e.g. $u\bar{u} \to H$) and the background is the sum of all other processes (e.g. $c\bar{c} \to H$ and ggF). Discriminant cuts are set at the signal-background intersection. The distributions are normalised according to fraction of events/x with (a) $x = 0.01$, (b) $x = 0.02$, and (c) $x = 0.01$.*

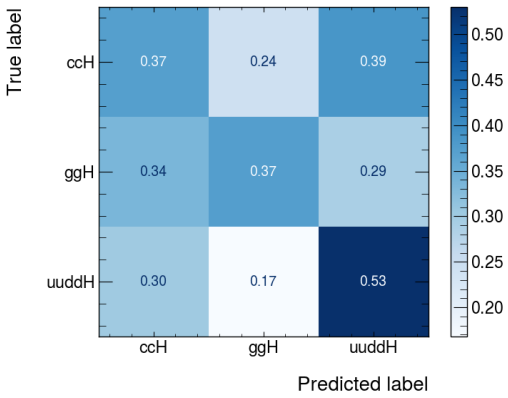

Figure 11.9 *Confusion matrix for the orthogonal signal regions.*

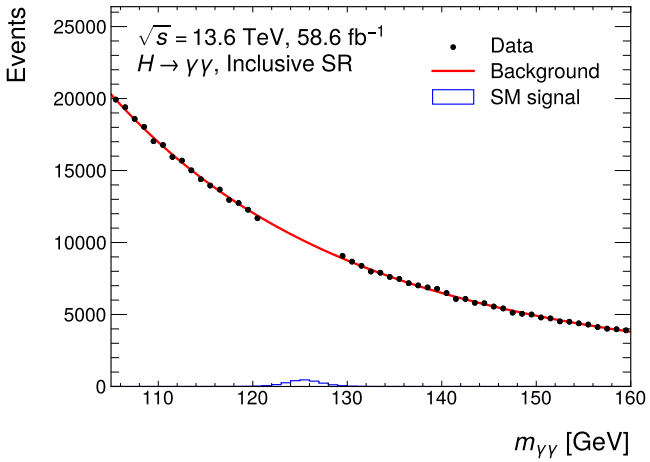

Figure 11.10 *Invariant mass distribution for the inclusive signal region. The data is blinded in the signal region and so the ggF MC sample is used to model the signal.*

11.3 Statistical analysis

The statistical analysis procedure is summarised in the following steps:

1. Use the $m_{\gamma\gamma}$ distribution for a given signal region to extract the signal and background yields.
2. Perform a counting experiment to compare the signal yield from the $m_{\gamma\gamma}$ distribution with hypothesised signal yields for different coupling modifier strengths.

The following sections explain each step in more detail.

11.3.1 Diphoton invariant mass distribution

The $m_{\gamma\gamma}$ distribution is used to extract the signal and background yields in the signal region. Due to this analysis being a proof-of-concept using pseudo-data (see Section 11.1.1), simplified signal and background extraction methods are used. Similarly, uncertainties from the Run 2 measurement are assumed.

Figure 11.10 shows the $m_{\gamma\gamma}$ distribution for the inclusive signal region. To extract the signal yield in the signal region, $121 < m_{\gamma\gamma} < 129\,\text{GeV}$, a cut and count method is applied to the ggF histogram. The ggF counts in the signal region are

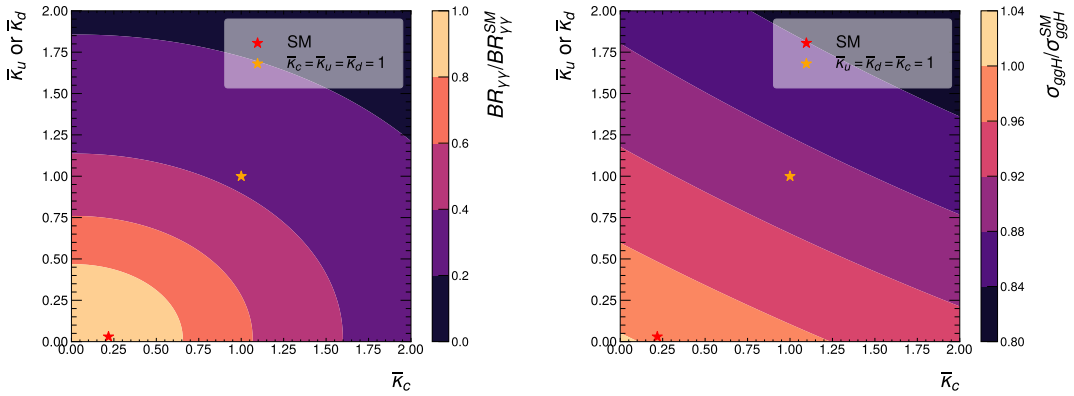

(a) *Branching ratio parameterisation* **(b)** *ggF cross-section parameterisation*

Figure 11.11 *Parameterisation of the (a) branching ratio and (b) ggF cross-section for the normalised up, down and charm quark coupling strength modifiers, $\bar{\kappa}_q = y_q/y_b^{SM}$. The red star shows the SM value for the charm Yukawa coupling. The orange star shows the value where the up, down and charm quark Yukawa couplings are equal to the bottom quark Yukawa coupling.*

summed to obtain the signal yield. To extract the background counts in the signal region, the continuum background distribution is fitted using an exponential function of a second-order polynomial in $m_{\gamma\gamma}$ given by Equation 8.1.

11.3.2 Counting experiment

To interpret the signal yield in terms of the Yukawa couplings, a counting experiment is performed. The signal yield in the pseudo-data is compared to the signal yield calculated for varying coupling strength modifiers.

The signal yield, introduced in Equation 3.13, is modelled using the Kappa Framework (see Section 3.5) as

$$N(\bar{\kappa}_c, \bar{\kappa}_u) = N_{\text{ggF}}(\bar{\kappa}_c, \bar{\kappa}_u) + N_{uu,dd\to H}(\bar{\kappa}_c, \bar{\kappa}_u) + N_{cc\to H}(\bar{\kappa}_c, \bar{\kappa}_u), \tag{11.3}$$

where $\bar{\kappa}_q = y_q/y_q^{\text{SM}}$ and N_{ggF}, $N_{uu,dd\to H}$ and $N_{cc\to H}$ are the signal yields for ggF, $uu, dd \to H$ and $c\bar{c} \to H$ processes respectively.

The normalisation effects introduced in Section 3.7.3 are considered in the signal yield parameterisation. The contour plots in Figure 11.11 illustrate the $H \to \gamma\gamma$ branching ratio and ggF cross-section parameterisation in the Kappa Framework

(see Table 3.4) in terms of $\bar{\kappa}_c$ and $\bar{\kappa}_u$. The plots highlight the effect of enhanced coupling modifiers on the branching ratio and cross-section, and ultimately the signal yield, compared to the SM values. The orange star represents the values where the up, down and charm quark Yukawa couplings are equal to the bottom quark coupling. Here, the branching ratio is significantly reduced to approximately 30% of the SM value. By comparison, the cross-section is only reduced to around 90% of the SM value.

A χ^2 fit is used to compare the signal yield in pseudo-data with the hypothesised signal yields for varying coupling strength modifiers. The χ^2 function is defined as

$$\chi^2 = \frac{(N_{\text{data}} - N_{\text{model}})^2}{\sigma^2_{\text{data}} + \sigma^2_{\text{sys}}}, \tag{11.4}$$

where N_{data} is the signal yield in pseudo-data and N_{model} is the signal yield for varying coupling strength modifiers. The uncertainty on the signal yield in pseudo-data is $\sigma_{\text{data}} = \sqrt{S+B}$. The systematic uncertainty, σ_{sys}, is assumed to be 6% from the previous Run 2 measurement in Table 8.2. To determine the goodness-of-fit, the p-value is obtained from the χ^2 test statistic as the probability of observing a χ^2 value greater than the observed value, $p = P(\chi^2 \geq \chi^2_{\text{obs}})$. The p-value is then used to determine the 68% (1σ) and 95% (2σ) confidence levels on the coupling strength modifiers.

11.4 Results

The constraints on the charm and light quark Yukawa couplings are presented in this section. Three different interpretations are presented:

1. **shape+XS+BR** interpretation accounting for shape, cross-section (XS) and branching ratio (BR) effects;
2. **shape+XS** interpretation accounting shape and cross-section effects, assuming the SM $H \to \gamma\gamma$ branching ratio; and
3. **BR-only** interpretation accounting for branching ratio effects, assuming SM cross-section values.

All three interpretations are used to search for beyond the SM effects that may result in enhanced Yukawa couplings.

The shape+XS+BR interpretation assumes SM structure with the Yukawa coupling affecting both the ggF cross-section and $H \to \gamma\gamma$ branching ratio. As a result, the best constraints on the Yukawa couplings are expected from this interpretation due to the combination of effects illustrated in Figure 11.11.

The shape+XS interpretation considers beyond the SM physics where a new particle may enhance the ggF production quark loop. Conversely, the BR-only interpretation targets scenarios in which a new particle may enhance only the $H \to \gamma\gamma$ quark loop. The two Higgs doublet model (2HDM) [160] is an example beyond the SM scenario where the Yukawa coupling affects the two quark loops separately.

11.4.1 Inclusive signal region measurement

The inclusive signal region, based on the diphoton fiducial region defined in Section 8.2.3, forms the baseline signal region in this Yukawa interpretation. The aim of combining the signal regions defined from the signal classifier is to improve on the single measurement in the inclusive signal region.

Table 11.5 *Expected limits on $\bar{\kappa}_c$ and $\bar{\kappa}_u$ for each interpretation at 68% and 95% confidence levels (CL).*

Interpretation	Signal region	$\lvert\,\bar{\kappa}\,\rvert$	Exp. 68% CL	Exp. 95% CL
shape+XS+BR	Inclusive	$\bar{\kappa}_u$	$0.00 + 0.55$	0.86
		$\bar{\kappa}_c$	$0.00 + 0.61$	0.89
	Combined	$\bar{\kappa}_u$	$0.00 + 0.53$	0.80
		$\bar{\kappa}_c$	$0.00 + 0.60$	0.87
shape+XS	Inclusive	$\bar{\kappa}_u$	$0.00 + 0.59$	0.87
		$\bar{\kappa}_c$	$0.00 + 2.36$	3.30
	Combined	$\bar{\kappa}_u$	$0.00 + 0.56$	0.82
		$\bar{\kappa}_c$	$0.00 + 2.25$	3.16
BR-only	Inclusive	$\bar{\kappa}_u$	$0.00 + 0.44$	0.63
		$\bar{\kappa}_c$	$0.00 + 0.63$	0.90
	Combined	$\bar{\kappa}_u$	$0.00 + 0.44$	0.63
		$\bar{\kappa}_c$	$0.00 + 0.61$	0.88

The expected exclusion limits for the charm and light quark Yukawa coupling modifiers are presented in Table 11.5. The key findings are:

1. the light quark couplings are less than the bottom quark coupling,

establishing the hierarchy predicted in the SM;

2. the constraints on the charm quark coupling are less stringent than the Run 2 results, as expected given the smaller dataset ($58.6\,\text{fb}^{-1}$ vs. $139\,\text{fb}^{-1}$); and

3. the constraints from the BR-only interpretation are the most stringent which is unexpected given the effects observed in Figure 11.11.

These observations are discussed further in the following sections.

11.4.2 Combined measurements

Compared to using a single, inclusive region, this thesis develops a strategy to constrain the quark couplings from three orthogonal signal regions: ggF-enhanced, $\kappa_{u,d}$-enhanced and κ_c-enhanced (see Section 11.2). The constraints on the couplings were obtained by combining the three regions using the least squares method [161]:

$$\chi^2 = \chi^2_{\text{ggF}} + \chi^2_{uu,dd\to H} + \chi^2_{cc\to H}. \tag{11.5}$$

In this method, independent measurements dominated by statistical uncertainty are assumed, which is the case for the analysis in this thesis. The systematic uncertainties across the three measurements are correlated; this, however, is neglected in the combination.

The two-dimensional expected exclusion limits are shown in Figure 11.12 for the different interpretations. Table 11.5 compares the expected exclusion limits for both the inclusive and combined measurements. In all interpretations, the combined measurement provides the best constraints on $\bar{\kappa}_u$ and $\bar{\kappa}_c$. The largest improvement occurs in the shape+XS+BR interpretation, yielding a $\sim$ 7% reduction in $\bar{\kappa}_u$ relative to the inclusive signal region.

Shape+XS+BR interpretation

The shape+XS+BR interpretation is comparable to the interpretation of the bottom and charm quark Yukawa couplings performed in the Run 2 $H \to \gamma\gamma$ measurement [7].

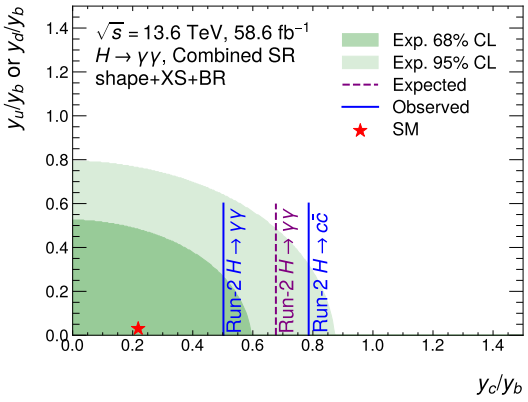

(a) *shape+XS+BR interpretation*

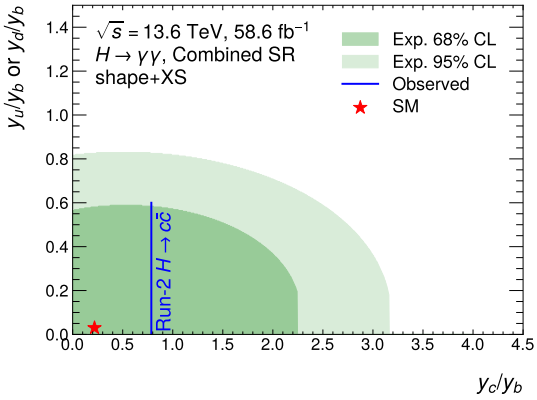

(b) *shape+XS interpretation*

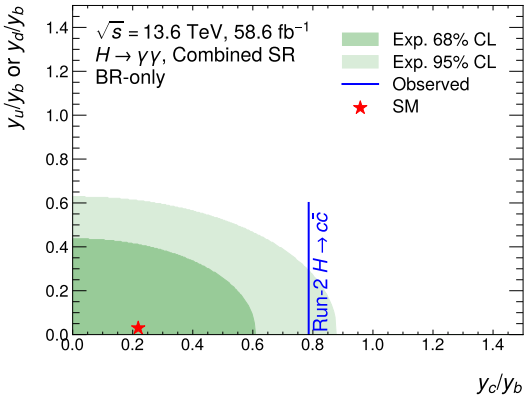

(c) *BR-only interpretation*

Figure 11.12 *2D expected limits on $\bar{\kappa}_c$ and $\bar{\kappa}_u$ using the (a) shape+XS+BR, (b) shape+XS and (c) BR-only interpretations for the combined measurement. Exclusion limits at 68% (dark green) and 95% (light green) confidence level (CL) are shown. The standard model prediction for $\bar{\kappa}_c$ is represented by the red star. The Run 2 expected (purple dashed line) and observed (blue solid line) constraints at 95% CL from Ref. [35] and Ref. [7] are shown. Both Run 2 analyses assume SM values for the light quark Yukawa couplings and so are not directly comparable to the results presented in this thesis.*

The expected exclusion limits on the coupling modifiers are

$$\begin{aligned} |\,\bar{\kappa}_u\,| &< 0.80, \\ |\,\bar{\kappa}_c\,| &< 0.87, \end{aligned} \tag{11.6}$$

at 95% confidence level. The combined results are an improvement on the single measurement in the inclusive signal region.

The expected and observed constraints at 95% confidence level are shown in Figure 11.12a for the Run 2 $H \to \gamma\gamma$ measurement. Since the exclusion limits presented in this thesis are determined from MC signal events, the expected Run 2 limits are a fair comparison. Better exclusion is found on $\bar{\kappa}_c$ for the Run 2 $H \to \gamma\gamma$ measurement; this is expected given the measurement was performed with $139\,\text{fb}^{-1}$ compared to the $58.6\,\text{fb}^{-1}$ used in this analysis. Likewise, the observed constraint on $\bar{\kappa}_c$ at 95% confidence level from direct $H \to c\bar{c}$ measurement [4] is more stringent than the result presented in this thesis.

Since both the first- and second-generation Yukawa couplings are found to be weaker than the third-generation, this technique is expected to confirm the SM prediction of a hierarchical structure in the Yukawa couplings at 95% confidence level.

Shape+XS interpretation

The constraints on $\bar{\kappa}_c$ in this interpretation do not add anything compared to the direct $H \to c\bar{c}$ measurement. The constraints on the light quark Yukawa coupling modifiers, however, are expected to still confirm the hierarchy of the first-generation Yukawa couplings at 95% confidence level.

BR-only interpretation

The most stringent constraints on the light quark Yukawa couplings are found in this interpretation. Table 11.6 summmarises the expected event composition for each production mode in the inclusive signal region, assuming $\bar{\kappa}_u = \bar{\kappa}_c = 1$. As expected from Figure 11.11, the shape+XS+BR interpretation exhibits the smallest ggF contribution due to the reduced branching ratio and ggF cross-section at enhanced coupling strengths. The production of $uu, dd \to H$, however, increases substantially which results in an overall higher cross-section and total

Table 11.6 *Expected composition of events for each production mode in the inclusive signal region considering each interpretation. The number of events is calculated using* $\mathcal{N} = \sigma(\kappa_q) \cdot \mathcal{L} \cdot \mathcal{B}_{\gamma\gamma}(\kappa_q) \cdot \epsilon$*, assuming* $\bar{\kappa}_c = \bar{\kappa}_u = 1$.

Interpretation	N_{ggF}	$N_{c\bar{c}\to H}$	$N_{u\bar{u},d\bar{d}\to H}$	N_{total}
shape+XS+BR	691	26	339	1056
shape+XS	1885	71	925	2881
BR-only	771	1	0	722

event yield compared to the BR-only interpretation. Consequently, the BR-only interpretation, with its lower total yield, leads to the tightest constraints on the light quark Yukawa couplings.

11.4.3 Individual measurements

The expected exclusion limits for the individual signal regions are shown in Table 11.7. The complete set of exclusion plots is provided in Appendix C. Table 11.8 presents the ggF signal and background yields in each signal region. Furthermore, the significance of the ggF signal is reported for each signal region with the ggF-enhanced region showing the highest significance.

11.4.4 Summary of assumptions

The results in this section were obtained under a number of assumptions, the most significant of which are summarised here. The $u\bar{u}, d\bar{d} \to H$ and $c\bar{c} \to H$ signal events were generated with NLO accuracy using MadGraph5_aMC@NLO and showered with Pythia. The evaluation of theoretical modelling uncertainties for these samples is left to further study. Furthermore, there are no NNLO predictions for $q\bar{q} \to H$ production at $\sqrt{s} = 13.6\,\text{TeV}$ readily available. For $c\bar{c} \to H$ production, the NNLO prediction at 13 TeV was extrapolated to 13.6 TeV using a scale factor derived from ggF cross-sections. For $u\bar{u} \to H$ and $d\bar{d} \to H$ production, the corresponding NLO cross-sections were extrapolated to NNLO using a NNLO/NLO scale factor, estimated from 13 TeV $c\bar{c} \to H$ production. The detector resolution effects were emulated with Rivet for these samples. The acceptance and efficiency for passing the baseline $H \to \gamma\gamma$ selection criteria are assumed to be identical to those for ggF production. Finally, the systematic

Table 11.7 *Expected limits on $\bar{\kappa}_c$ and $\bar{\kappa}_u$ in each separate signal region at 68% confidence level (CL). The best constraints for each interpretation are highlighted in bold.*

Interpretation	Signal region	$\lvert\bar{\kappa}\rvert$	Exp. 68% CL
shape+XS+BR	ggF-enhanced	$\bar{\kappa}_u$	**$0.00 + 0.63$**
		$\bar{\kappa}_c$	$0.00 + 0.82$
	$\kappa_{u,d}$-enhanced	$\bar{\kappa}_u$	$0.00 + 1.58$
		$\bar{\kappa}_c$	**$0.00 + 0.78$**
	κ_c-enhanced	$\bar{\kappa}_u$	$0.00 + 0.73$
		$\bar{\kappa}_c$	$0.00 + 0.82$
BR-only	ggF-enhanced	$\bar{\kappa}_u$	$0.00 + 0.60$
		$\bar{\kappa}_c$	$0.00 + 0.84$
	$\kappa_{u,d}$-enhanced	$\bar{\kappa}_u$	**$0.00 + 0.55$**
		$\bar{\kappa}_c$	**$0.00 + 0.78$**
	κ_c-enhanced	$\bar{\kappa}_u$	$0.00 + 0.59$
		$\bar{\kappa}_c$	$0.00 + 0.82$
shape+XS	ggF-enhanced	$\bar{\kappa}_u$	$0.00 + 0.93$
		$\bar{\kappa}_c$	$0.00 + 3.02$
	$\kappa_{u,d}$-enhanced	$\bar{\kappa}_u$	**$0.00 + 0.69$**
		$\bar{\kappa}_c$	$0.00 + 3.07$
	κ_c-enhanced	$\bar{\kappa}_u$	$0.00 + 0.83$
		$\bar{\kappa}_c$	**$0.00 + 2.84$**

Table 11.8 *SM ggF signal and background yield extracted from each signal region. The significance of the ggF signal is shown.*

Signal region	ggF yield	B yield	Significance ggF
Inclusive	2024	83207	7.0
ggF-enhanced	712	22354	4.7
$\kappa_{u,d}$-enhanced	631	30937	3.6
κ_c-enhanced	681	29051	4.0

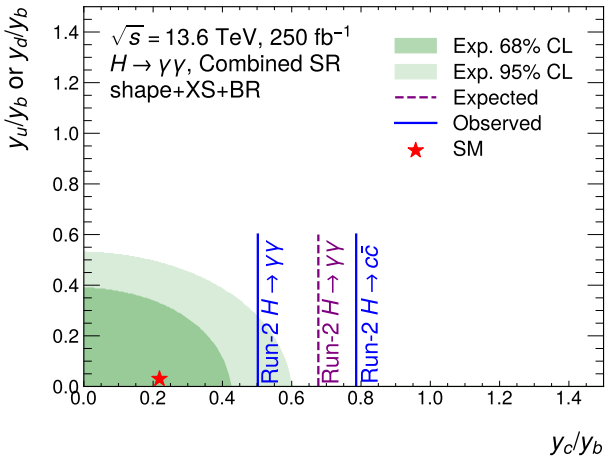

Figure 11.13 *Same as Figure 11.12 but for the full Run 3 dataset in the shape+XS+BR interpretation.*

uncertainty is assumed to be consistent with that of the Run 2 $H \to \gamma\gamma$ cross-section measurement.

11.5 Outlook to full Run 3 and HL-LHC

Figure 11.13 shows two-dimensional exclusion limits on $\bar{\kappa}_u$ and $\bar{\kappa}_c$ for the full Run 3 dataset. To extrapolate the expected constraints for the full Run 3 dataset, the Run 2 systematic uncertainties are assumed. The exclusion limits at 95% confidence level are summarised in Table 11.9. With the full Run 3 dataset, the expected exclusion on $\bar{\kappa}_c$ improves upon the expected Run 2 limit.

Table 11.9 *Expected constraints on the charm and light quark Yukawa couplings from the combined measurement at 95% confidence level (CL). Projected constraints are shown for the full Run 3 dataset.*

Dataset	$\mathcal{L}$ [fb^{-1}]	$\lvert\bar{\kappa}\rvert$	Exp. 95% CL
Partial Run 3	58.6	$\bar{\kappa}_u$	0.80
		$\bar{\kappa}_c$	0.87
Full Run 3	250	$\bar{\kappa}_u$	0.53
		$\bar{\kappa}_c$	0.60

In this analysis, the effects of the κ_s variation are indistinguishable from the κ_c variation. At the HL-LHC, $H \to c\bar{c}$ measurements are expected to constrain κ_c to within approximately 20% of the SM value [155], thus breaking the degeneracy. Taking advantage of a well-measured charm Yukawa coupling, the κ_c-enhanced

signal region could therefore be replaced with a κ_s-enhanced signal region. This technique would therefore provide additional information on the strange and light quark Yukawa couplings given a well-measured charm Yukawa coupling.

11.6 Comparison to other techniques

For Run 2, the CMS collaboration [40] probed the light quark Yukawa couplings searching for $H\gamma$ production in the $H \to 4l$ decay channel, as described in Section 3.6.2. The top and bottom quark Yukawa couplings are set to the SM values whilst the up, down, strange and charm quark Yukawa couplings are free-floating parameters. For the full $138\,\text{fb}^{-1}$ of the Run 2 dataset, the expected constraints on the light quark couplings are $-1.13 < \bar{\kappa}_u < 1.13$ and $-0.98 < \bar{\kappa}_d < 0.97$ at 95% confidence level. The technique presented in this thesis is therefore expected to provide more stringent constraints on the light quark Yukawa couplings compared to the CMS measurement.

Introduced in Section 3.6.2, both ATLAS [38] and CMS [39] collaborations have reported upper bounds on the rare $H \to \rho\gamma$ decay which is sensitive to the light quark Yukawa couplings. Summarised in Table 3.6, the current constraints on the light quark couplings are $-243 < 2\bar{\kappa}_u + \bar{\kappa}_d < 327$, derived from the search for $H \to \rho\gamma$. The technique presented in this thesis is expected to improve the constraints on the light quark Yukawa couplings by two orders of magnitude compared to the rare decay measurements.

11.7 Summary

This chapter presents the interpretation of charm and light quark Yukawa couplings in the $H \to \gamma\gamma$ measurement. The aim of this analysis is to develop a novel technique to constrain coupling strength modifiers. In addition to different initial state radiation effects observed between quark-initiated ($q\bar{q} \to H$) and gluon-initiated (ggF) Higgs production, this analysis exploits the distinct parton distribution function (PDF) effects of $u\bar{u} \to H$ and $d\bar{d} \to H$ production. To optimally use these effects simultaneously, a neural network classifier is designed to classify different Higgs production modes. The results show expected sensitivity to constrain the first- and second-generation Yukawa couplings to less

than the bottom quark coupling at 95% confidence level. In conclusion, when deployed to Run 3 data, the new technique presented in this chapter is expected to confirm the hierarchical structure of the Yukawa couplings as predicted in the SM. Furthermore, the new technique is expected to provide better constraints on the light quark Yukawa couplings compared to other experimental measurements.

Chapter 12

Conclusion

"This discovery has opened the door to the next generation of physics. It's not the end of the story; it's just the beginning."

Peter Higgs

Since the Higgs boson was discovered by the ATLAS and CMS collaborations in 2012, the LHC has pursued a rich programme of physics to study its properties. Using $58.6\,\text{fb}^{-1}$ of the partial Run 3 data from the ATLAS Experiment, this thesis presents an innovative approach to indirectly probe the Yukawa coupling to the light (up and down) quarks and the charm quark.

The work in this thesis consists of two parts. The first part focuses on the technical work involved in the development of the ATLAS trigger system for Run 3 data taking. A study of the High-Level Trigger strategy for events with B-mesons decaying to a pair of muons was performed. The trigger relies on track reconstruction within detector regions of interest (RoI) defined around the muon candidates. The aim of the study was to determine a RoI configuration that achieves the optimal compromise between trigger efficiency and tracking time. It was found that reducing the RoI width and merging the two muon RoIs into a single 'super RoI' reduces the tracking timing by 70% without compromising trigger efficiency. This optimised tracking approach has been adopted for the ATLAS Run 3 B-physics triggers. Furthermore, development of the new web-based Trigger Rate Presenter dashboard used for live rate monitoring in the ATLAS control room is presented.

The second part of this thesis builds upon the existing Run 2 $H \to \gamma\gamma$ cross-section measurements. This thesis validated the available 2022+2023 Run 3 dataset, the corresponding simulated samples and software used in the developing Run 3 analysis. The work in this thesis demonstrates that the data and simulated samples under validation are in good agreement with the reference. Furthermore, the modelling of the simulated $H \to \gamma\gamma$ signal was validated for different regions of phase space, sensitive to different Higgs production modes, used in the cross-section measurement.

A new development in this thesis is the use of machine learning to enhance the sensitivity to the charm and light quark Yukawa couplings in the $H \to \gamma\gamma$ measurement. Exploited in Run 2, the sensitivity to quark couplings comes from the difference between quark-initiated ($q\bar{q} \to H$) and gluon-initiated (ggF) Higgs boson production. The measurement presented in this thesis, for the first time, also exploits the distinct parton distribution functions of the first-generation up and down quarks and their impact on the kinematics of $u\bar{u} \to H$ and $d\bar{d} \to H$ events. To optimally use these effects simultaneously, a neural network classifier is designed to classify different Higgs production modes. The expected constraints on the light (assuming $\bar{\kappa}_u = \bar{\kappa}_d$) and charm ($\bar{\kappa}_c$) quark Yukawa coupling modifiers

are about:

$$|\bar{\kappa}_u| < 0.8, \qquad (12.1)$$
$$|\bar{\kappa}_c| < 0.9,$$

at 95% confidence level. This would probe the hierarchy of the quark Yukawa couplings as predicted by the Standard Model, constraining the first- and second-generation couplings below the third-generation bottom quark coupling. Furthermore, this new technique is expected to provide better constraints on the light quark Yukawa couplings compared to existing experimental measurements.

The interaction between the Higgs boson and fermions is unique in the Standard Model as the only coupling directly proportional to the fermion mass. This thesis demonstrates a new technique which will be able to show the dependence of the Yukawa coupling on the mass of the quark. This is crucial for understanding the Higgs boson and, ultimately, how fundamental particles acquire mass.

Appendix A

Rejecting other Higgs production modes

The focus of this analysis is on Higgs production modes that are sensitive to the charm and light quark Yukawa couplings. All other production modes are considered background and are reduced by applying additional cuts to the data.

Table A.1 *Number of events passing selection criteria to remove unwanted production modes: VBF, VH, and $t\bar{t}H$. These production modes have all been measured to at least 5σ experimentally which corresponds to a 20% experimental uncertainty on the signal yield as reflected in the table. $\Delta S'/S$ is included to show the impact of the uncertainty on the signal yield where S is the ggF signal and S' includes VBF, VH, and $t\bar{t}H$.*

Process	Before		After	
	Events	Composition [%]	Events	Composition [%]
ggF	2308	88.7	2025	91.8
VBF	182 ± 36	7.0	107 ± 21	4.9
VH	87 ± 17	3.3	64 ± 13	2.9
$t\bar{t}H$	26 ± 5	1.0	9 ± 2	0.4
$\Delta S'/S$		1.7%		1.2%

Section 8.2.2 introduced the fiducial subregions of phase space which are sensitive to specific Higgs production modes. The cuts used to define these subregions are inverted here to reduce these production modes. Table A.1 shows the number of events passing the selection criteria to reduce VBF, VH and $t\bar{t}H$ contributions.

Reducing the contributions from VBF, VH and $t\bar{t}H$ production modes increases the purity of the signal peak in the $m_{\gamma\gamma}$ distribution. The remaining contributions from these production modes, however, must be subtracted from the signal yield which adds a source of uncertainty. VBF, VH and $t\bar{t}H$ production have all been measured to at least 5σ experimentally [3]. This corresponds to a 20% experimental uncertainty on the signal yield from these production modes as reflected in Table A.1. The theoretical uncertainties associated with these production modes, shown in Table 3.1, are small compared to the experimental uncertainties.

Assuming the dominant experimental uncertainty, the uncertainty on the signal yield from VBF, VH and $t\bar{t}H$ production modes is reduced from approximately 2% before the cuts and 1% after the cuts.

Appendix B

Background rejection neural network

This appendix introduces a background rejection neural network designed to distinguish between the Higgs boson signal and background processes. The classifier identifies two binary classes defined as follows:

1. **ggF signal**: the dominant Higgs boson production mode; and
2. **$\gamma\gamma$ + jets background**: the dominant background process.

The aim of this binary classifier is to reject the dominant background process and enhance the sensitivity to the Higgs boson signal.

Simulated data

Table B.1 *Samples used to train the background rejection classifier. The pileup, $\langle\mu\rangle$ = 51, corresponds to 2023 data taking.*

Process	Pileup $\langle\mu\rangle$	Generator	Accuracy	Parton shower
$gg \to H$	51	POWHEG	NNLO	PYTHIA
$\gamma\gamma$+jets		SHERPA		SHERPA

The signal samples used to train the background rejection classifier are summarised in Table B.1. In contrast to the signal classifer, both samples include detector effects.

Validation of these samples is discussed in Chapter 9. The samples were produced using the 2022+23 SW. Given the known bug in the jet collection for this software version, jet features were not used in this model.

Feature selection

The background rejection classifier was trained on eight features using four vector information of the leading and subleading photons. The features are listed in Table B.2. To remove any dependence on the diphoton mass, the relative transverse momentum and energy were used.

Table B.2 *Features used in training the background rejection neural network. The relative p_T and E are used to remove any dependence on the diphoton mass.*

Description	Features
Relative transverse momentum	$\frac{p_{\mathrm{T},\gamma 1}}{m_{\gamma\gamma}}$, $\frac{p_{\mathrm{T},\gamma 2}}{m_{\gamma\gamma}}$
Pseudorapidity	$\eta_{\gamma 1}$, $\eta_{\gamma 2}$
Azimuthal angle	$\phi_{\gamma 1}$, $\phi_{\gamma 2}$
Relative energy	$\frac{E_{\gamma 1}}{m_{\gamma\gamma}}$, $\frac{E_{\gamma 2}}{m_{\gamma\gamma}}$

The same robust scaling method was used to normalise the input features as described in Section 11.2.1. Figure B.1 shows the eight input feature distributions after applying the robust scaling method.

Neural network architecture

The architecture of the background rejection classifier is shown in Table B.3. The number of layers and neurons were manually optimised. The same optimiser, regularisation and callback techniques as the signal classifier described in Section 11.2.2 were chosen.

Table B.3 *Background rejection neural network architecture.*

Layers	Neurons	Activation function
Input layer	16	ReLU
Hidden layer	8	ReLU
Output layer	1	Sigmoid

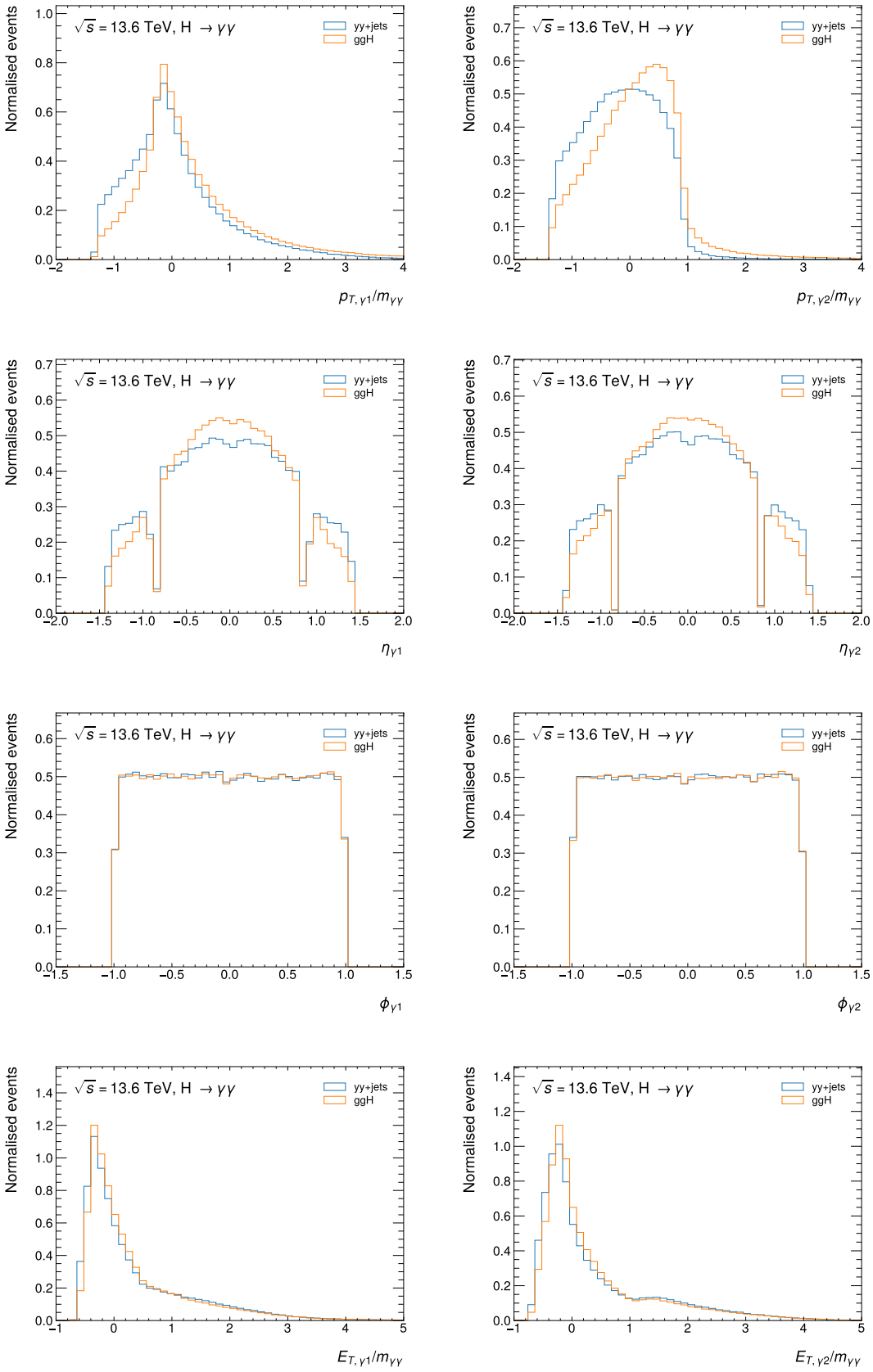

Figure B.1 *Normalised input feature distributions after applying the robust scaling method used to train the background rejection classifier.*

Since background rejection is a binary classification problem, the binary cross-entropy loss function was used. It is given by the equation

$$L(\hat{y}, y) = -\frac{1}{N}\sum_{i=1}^{N}\left(y_i \log(\hat{y}_i) + (1 - y_i)\log(1 - \hat{y}_i)\right), \tag{B.1}$$

where N is the number of samples, y_i is the true value and $\hat{y}_i$ is the prediction.

Model performance

The performance of the background rejection classifier was evaluated by comparing the accuracy and loss for the validation and training datasets as shown in Figure B.2. A 70:30 split was used for training and validation. The accuracy and loss show good agreement between the training and validation datasets indicating the model is not overfitting. Furthermore, the ROC curve plotting the true positive rate against the false positive rate is shown in Figure B.2c. The area under the curve is 65% which is an improvement on random guessing at 50%.

Four signal regions are defined for the background rejection classifier. The first is the inclusive signal region and the remaining are the three signal regions defined in the signal classifier: ggF-enhanced, $\kappa_{u,d}$-enhanced and κ_c-enhanced.

The discriminant, defined as the probability of an event belonging to a given class, is used to find a cut that maximises the significance in each signal region. The significance [162] is determined as

$$\text{Significance} = \sqrt{2 \cdot \left((S + B)\log\left(1 + \frac{S}{B}\right) - S\right)}, \tag{B.2}$$

where S and B are the number of signal and background events respectively. The significance can be approximated as $S/\sqrt{B}$ for small S/B. Figure B.3 shows the discriminant distributions for each signal region.

The optimised discriminant cuts are shown in Table B.4 along with the signal and background efficiencies passing the cuts. The $\kappa_{u,d}$-enhanced signal region has the worst performance in separating signal and background events with a 6.1% improvement in S/B. This corresponds to a 0.9% improvement in the significance. The highest improvement in the significance is 1.8% for the inclusive signal region which has a negligible impact on the sensitivity to the Yukawa couplings.

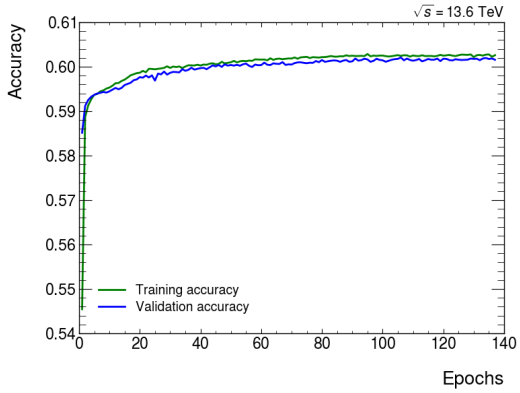

(a) *Validation and training accuracy*

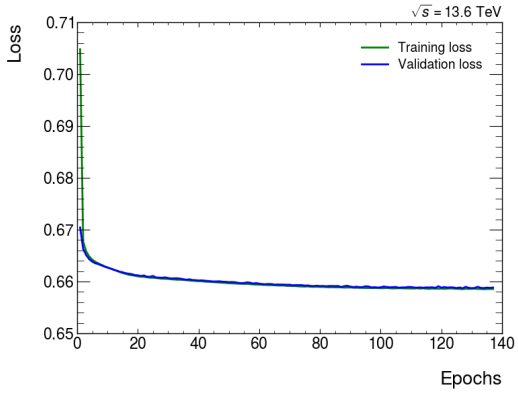

(b) *Validation and training loss*

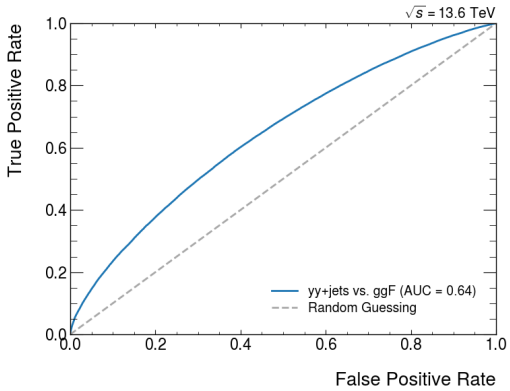

(c) *Training ROC curve*

Figure B.2 *Performance metrics of the background rejection classifer: (a) validation and training accuracy; (b) validation and training loss; and (c) training ROC curve plotting the true positive rate against the false positive rate.*

Table B.4 *Discriminant cuts for the background rejection classifier for each signal region: inclusive, ggF-enhanced, $\kappa_{u,d}$-enhanced and κ_c-enhanced. The cuts were optimised by maximising the significance. The signal (S) and background (B) efficiencies passing the optimised cuts are shown.*

Signal region	Cut	S efficiency	B efficiency	Δ(S/B)	$\Delta(S/\sqrt{B})$
Inclusive	0.35	92.4%	82.3%	12.0%	1.8%
ggF-enhanced	0.49	87.2%	74.0%	17.8%	1.4%
$\kappa_{u,d}$-enhanced	0.34	95.9%	90.4%	6.1%	0.9%
κ_c-enhanced	0.36	94.3%	87.6%	7.6%	0.8%

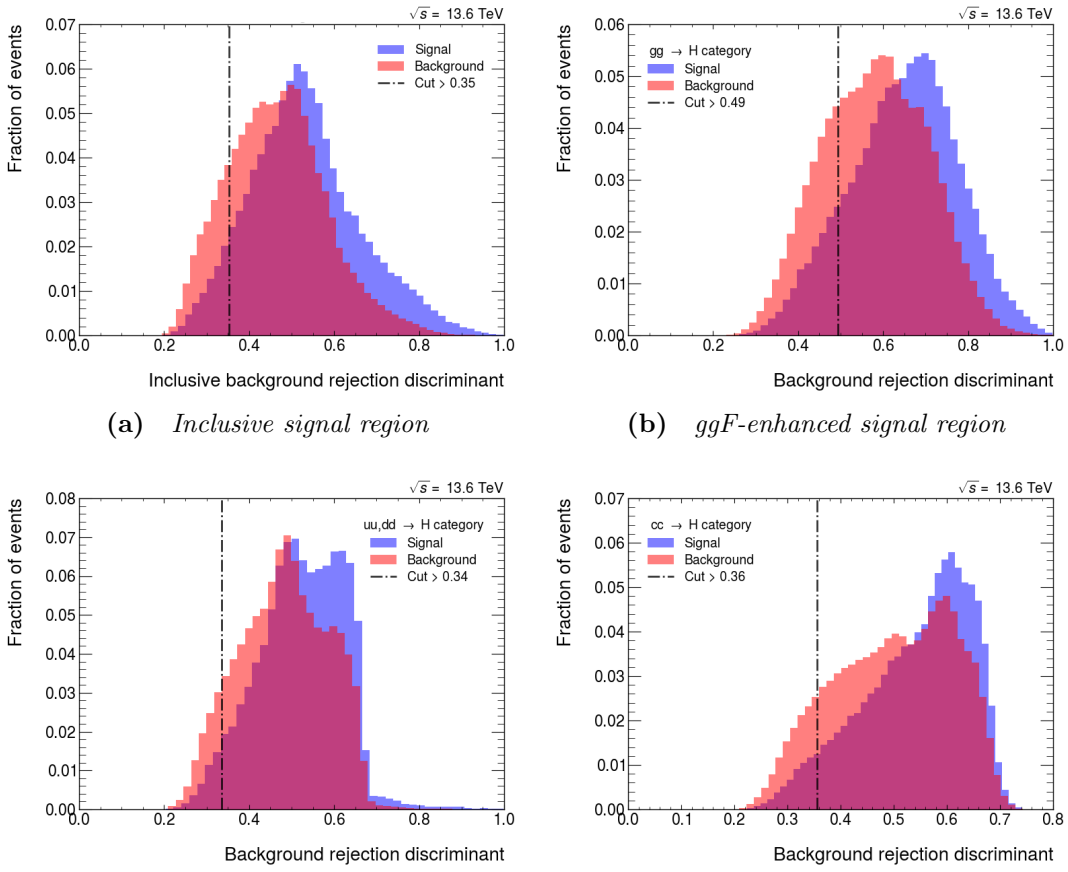

(a) *Inclusive signal region* **(b)** *ggF-enhanced signal region*

(c) *$\kappa_{u,d}$-enhanced signal region* **(d)** *κ_c-enhanced signal region*

Figure B.3 *Discriminant distributions for the background rejection classifier in the following signal regions: (a) inclusive; (b) ggF-enhanced; (c) $\kappa_{u,d}$-enhanced; and (d) κ_c-enhanced. The optimised cuts are determined by maximising the significance.*

Appendix C

Individual signal region plots

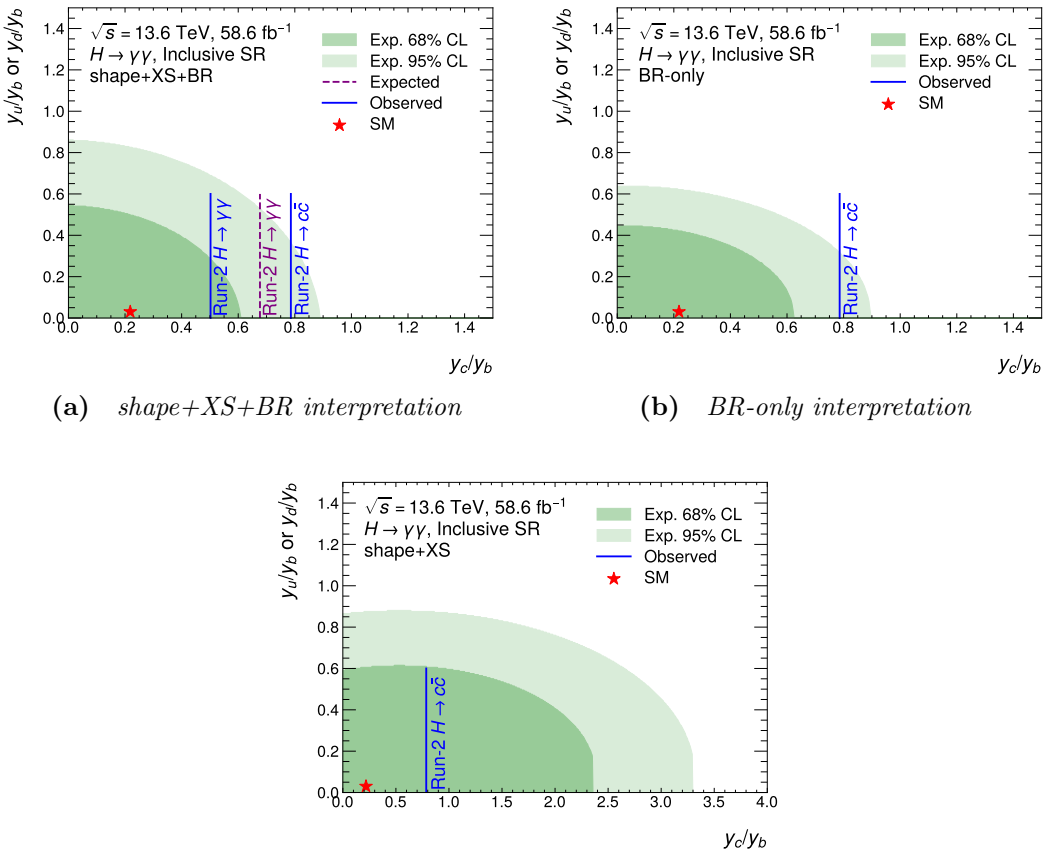

(a) *shape+XS+BR interpretation* **(b)** *BR-only interpretation*

(c) *shape+XS interpretation*

Figure C.1 *2D expected limits on $\bar{\kappa}_c$ and $\bar{\kappa}_u$ using the (a) shape+XS+BR, (b) BR-only and (c) shape+XS interpretations in the inclusive signal region.*

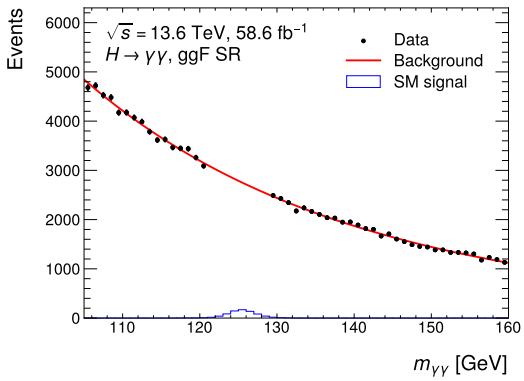

Figure C.2 *Invariant mass distribution for the ggF signal region.*

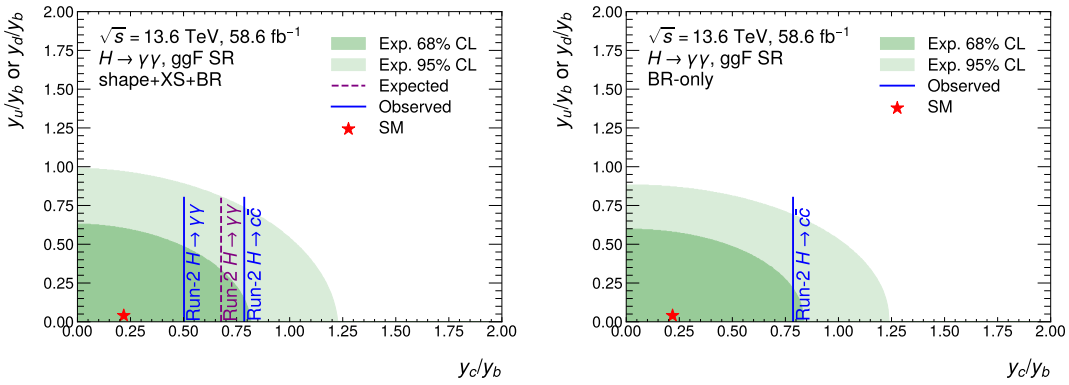

(a) *shape+xs+BR interpretation* **(b)** *BR-only interpretation*

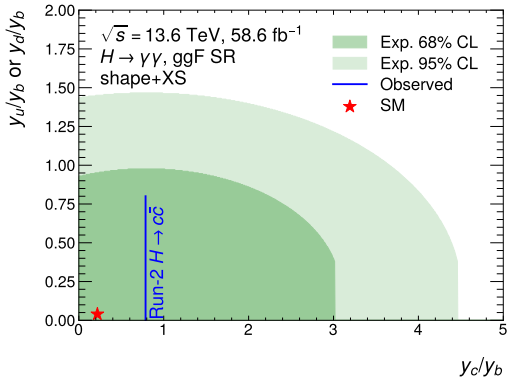

(c) *shape+xs interpretation*

Figure C.3 *2D expected limits on $\bar{\kappa}_c$ and $\bar{\kappa}_u$ using the (a) shape+xs+BR, (b) BR-only and (c) shape+xs interpretations in the ggF signal region.*

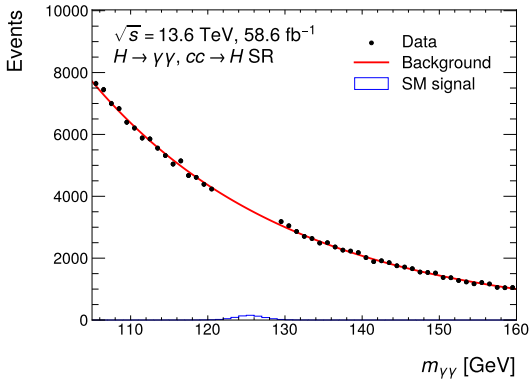

Figure C.4 *Invariant mass distribution for the κ_c signal region.*

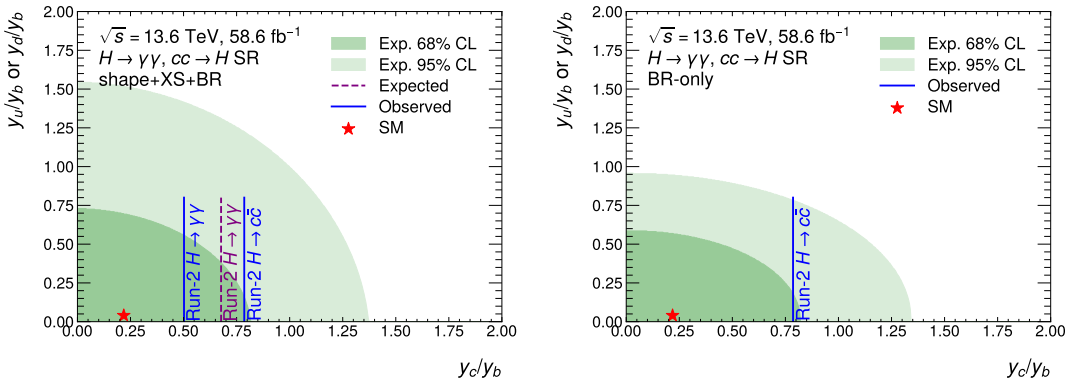

(a) *shape+xs+BR interpretation* **(b)** *BR-only interpretation*

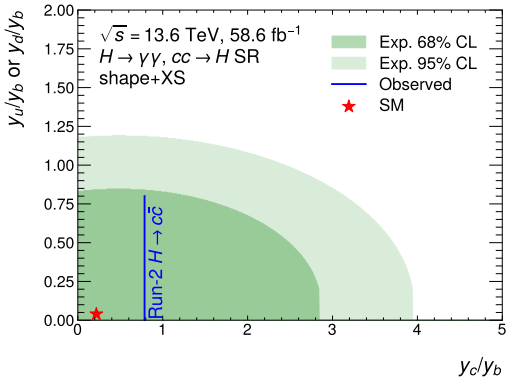

(c) *shape+xs interpretation*

Figure C.5 *2D expected limits on $\bar{\kappa}_c$ and $\bar{\kappa}_u$ using the (a) shape+xs+BR, (b) BR-only and (c) shape+xs interpretations in the κ_c-enhanced signal region.*

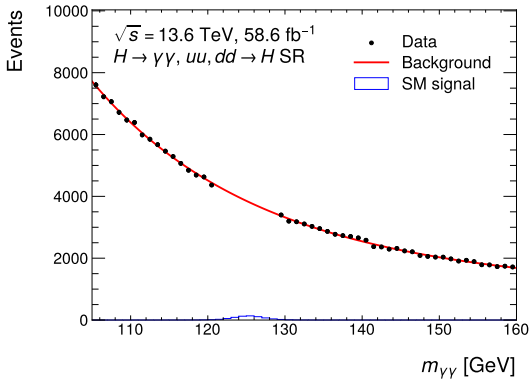

Figure C.6 *Invariant mass distribution for the $\kappa_{u,d}$ signal region.*

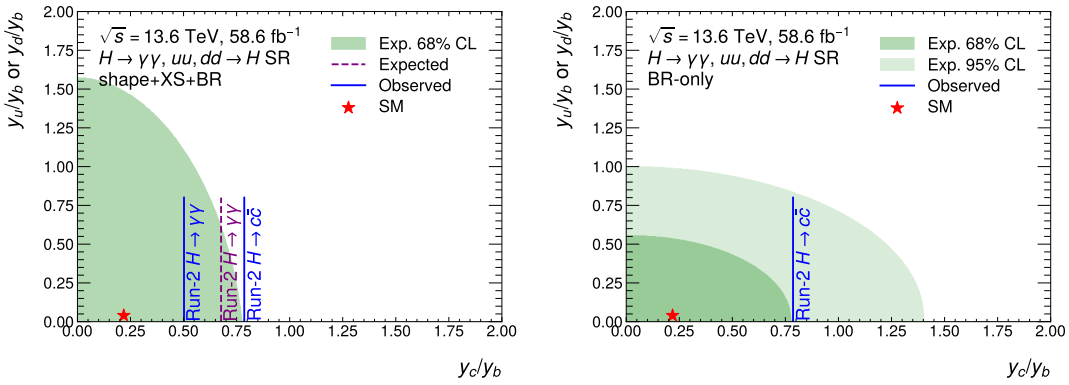

(a) *shape+xs+BR interpretation* **(b)** *BR-only interpretation*

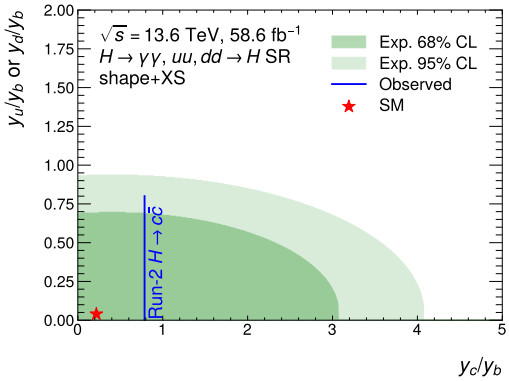

(c) *shape+xs interpretation*

Figure C.7 *2D expected limits on $\bar{\kappa}_c$ and $\bar{\kappa}_u$ using the (a) shape+xs+BR, (b) BR-only and (c) shape+xs interpretations in the $\kappa_{u,d}$ -nhanced signal region.*

Appendix D

ECFA ECR Panel

During my PhD, I was elected as a member to the European Committee for Future Accelerators (ECFA) Early-Career Researchers (ECR) Panel [163]. The ECFA ECR Panel represents the interests of young scientists in the field in Europe. My mandate lasted for two years, from January 2023 to December 2024, and the summary of the panel's activities during 2023 is presented in Ref. [164].

During my time on the panel, I contributed to the equality and diversity working group and was an analyser and editor of the survey report presented in Ref. [165].

As part of the UK representation on the ECFA ECR Panel, I helped organise the UK Future Collider Town Hall in July 2023, aimed at engaging the UK ECR community in discussions about the future of particle physics. A report on this event is presented in Ref. [166].

Additionally, I was on the organising panel for a careers event for ECRs in experimental high-energy physics. Based on feedback from the ECR survey, the event was designed to provide information on various career paths available to ECRs in the field.

Finally, I contributed to the UK input for the 2026 European Strategy for Particle Physics Update by participating in the organisation of the UK drafting efforts as part of the ECR team.

Bibliography

[1] ATLAS Collaboration. Observation of a new particle in the search for the Standard Model Higgs boson with the ATLAS detector at the LHC. *Physics Letters B*, 716(1), 2012, arXiv:1207.7214.

[2] CMS Collaboration. Observation of a new boson at a mass of 125 GeV with the CMS experiment at the LHC. *Physics Letters B*, 716(1), 2012, arXiv:1207.7235.

[3] ATLAS Collaboration. A detailed map of Higgs boson interactions by the ATLAS experiment ten years after the discovery. *Nature*, 607(7917), 2022, arXiv:2207.00092.

[4] ATLAS Collaboration. Direct constraint on the Higgs–charm coupling from a search for Higgs boson decays into charm quarks with the ATLAS detector. *The European Physical Journal C*, 82(8), 2022, arXiv:2201.11428.

[5] CMS Collaboration. Search for Higgs boson decay to a charm quark-antiquark pair in proton-proton collisions at $\sqrt{s} = 13$ TeV. *Physical Review Letters*, 131(6), 2022, arXiv:2205.05550.

[6] A. Cerri and V. V. Gligorov and S. Malvezzi and others. Opportunities in Flavour Physics at the HL-LHC and HE-LHC. 2019, arXiv:1812.07638.

[7] ATLAS Collaboration. Measurements of the Higgs boson inclusive and differential fiducial cross-sections in the diphoton decay channel with pp collisions at $\sqrt{s} = 13$ TeV with the ATLAS detector. *Journal of High Energy Physics*, 2022(8), 2022, arXiv:2202.00487.

[8] C. Burgard. Example: Standard model of physics. https://texample.net/tikz/examples/model-physics/. Accessed: 22-10-2024.

[9] M. E. Peskin and D. V. Schroeder. *An Introduction to Quantum Field Theory*. Addison-Wesley, 1995.

[10] R. P. Feynman. Space-time approach to Quantum Electrodynamics. *Physical review*, 76(6), 1949.

[11] H. Fritzsch, M. Gell-Mann, and H. Leutwyler. Advantages of the Color Octet Gluon Picture. *Physics Letters B*, 47(4), 1973.

[12] H. Fritzsch and M. Gell-Mann. Current Algebra: Quarks and What Else?, 2002, arXiv:hep-ph/0208010.

[13] S. L. Glashow. Towards a unified theory: Threads in a tapestry. *Reviews of Modern Physics*, 52(3), 1980.

[14] A. Salam. Gauge unification of fundamental forces. *Reviews of Modern Physics*, 52(3), 1980.

[15] S. Weinberg. Conceptual foundations of the unified theory of weak and electromagnetic interactions. *Reviews of Modern Physics*, 52(3), 1980.

[16] P. W. Higgs. Broken symmetries and the masses of gauge bosons. *Physical review letters*, 13(16), 1964.

[17] F. Englert and R. Brout. Broken symmetry and the mass of gauge vector mesons. *Physical review letters*, 13(9), 1964.

[18] J. Riebesell. Higgs Potential. https://tikz.net/higgs-potential/. Accessed: 24-02-2025.

[19] S. Bailey, T. Cridge, L. A. Harland-Lang, et al. Parton distributions from LHC, HERA, Tevatron and fixed target data: MSHT20 PDFs. *The European Physical Journal C*, 81(4), 2021, arXiv:2012.04684.

[20] A. Buckley, C. White, and M. White. *Practical collider physics*. IOP Publishing, Bristol, 2021.

[21] A. Karlberg, J. Malcles, B. Mistlberger, et al. Ad interim recommendations for the Higgs boson production cross sections at $\sqrt{s} = 13.6$ TeV. 2024, arXiv:2402.09955.

[22] D. de Florian, C. Grojean, F. Maltoni, et al. Handbook of LHC Higgs Cross Sections: 4. Deciphering the Nature of the Higgs Sector. 2017, arXiv:1610.07922.

[23] M. Bonvini, A. S. Papanastasiou, and F. J. Tackmann. Matched predictions for the $b\bar{b}H$ cross section at the 13 TeV LHC. *Journal of High Energy Physics*, 2016(10), 2016, arXiv:1605.01733.

[24] R. V. Harlander. Higgs production in heavy-quark annihilation through next-to-next-to-leading order QCD. *The European Physical Journal C*, 76(5), 2016, arXiv:1512.04901.

[25] S. Heinemeyer, C. Mariotti, G. Passarino, et al. Handbook of LHC Higgs Cross Sections: 3. Higgs Properties: Report of the LHC Higgs Cross Section Working Group. 2013, arXiv:1307.1347.

[26] J. Alwall, R. Frederix, S. Frixione, et al. The automated computation of tree-level and next-to-leading order differential cross sections, and their matching to parton shower simulations. *Journal of High Energy Physics*, 2014(7), 2014, arXiv:1405.0301.

[27] S. Navas, C. Amsler, T. Gutsche, et al. Review of particle physics. *Phys. Rev. D*, 110(3), 2024.

[28] M. Thomson. *Modern particle physics*. Cambridge University Press, 2013.

[29] ATLAS Collaboration and CMS Collaboration. Combined Measurement of the Higgs Boson Mass in pp Collisions at $\sqrt{s} = 7$ and 8 TeV with the ATLAS and CMS Experiments. *Physical Review Letters*, 114(19), 2015, arXiv:1503.07589.

[30] A. David, A. Denner, M. Duehrssen, et al. LHC HXSWG interim recommendations to explore the coupling structure of a Higgs-like particle. 2012, arXiv:1209.0040.

[31] ATLAS Collaboration. Measurement of the properties of Higgs boson production at $\sqrt{s} = 13$ TeV in the $H \to \gamma\gamma$ channel using 139 fb^{-1} of pp collision data with the ATLAS experiment. *Journal of High Energy Physics*, 2023(7), 2023, arXiv:2207.00348.

[32] Y. Soreq, H. X. Zhu, and J. Zupan. Light quark Yukawa couplings from Higgs kinematics. *Journal of High Energy Physics*, 2016(12), 2016, arXiv:1606.09621.

[33] G. Aad, B. Abbott, D. C. Abbott, et al. A search for the dimuon decay of the Standard Model Higgs boson with the ATLAS detector. *Physics Letters B*, 812, 2021, arXiv:2007.07830.

[34] CMS Collaboration. Evidence for Higgs boson decay to a pair of muons. *Journal of High Energy Physics*, 2021(1), 2021, arXiv:2009.04363.

[35] ATLAS Collaboration. Measurements of WH and ZH production with Higgs boson decays into bottom quarks and direct constraints on the charm Yukawa coupling in 13 TeV pp collisions with the ATLAS detector. 2024, arXiv:2410.19611.

[36] König, M. and Neubert, M. Exclusive radiative Higgs decays as probes of light-quark Yukawa couplings. *Journal of High Energy Physics*, 2015(8), 2015, arXiv:1505.03870.

[37] Kagan, A. L. and Perez, G. and Petriello, F. and Soreq, Y. and Stoynev, S. and Zupan, J. Exclusive Window onto Higgs Yukawa Couplings. *Physical Review Letters*, 114(10), 2015, arXiv:1406.1722.

[38] ATLAS Collaboration. Search for exclusive Higgs and Z boson decays to $\phi\gamma$ and $\rho\gamma$ with the ATLAS detector. *Journal of High Energy Physics*, 2018(7), 2018, arXiv:1712.02758.

[39] CMS Collaboration. Search for decays of the 125 GeV Higgs boson into a Z boson and a ρ or ϕ meson. *Journal of High Energy Physics*, 2020(11), 2020, arXiv:2007.05122.

[40] CMS Collaboration. Search for γH production and constraints on the Yukawa couplings of light quarks to the Higgs boson, 2025, arXiv:2502.05665.

[41] ATLAS Experiment Public Results: Some Displays of Candidate Events Selected in Higgs Search Analyses. https://twiki.cern.ch/twiki/bin/view/AtlasPublic/EventDisplaysFromHiggsSearches. Accessed: 2022-05-23.

[42] F. Bishara, U. Haisch, P. F. Monni, and E. Re. Constraining Light-Quark Yukawa Couplings from Higgs Distributions. *Physical Review Letters*, 118(12), 2017, arXiv:1606.09253.

[43] E. Mobs. The CERN accelerator complex in 2019. https://cds.cern.ch/record/2684277, 2019.

[44] O. S. Brüning, P. Collier, P. Lebrun, et al. LHC Design Report. Technical report, CERN, 2004, CERN-2004-003-V-1.

[45] L. Evans. The Large Hadron Collider. *New Journal of Physics*, 9(9), 2007.

[46] ATLAS Collaboration. Operation of the ATLAS trigger system in Run 2. *Journal of Instrumentation*, 15(10), 2020, arXiv:2007.12539.

[47] ATLAS Collaboration. The ATLAS experiment at the CERN Large Hadron Collider. *Journal of instrumentation*, 3(08), 2008.

[48] CMS Collaboration. The CMS experiment at the CERN LHC. *Journal of instrumentation*, 3(08), 2008.

[49] A. A. Alves Jr, L. M. Andrade Filho, A. F. Barbosa, et al. The LHCb detector at the LHC. *Journal of instrumentation*, 3(08), 2008.

[50] K. Aamodt, A. A. Quintana, R. Achenbach, et al. The ALICE experiment at the CERN LHC. *Journal of Instrumentation*, 3(08), 2008.

[51] G. Arduini, V. Baglin, H. Bartosik, et al. LHC Upgrades in preparation of Run 3. *JINST*, 19(05), 2024.

[52] O. Aberle, I. Béjar Alonso, O. Brüning, et al. High-Luminosity Large Hadron Collider (HL-LHC). Technical report, CERN, 2020, CERN-2020-010.

[53] Public ATLAS Luminosity Results for Run-3 of the LHC. https://twiki.cern.ch/twiki/bin/view/AtlasPublic/LuminosityPublicResultsRun3. Accessed: 06-03-2024.

[54] P. Grafström and W. Kozanecki. Luminosity determination at proton colliders. *Progress in particle and nuclear physics*, 81, 2015.

[55] ATLAS Collaboration. The ATLAS Experiment at the CERN Large Hadron Collider: A Description of the Detector Configuration for Run 3. *Journal of Instrumentation*, 19(05), 2023, arXiv:2305.16623.

[56] ATLAS Collaboration. ATLAS: technical proposal for a general-purpose pp experiment at the Large Hadron Collider at CERN. Technical report, CERN, 1994, CERN-LHCC-94-43; LHCC-P-2.

[57] ATLAS Collaboration. ATLAS detector and physics performance. Technical report, CERN, 1999, CERN-LHCC-99-014; ATLAS-TDR-14.

[58] L. Castillo. *The Search and Discovery of the Higgs Boson.* Institute of Physics, 2014.

[59] G. Strong. On the impact of selected modern deep-learning techniques to the performance and celerity of classification models in an experimental high-energy physics use case. *Machine Learning: Science and Technology*, 1(4), 2020, arXiv:2002.01427.

[60] ATLAS Collaboration. ATLAS magnet system. Technical report, CERN, 1997, CERN-LHCC-97-018; ATLAS-TDR-6.

[61] ATLAS Collaboration. ATLAS central solenoid. Technical report, CERN, 1997, CERN-LHCC-97-021; ATLAS-TDR-9.

[62] J. P. Badiou, J. Beltramelli, J. M. Baze, and J. Belorgey. ATLAS barrel toroid. Technical report, CERN, 1997, CERN-LHCC-97-019; ATLAS-TDR-7.

[63] ATLAS Collaboration. ATLAS end-cap toroids . Technical report, CERN, 1997, CERN-LHCC-97-020; ATLAS-TDR-8.

[64] ATLAS Collaboration. Experiment Briefing: Keeping the ATLAS Inner Detector in perfect alignment. 2020.

[65] ATLAS Collaboration. ATLAS inner detector. Technical report, CERN, 1997, CERN-LHCC-97-016; ATLAS-TDR-4.

[66] S. Haywood, L. Rossi, R. Nickerson, and A. Romaniouk. ATLAS inner detector. Technical report, CERN, 1997, CERN-LHCC-97-017; ATLAS-TDR-5.

[67] N. Wermes and G. Hallewel. ATLAS pixel detector. Technical report, CERN, 1998, CERN-LHCC-98-013; ATLAS-TDR-11.

[68] G. Aad, M. Ackers, F. A. Alberti, et al. ATLAS pixel detector electronics and sensors. *JINST*, 3, 2008.

[69] M. Capeans, G. Darbo, K. Einsweiller, et al. ATLAS Insertable B-Layer. Technical report, CERN, 2010, CERN-LHCC-2010-013; ATLAS-TDR-19.

[70] ATLAS Collaboration. Operation and performance of the ATLAS semiconductor tracker. *Journal of Instrumentation*, 9(08), 2014, arXiv:1404.7473.

[71] ATLAS Collaboration. Operation and performance of the ATLAS semiconductor tracker in LHC Run 2. *Journal of Instrumentation*, 17(01), 2022, arXiv:2109.02591.

[72] E. Abat, T. N. Addy, T. P. A. Akesson, et al. The ATLAS Transition Radiation Tracker (TRT) proportional drift tube: design and performance. *JINST*, 3, 2008.

[73] X. Artru, G. B. Yodh, and G. Mennessier. Practical theory of the multilayered transition radiation detector. *Phys. Rev. D*, 12(5), 1975.

[74] C. W. Fabjan and D. Fournier. Calorimetry: Particle Detectors and Detector Systems. *Particle Physics Reference Library: Volume 2: Detectors for Particles and Radiation*, 2020.

[75] Hanagaki, K., Tanaka, J., Tomoto, M. and Yamazaki, Y. *Particle Identification*. Springer Japan, Tokyo, 2022.

[76] C. W. Fabjan and F. Gianotti. Calorimetry for particle physics. *Reviews of Modern Physics*, 75(4), 2003.

[77] ATLAS Collaboration. ATLAS liquid-argon calorimeter. Technical report, CERN, 1996, CERN-LHCC-96-041; ATLAS-TDR-2.

[78] J. Pequenao. Computer generated image of the ATLAS Liquid Argon, 2008.

[79] Escalier, M and Fayard, L and Marchand, J F. Reconstruction of the z vertex and direction of the photon. Technical report, CERN, 2010, ATL-PHYS-INT-2010-013.

[80] ATLAS Collaboration. ATLAS tile calorimeter. Technical report, CERN, 1996, CERN-LHCC-96-042; ATLAS-TDR-3.

[81] ATLAS Collaboration. ATLAS muon spectrometer. Technical report, CERN, 1997, CERN-LHCC-97-022; ATLAS-TDR-10.

[82] T. Kawamoto, S. Vlachos, L. Pontecorvo, et al. New Small Wheel. Technical report, CERN, 2013, CERN-LHCC-2013-006; ATLAS-TDR-020.

[83] ATLAS Collaboration. Letter of Intent for the Phase-I Upgrade of the ATLAS Experiment. Technical report, CERN, 2011, CERN-LHCC-2011-012; LHCC-I-020.

[84] ATLAS Collaboration. Letter of Intent for the Phase-II Upgrade of the ATLAS Experiment. Technical report, CERN, 2012, CERN-LHCC-2012-022; LHCC-I-023.

[85] ApprovedPlotsDAQ, ATLAS Public. https://twiki.cern.ch/twiki/bin/view/AtlasPublic/ApprovedPlotsDAQ. Accessed: 2024-02-26.

[86] ATLAS collaboration. Performance of the ATLAS Trigger System in 2010. *The European Physical Journal C*, 72(1), arXiv:1110.1530.

[87] ATLAS Collaboration. Performance of the ATLAS trigger system in 2015. *The European Physical Journal C*, 77(5), arXiv:1611.09661.

[88] ATLAS Collaboration. Technical Design Report for the Phase-I Upgrade of the ATLAS TDAQ System. Technical report, CERN, 2013, CERN-LHCC-2013-018; ATLAS-TDR-023.

[89] ATLAS Collaboration. The ATLAS trigger system for LHC Run 3 and trigger performance in 2022. *Journal of Instrumentation*, 19(06), 2024, arXiv:2401.06630.

[90] G. E. Orellana. Projected ATLAS Electron and Photon Trigger Performance in Run 3. Technical report, CERN, 2021, ATL-DAQ-PROC-2020-014.

[91] ATLAS Collaboration. ATLAS level-1 trigger. Technical report, CERN, 1998, CERN-LHCC-98-014; ATLAS-TDR-12.

[92] M. Stockton. The ATLAS Level-1 central trigger. In *Journal of Physics: Conference Series*, volume 331. IOP Publishing, 2011.

[93] R. Schwienhorst. The Phase-1 upgrade of the ATLAS first level calorimeter trigger. *Journal of Instrumentation*, 11(01), 2016.

[94] ATLAS Collaboration. Performance of electron and photon triggers in ATLAS during LHC Run 2. *The European Physical Journal C*, 80(1), 2020, arXiv:1909.00761.

[95] P. Jenni, M. Nessi, M. Nordberg, and K. Smith. ATLAS high-level trigger, data-acquisition and controls. Technical report, CERN, 2003, CERN-LHCC-2003-022; ATLAS-TDR-16.

[96] ATLAS Collaboration. The ATLAS Inner Detector trigger performance in pp collisions at 13TeV during LHC Run 2. *European Physical Journal C*, 82(3), 2022, arXiv:2107.02485.

[97] ATLAS Collaboration. The ATLAS Inner Detector Trigger performance in pp collisions at 900 GeV and 13.6 TeV for LHC Run 3 operation during 2022. Technical report, CERN, 2023, arXiv:2107.02485.

[98] T. Sjöstrand, S. Ask, J. R. Christiansen, et al. An introduction to PYTHIA 8.2. *Computer Physics Communications*, 191, 2015, arXiv:1410.3012.

[99] ATLAS Pythia 8 tunes to 7 TeV data. Technical report, CERN, 2014, ATL-PHYS-PUB-2014-021.

[100] N. Themistokleous. Search for right-handed $\mathcal{W}$ bosons and heavy neutrinos with the ATLAS experiment, 2023, CERN-THESIS-2023-044.

[101] G. Avolio, M. D'Ascanio, G. Lehmann-Miotto, and I. Soloviev. A web-based solution to visualize operational monitoring data in the Trigger and Data Acquisition system of the ATLAS experiment at the LHC. In *Journal of Physics: Conference Series*, volume 898. IOP Publishing, 2017.

[102] S. Kolos, G. Boutsioukis, and R. Hauser. High-performance scalable information service for the ATLAS experiment. In *Journal of Physics: Conference Series*, volume 396. IOP Publishing, 2012.

[103] A. D. Sicoe, G. L. Miotto, L. Magnoni, et al. A persistent back-end for the ATLAS TDAQ online information service (P-BEAST). In *Journal of Physics: Conference Series*, volume 368. IOP Publishing, 2012.

[104] M. Chakraborty and A. P. Kundan. Grafana. In *Monitoring cloud-native applications*. Springer, 2021.

[105] ATLAS Collaboration. ATLAS Track Reconstruction - General Overview. https://atlassoftwaredocs.web.cern.ch/internal-links/tracking-tutorial/idoverview/, 2024. Accessed: 06-03-2024.

[106] N. Calace. Track and Vertex reconstruction in ATLAS for LHC Run-3 and High-Luminosity phases. Technical report, CERN, 2021, ATL-COM-PHYS-2021-485.

[107] ATLAS Collaboration. Performance of the ATLAS track reconstruction algorithms in dense environments in LHC Run 2. *The European Physical Journal C*, 77(10), 2017, arXiv:1704.07983.

[108] R. Frühwirth. Application of Kalman filtering to track and vertex fitting. *Nuclear Instruments and Methods in Physics Research Section A: Accelerators, Spectrometers, Detectors and Associated Equipment*, 262(2-3), 1987.

[109] ATLAS Collaboration. Inside out – Ambiguity solving and TRT extension. https://atlassoftwaredocs.web.cern.ch/internal-links/tracking-tutorial/ambitrt/, 2024. Accessed: 08-06-2025.

[110] F. Meloni. Primary vertex reconstruction with the ATLAS detector. *Journal of Instrumentation*, 11(12), 2016.

[111] I. Sanderswood. Development of ATLAS Primary Vertex Reconstruction for LHC Run 3. 2019, arXiv:1910.08405.

[112] ATLAS Collaboration. Topological cell clustering in the ATLAS calorimeters and its performance in LHC Run 1. *The European Physical Journal C*, 77(7), 2017, arXiv:1603.02934.

[113] ATLAS Collaboration. Electron and photon reconstruction and performance in ATLAS using a dynamical, topological cell clustering-based approach. Technical report, CERN, 2017, ATL-PHYS-PUB-2017-022.

[114] ATLAS Collaboration. Electron and photon performance measurements with the ATLAS detector using the 2015–2017 LHC proton-proton collision data. *Journal of Instrumentation*, 14(12), 2019, arXiv:1908.00005.

[115] ATLAS Collaboration. Measurement of the photon identification efficiencies with the ATLAS detector using LHC Run 2 data collected in 2015 and 2016. *The European Physical Journal C*, 79(3), 2019, arXiv:1810.05087.

[116] ATLAS Collaboration. Measurement of Higgs boson production in the diphoton decay channel in *pp* collisions at center-of-mass energies of 7 and 8 TeV with the ATLAS detector. *Physical Review D*, 90(11):112015, 2014, arXiv:1408.7084.

[117] B. Lenzi and D. Delgove. Selection of the diphoton production vertex using multivariate techniques for $H \to \gamma\gamma$ and other analyses. Technical report, CERN, 2015, ATL-COM-PHYS-2015-1321.

[118] ATLAS Collaboration. Measurement of the $H \to \gamma\gamma$ and $H \to ZZ^* \to 4\ell$ cross-sections in pp collisions at $\sqrt{s} = 13.6$ TeV with the ATLAS detector. *The European Physical Journal C*, 84(1), 2024, arXiv:2306.11379.

[119] ATLAS Collaboration. Muon reconstruction performance of the ATLAS detector in proton–proton collision data at $\sqrt{s} = 13$ TeV. *The European Physical Journal C*, 76(5), 2016, arXiv:1603.05598.

[120] ATLAS Collaboration. Muon reconstruction and identification efficiency in ATLAS using the full Run 2 *pp* collision data set at $\sqrt{s} = 13$ TeV. *The European Physical Journal C*, 81(7), 2021, arXiv:2012.00578.

[121] Illingworth, J. and Kittler, J. A survey of the Hough transform. *Computer vision, graphics, and image processing*, 44(1), 1988.

[122] M. Cacciari, G. P. Salam, and G. Soyez. The anti-kt jet clustering algorithm. *Journal of High Energy Physics*, 2008(04), 2008, arXiv:0802.1189.

[123] ATLAS Collaboration. Jet energy measurement with the ATLAS detector in proton-proton collisions at $\sqrt{\text{s}} = 7$ TeV. *The European Physical Journal C*, 73(3), 2013, arXiv:1112.6426.

[124] ATLAS Collaboration. Determination of the jet energy scale and resolution at ATLAS using Z/γ–jet events in data at $\sqrt{s} = 8$ TeV. Technical report, CERN, 2015, ATLAS-CONF-2015-057.

[125] ATLAS Collaboration. Jet reconstruction and performance using particle flow with the ATLAS Detector. *The European Physical Journal C*, 77(7), 2017, arXiv:1703.10485.

[126] ATLAS Collaboration. Performance of pile-up mitigation techniques for jets in *pp* collisions at $\sqrt{s} = 8$ TeV using the ATLAS detector. *The European Physical Journal C*, 76(11), 2016, arXiv:1510.03823.

[127] ATLAS Collaboration. Measurement of the $t\bar{t}$ cross section and its ratio to the Z production cross section using pp collisions at $\sqrt{s} = 13.6$ TeV with the ATLAS detector. *Phys. Lett. B*, 848, 2023, arXiv:2308.09529.

[128] ATLAS Collaboration. ATLAS flavour-tagging algorithms for the LHC Run 2 pp collision dataset. *The European Physical Journal C*, 83(7), 2023, arXiv:2211.16345.

[129] ATLAS Collaboration. The performance of missing transverse momentum reconstruction and its significance with the ATLAS detector using 140 fb^{-1} of $\sqrt{s} = 13$ TeV pp collisions, 2024, arXiv:2402.05858.

[130] Mohamed, A. T. A. Measurement of Higgs Boson Production Cross Sections in the Diphoton Channel: with the full ATLAS Run-2 Data and Constraints on Anomalous Higgs Boson Interactions. Springer Nature, 2020.

[131] ATLAS Collaboration. Measurements of Higgs boson properties in the diphoton decay channel with 36 fb^{-1} of pp collision data at $\sqrt{s} = 13$ TeV with the ATLAS detector. *Phys. Rev. D*, 98(5), 2018, arXiv:1802.04146.

[132] ATLAS Collaboration. Measurement of the isolated diphoton cross-section in pp collisions at $\sqrt{s} = 7$ TeV with the ATLAS detector. 2011, arXiv:1107.0581.

[133] ATLAS Collaboration. Measurement of the Inelastic Proton-Proton Cross Section at $\sqrt{s} = 13$ TeV with the ATLAS Detector at the LHC. *Physical review letters*, 117(18):182002, 2016, arXiv:1606.02625.

[134] G. Billis, B. Dehnadi, M. A. Ebert, et al. Higgs p_T Spectrum and Total Cross Section with Fiducial Cuts at Third Resummed and Fixed Order in QCD. *Physical Review Letters*, 127(7), 2021, arXiv:2102.08039.

[135] A. Djouadi, J. Kalinowski, and M. Spira. HDECAY: a program for Higgs boson decays in the Standard Model and its supersymmetric extension. *Computer Physics Communications*, 108(1), 1998, arXiv:hep-ph/9704448.

[136] A. Djouadi, J. Kalinowski, M. Mühlleitner, and M. Spira. HDECAY: Twenty++ years after. *Computer Physics Communications*, 238, 2019, arXiv:1801.09502.

[137] G. Cowan, K. Cranmer, E. Gross, and O. Vitells. Asymptotic formulae for likelihood-based tests of new physics. *The European Physical Journal C*, 71(2), 2011, arXiv:1007.1727.

[138] ATLAS Collaboration. Preliminary analysis of the luminosity calibration of the ATLAS 13.6 TeV data recorded in 2022. Technical report, CERN, 2023, ATL-DAPR-PUB-2023-001.

[139] ATLAS Collaboration. Preliminary analysis of the luminosity calibration for the ATLAS 13.6 TeV data recorded in 2023. Technical report, CERN, 2024, ATL-DAPR-PUB-2024-001.

[140] S. Agostinelli, J. Allison, K. al Amako, et al. GEANT4—a simulation toolkit. *Nuclear instruments and methods in physics research section A: Accelerators, Spectrometers, Detectors and Associated Equipment*, 506(3), 2003.

[141] ATLAS Collaboration. The ATLAS Simulation Infrastructure. *The European Physical Journal C*, 70(3), 2010, arXiv:1005.4568.

[142] ATLAS Collaboration. AtlFast3: The Next Generation of Fast Simulation in ATLAS. *Computing and Software for Big Science*, 6(1), 2022.

[143] P. Nason. A New Method for Combining NLO QCD with Shower Monte Carlo Algorithms. *Journal of High Energy Physics*, 2004(11), 2004, arXiv:hep-ph/0409146.

[144] S. Frixione, P. Nason, and C. Oleari. Matching NLO QCD computations with parton shower simulations: the POWHEG method. *Journal of High Energy Physics*, 2007(11), 2007, arXiv:0709.2092.

[145] S. Alioli, P. Nason, C. Oleari, and E. Re. A general framework for implementing NLO calculations in shower Monte Carlo programs: the POWHEG BOX. *Journal of High Energy Physics*, 2010(6), 2010, arXiv:1002.2581.

[146] K. Hamilton, P. Nason, and G. Zanderighi. MINLO: multi-scale improved NLO. *Journal of High Energy Physics*, 2012(10), 2012, arXiv:1206.3572.

[147] K. Hamilton, P. Nason, E. Re, and G. Zanderighi. NNLOPS simulation of Higgs boson production. *Journal of High Energy Physics*, 2013(10), 2013, arXiv:1309.0017.

[148] R. D. Ball, J. Butterworth, A. M. Cooper-Sarkar, et al. The PDF4LHC21 combination of global PDF fits for the LHC Run III. *Journal of Physics G: Nuclear and Particle Physics*, 49(8), 2022, arXiv:2203.05506.

[149] C. Bierlich, S. Chakraborty, N. Desai, et al. A comprehensive guide to the physics and usage of PYTHIA 8.3, 2022, arXiv:2203.11601.

[150] R. D. Ball, V. Bertone, S. Carrazza, et al. Parton distributions for the LHC run II. *Journal of High Energy Physics*, 2015(4), 2015, arXiv:1410.8849.

[151] E. Bothmann, G. Singh Chahal, S. Höche, et al. Event generation with Sherpa 2.2. *SciPost Physics*, 7(3), 2019, arXiv:1905.09127.

[152] F. Yu. Phenomenology of enhanced light quark Yukawa couplings and the W±h charge asymmetry. *Journal of High Energy Physics*, 2017(2), 2017, arXiv:1609.06592.

[153] G. Christou. Master's thesis, University of Edinburgh, 2024.

[154] ATLAS Collaboration. Measurements of WH and ZH production with Higgs boson decays into bottom quarks and direct constraints on the charm Yukawa coupling in 13 TeV pp collisions with the ATLAS detector. 2024, arXiv:2410.19611.

[155] Snowmass White Paper Contribution: Physics with the Phase-2 ATLAS and CMS Detectors. Technical report, CERN, 2022, ATL-PHYS-PUB-2022-018.

[156] S. Galli and C. Molnar. *Python feature engineering cookbook: a complete guide to crafting powerful features for your machine learning models*. Packt Publishing Ltd., Birmingham, UK, third edition, 2024.

[157] F. Chollet. Keras 3. https://github.com/keras-team/keras, 2015.

[158] G. Rebala, A. Ravi, and S. Churiwala. *An Introduction to Machine Learning*. Springer International Publishing, first edition, 2019.

[159] Diederik P. K. and Jimmy B. Adam: A Method for Stochastic Optimization, 2017, arXiv:1412.6980.

[160] ATLAS Collaboration. Interpretations of the ATLAS measurements of Higgs boson production and decay rates and differential cross-sections in pp collisions at $\sqrt{s} = 13$ TeV. 2024, arXiv:2402.05742.

[161] G. Cowan. *Statistical data analysis*. Oxford science publications. Clarendon Press, Oxford, 1998.

[162] G. Cowan, K. Cranmer, E. Gross, and O. Vitells. Asymptotic formulae for likelihood-based tests of new physics. *The European Physical Journal C*, 71(2), 2011, arXiv:1007.1727.

[163] ECFA Early-Career Researchers Panel. https://ecfa.web.cern.ch/ecfa-early-career-researchers-panel. Accessed: 28-08-2024.

[164] J. Allen, B. Alves, J. H. Arling, et al. The ECFA Early-Career Researchers Panel: Report for the year 2023, 2024, arXiv:2407.12761.

[165] J. Allen, K. Augsten, G. Benato, et al. Results of the 2022 ECFA Early-Career Researchers Panel survey on career prospects and diversity, 2024, arXiv:2404.02074.

[166] J. Allen, A. Chisholm, H. Pacey, et al. Report on the UK Future Collider Town Hall (6/7/2023). https://conference.ippp.dur.ac.uk/event/1201/sessions/1509/attachments/4963/6722/TownHall_July2023_Report.pdf. Accessed: 28-08-2024.